ELECTRON ENERGY LOSS SPECTROSCOPIC STUDY OF SMALL MOLECULES ON TRANSITION METAL SURFACES

Thesis by

Youqi Wang

In Partial Fulfillment of the Requirements

for the Degree of

Doctor Of Philosophy

California Institute of Technology

Pasadena, California

1995

(Submitted October 5, 1994)

君欲谋其道必先谋其食

Acknowledgment

It is indeed one of the few luckiest things happened in my life to have Professor W. Henry Weinberg as my thesis advisor. In the past eight years, I was given the level of trust and understanding that Henry ever gave to his students. It is this kind of support, *together* with his precious advises and guidance, that makes it possible for me to achieve what I have achieved. I sincerely thank to Professor Weinberg for the past eight golden years, especially for those moments that were so wonderful that I may never have it again in the rest of my life.

It is another luckiest thing to have Dr. Hua Chuan as my companion of life. Without her understanding at the deepest level, without her support in all respects, without her delicate and appropriate helps, it would be impossible for me to overcome what I have overcome and to reach what I have reached. To large extent, it was the interaction with her and the difficulties encountered in the communication that prompted me to realize what I have realized. I sincerely thank to Dr. Hua Chuan for the companionship in the past eleven years and the years to come that are expected to be more colorful and exciting. According to her prediction, my dream will become true before I fade out.

I think the most precious possession I can have in this world is to have someone I can communicate with without too much difficulty in language. I am rich in this respect. Among all of my friends, Dr. Shenheng Guan played an important role in my scientific effort during the past eight years. It was from him that I first learned the idea of maximum entropy, which eventually led to the development of UHREELS. It was also from the interaction with him that I obtained the final stimulus towards a deeper understanding of what I was doing. I am very grateful to the friendship with Guan in the past sixteen years and the years to come.

Many of my friends have made their contributions in their own ways that are significant and non-trivial to my own evolution. I would like to show here my special

thanks to Dr. Peijun Cong, Dr. Ling Zuo, Dr. Hongqiang Ding, and Dr. Mingsheng Hang. I also thank to Mr. Paul Yin and Ms. Hui Guo for the many stimulating discussions.

During my work at UCSB, I have been benefited from the friendship with my fellow student William J. Mitchell and Jun Xie. Without their help, my progress would have been much slower and lesser. We also shared many cheerful memories for those victories and frustrations working in the laboratory. I would like to quote here an interesting argument from Bill (almost the original): "If the thing is as simple and trivial as you think it is, it must have been figured out already. Since this does not seem to be the case, you must have made some mistake in your thinking." To large extent, this argument also reflects my own attitude towards my work, done or to be done, although I haven't figured out what's wrong in my thinking yet.

I have also been benefited a lot from Professor Weinberg's research group. In the past several years, I have given quite many group seminars regarding UHREELS and something else. From the discussions with the group, I have obtained many stimuli towards my work. In this regard, I particularly thank to Dr. Wolf Widdra, Mr. Kevin Lyons, and Mr. Kyle Self. Wolf is an interesting person, who wouldn't agree almost every word I have said. However, his objection has been a constant source in forcing me to think deeper and to try to find better ways for communicating.

I am grateful to the collaborations that I have had with Dr. John E. Parmeter, Dr. C. Buddie Mullins, Dr. Y.-K. Sun, and Dr. Dale F. Johnson. I have had a lot of fun in working with these fellows. They are not only my colleagues but also my friends. John was the person who introduced me to EELS. He was also the person who prompted me into the information processing business. Buddie and I have shared many common views towards science in general and the experimental work in particular. He also gave me many helps during my stay in Caltech. I thank him very much.

I would like to express my sincerest appreciation to Professor Harry B. Gray. As the chairman of the committee for my Ph.D. examinations, he has made great personal efforts

in successfully joining the forces from the different disciplines to insure the quality of the examinations. I am most grateful for his deep understanding and his great encouragement for my pursuit of the truth. I have great respect for him both as a scientist and a person.

I am also grateful to Professor David L. Goodstein, Professor John E. Bercaw, and the entire committee for their active participation to this process of science. I thank to them for their appreciation and criticism of the work I have done. I also thank to them for their giving me the opportunity to freely express my own opinion regarding the work. The day of the examinations is certainly one of the most cheerful days in my life.

I would like to express my special thanks to Professor Kip S. Thorne and Professor Steven C. Frautschi for their crucial involvement in the process of my Ph.D. examinations. They not only corrected the errors I made in my manuscript (not this volume) but also gave me many invaluable comments and suggestions that form the guideline of my future work. I was so impressed by the fact that, as a leading theoretical physicist of the world, Professor Thorne would read the manuscript so seriously and so carefully and would appreciate the small things I found. I am also very impressed by his amiable personality and his capability of understanding that dramatically reduced the barrier of language and made it much easier for me to communicate with him. His serious attitude towards a layman's work is a great encouragement for me to continue the work.

Being a student of Caltech is a privilege and a fortune of the lifetime. I sincerely thank to Professor Zi Gao, Professor D. M. Lindsay, Professor T. F. George for recommending me to Caltech. Professor Gao took great personal risks in writing the recommendation letter for me. In 1986, not everyone in China would have the courage to do what she has done. Professor Lindsay gave me the opportunity to come to America and helped me in many ways during my initial stay in this great land of freedom. He also made special effort in arranging me into Caltech. The experience I gained in working with him benefited a lot during my later work. Professor George also helped me in many respects. His charming personality and the ability of understanding are still very impressive to me.

During the past eight years, I have received many helps from the Chemistry Department of Caltech, not only from the departmental officials but also from the stuff members as well as the mechanics shop personal. The institute also provided very precious help to foreign students, especially the housing office. I sincerely thank to all those wonderful people in Caltech.

My experience in the Chemical Engineering Department of UCSB is also very cheerful. During the period of the laboratory setup, I have obtained many helps and assistance from the department personal. I sincerely thank to Mr. Ruddy of the physics mechanics shop for the many helps and the knowledge he taught me. Special thanks to Ms. Chari for the helps she provided to me.

Many people have helped me in the past, those in the united states as well as those on the other side of the Earth. Their kindness always makes me feel pressured and has always been a source of motivation for me to try to do something useful to the society.

Abstract

The scheme of ultrahigh-resolution electron energy loss spectroscopy (UHREELS) is described in detail with graphical examples of the real data processing. On the basis of modern digital information processing techniques, this method promises to yield EEL spectra with the ultimate resolution and superior signal to noise ratio.

The interaction of ammonia with clean and chemically modified Ru(001) surfaces were studied by using HREELS, TPD, and LEED techniques under UHV condition. Ammonia is found to interact with the surface chiefly through its lone-pair electrons, evidenced by the blue-shift of ammonia symmetric deformation mode and the increase of thermal desorption temperature of ammonia on both oxygen and nitrogen modified surfaces. No detectable dissociation of ammonia is found under the specified conditions.

The reactions of gas-phase atomic hydrogen with oxygen and carbon monoxide pre-adsorbed on Ru(001) surface at low temperature were studied *via* HREELS technique. The experimental results can be understood via an Eley-Rideal-like mechanism.

The decomposition mechanism of methylamine on Ru(001) surface was investigated by HREELS and TPD techniques. The cyanide adspecies was found to be side-on bonded on the ruthenium surface and its bond order is reduced from three to two.

Table of Contents

Summary

This thesis is a collection of several publications authored or co-authored by me. It reflects part of the research works I have done in the past eight years.

My major project towards the Ph.D. degree is to find a way to extract information from EELS experiment *as much as possible* and *as objectively as possible*. This project was initiated in the summer of 1987 with a special grant from the National Science Foundation. To large extent, I have achieved the goal successfully. The method that I came up with is referred to as UHREELS.

The main content of UHREELS is presented in Ref. 1. Basically, it is nothing but an organic combination of several well-known digital information processing techniques, i.e., deconvolution, maximum entropy spectral estimation, and system modeling *via* non-linear optimization. The purpose of the combination is to take the advantages of each technique while avoiding their disadvantages. The issues regarding this are briefly discussed in Ref. 2. The working procedure of UHREELS is given in Ref. 3.

Although UHREELS is indeed very simple or even trivial, its application may well be beyond EELS. This may be seen from the following quote taken from the comment of the referee of Ref. 3: "The authors are perfectly right in saying that their result, if correct, could have a profound impact in science. In fact it should not be necessary to improve microscopes and telescopes and, in particular, it should not be necessary to spend millions of dollars for correcting the aberrations of the Hubble telescope."

Obviously, the referee aforementioned missed the point and didn't believe UHREELS could work. Some other kinds of criticism can be found in Ref. 4 and several other recent publications. The lesson I learned from these responses is that, even though the method is trivial, detailed explanation is still very necessary. The manuscript on the general Fourier transform (GFT) and its property of *information conservation* has been drafted [5], which is the information basis of the method. However, the content still seems too trivial to be

published. Some of the misunderstandings regarding UHREELS has been briefly discussed in Ref. 6, and I am planning to write down a detailed version of the theory behind the UHREELS very soon.

The key to the success of UHREELS is the convolution relationship existed in an EEL spectrum and the accessibility of the *in situ* information regarding the instrument response function. It is thus crucial to obtain the response function as accurately as possible. I spent almost two years in trying to achieve this goal *via* pattern recognition approach with a sophisticated program. However, the performance was not very satisfactory. The human dependence in the process of determining the instrument response function makes it meaningless to perform statistical analysis on the final output of UHREELS. It was only in the summer of 1993 that I realized that there is a simple way of doing the job (see proposition two in Ref. 5 for details). Using the new approach, the subjectivity in the determination of the response function can be eliminated and the uncertainty of the determination can be quantified statistically. Consequently, the error estimation of the output of UHREELS can be carried out *via* the various standard statistical analysis techniques [7].

Although UHREELS holds the promise to yield EEL spectra with ultimate resolution, superior noise suppression, and much higher detecting sensitivity, as evidenced in Ref. 1, it also requires significant modifications of the EELS system and the change of the way of spectrum acquisition [3,5]. Since 1989, the EELS system that I associated with has been modified significantly. For example, the electron detecting system has been redesigned and manufactured which allows the dynamic range of about twenty times wider than before. The electronics system has been redesigned and manufactured with lower electric noise, faster response, and much lower thermal and temporal drift. The tuning system is now computer controllable. The heating/cooling system has also been changed to allow faster response and liquid helium operations, and the operations are

programmable now. All these changes are towards the completion only very recently. Therefore, the details have to be seen in the future publications from this research group.

The investigation of $NH_3/Ru(001)$ system began in the winter of 1986 when I started to learn EELS. The results of ammonia on clean Ru(001) surface are given in Ref. 8. One of the objects was to study the interactions of ammonia molecules on the surface. The observed linear (almost) dependency of the symmetric deformation (umbrella mode) on surface coverage indicates that the interaction is of long range (through metal) type, which is consistent with other experimental evidences. It was thus predicted that, on chemically modified surfaces with electron acceptors, similar linear dependency of the umbrella mode on the coverage should be observed. Subsequent research of ammonia on oxygen modified Ru(001) surface was carried out extensively with EELS as the main tool for the investigation. The results confirmed the prediction. Since these results are rather trivial, they are not published yet. To complete the study, efforts have been made in trying to modify the surface with nitrogen atoms. This initiated the collaboration with Y.-K. Sun in 1988 [9]. It turned out that preparing a nitrogen modified surface in the given EELS system was very difficult. The system needs significant modifications. The modifications began in 1989 after relocating the laboratory to UCSB. However, upon finishing the required works, the interest was shifted to, e.g., reaction studies.

One of the motivation of $NH_3/Ru(001)$ study was to try to figure out where ammonia sits on hexagonally close-packed metal surfaces. Although this group holds the belief that ammonia sits on on-top site, supported by coordination compounds comparison [8] and ammonia/oxygen/ruthenium study, most of other research groups believe that ammonia sits on three-fold site, and there is no direct and unambiguous experimental evidence yet for the justification. Sun's work [9] set a basis for obtaining the decisive experimental evidence needed by means of nitrogen modified surfaces, particularly the $\left(\sqrt{3} \times \sqrt{3}\right)R30^{\circ}$-N superstructure on Ru(001). The research plan has been discussed extensively for several years. However, I simply had no time in executing this plan.

The atomic hydrogen reaction studies [10-12] are some of the initial works on the modified EELS system. My contribution to these works is mainly on the instrumentation and experimental aspects, with some involvement in the data analysis.

The methylamine investigation [13,14] was a project continued from J. E. Parmeter and M. M. Hills' initial study. I was mainly responsible for the EELS experiments conducted in 1987 and had a little involvement in the spectral interpretation. This work is basically a completed research. However, I do wish that I could have a chance to do some EELS work on HCN.

From 1986 to 1989, I also intensively involved in the molecular-beam experiments in collaboration with C. B. Mullins. Most of the efforts were devoted to reshape the monster molecular-beam apparatus and to put the machine into workable condition. Part of that effort is reflected in Ref. 15.

My other experimental works include, e.g., FTIR instrumentation and molecular-beam system design and construction. The FTIR system is now approaching the stage of data production. The major portion of the beam system has been constructed but not installed yet. These works will be seen in the future publications from this research group, and I am proud of the fact that Professor Weinberg's surface vibration laboratory is now the best one in the world.

[1]   Y. Wang and W. H. Weinberg, Phys. Rev. Lett. **69**, 3326 (1992). This thesis, p. 1.

[2]   Y. Wang and W. H. Weinberg, Surf. Sci. **287/288**, 1102 (1992). This thesis, p. 6.

[3]   Y. Wang and W. H. Weinberg, this thesis, p. 10. The main contents have been posted at the 1993 international conference on surface vibrations.

[4]   B. G. Frederick and N. V. Richardson, Phys. Rev. Lett. **73**, 772 (1994).

[5]   Y. Wang, Research propositions for the Ph.D. degree in chemistry (Caltech, 1994).

[6]   Y. Wang and W. H. Weinberg, Phys. Rev. Lett. **73**, 773 (1994). This thesis, p. 5.

[7] W. H. Press, B. P. Flannery, S. A. Teukolsky, and W. T. Vetterling, *Numerical Recipes* 2nd ed. (Cambridge, Cambridge, 1992).

[8] J. E. Parmeter, Y. Wang, C. B. Mullins, and W. H. Weinberg, J. Chem. Phys. **88**, 5225 (1988). This Thesis, p. 79.

[9] Y.-K. Sun, Y. Wang, C. B. Mullins, and W. H. Weinberg, Langmuir **7**, 1689 (1991). This thesis, p. 45.

[10] W. J. Mitchell, Y. Wang, J. Xie, and W. H. Weinberg, JACS **115**, 4381 (1993). This thesis, p. 63.

[11] W. J. Mitchell, J. Xie, Y. Wang, and W. H. Weinberg, J. Electron Spec. Related Phenom. **64/65**, 427 (1993). This thesis, p. 65.

[12] J. Xie, W. J. Mitchell, K. J. Lyons, Y. Wang, and W. H. Weinberg, J. Vac. Sci. Technol. A **12**, 2210 (1994). This thesis, p. 72.

[13] W. H. Weinberg, D. F. Johnson, Y. Wang, J. E. Parmeter, and M. M. Hills, Surf. Sci. Lett. **235**, L299 (1990). This thesis, p. 41.

[14] D. F. Johnson, Y. Wang, J. E. Parmeter, M. M. Hills, and W. H. Weinberg, JACS **114**, 4279 (1992). This thesis, p. 51.

[15] C. B. Mullins, Y. Wang, and W. H. Weinberg, J. Vac. Sci. Technol. A **7**, 2125 (1989). This thesis, p. 77.

Ultrahigh-Resolution Electron Energy Loss Spectroscopy via Digital Signal Processing Techniques

Youqi Wang and W. Henry Weinberg

Department of Chemical Engineering, University of California, Santa Barbara, California 93106-5080

The methodology underlying a novel spectral analysis is presented for inelastic electron scattering from solids. Implementation of the method involves Fourier transformation of the measured spectrum and deconvolution in the Fourier domain, spectral estimation using the maximum entropy method, and line-shape analysis using Gaussian and Lorentzian functions, all performed in the Fourier domain. The utility of the method is demonstrated for the case of vibrationally inelastic electron scattering from CO adsorbed on Ru(001).

PACS numbers: 61.16.–d, 06.50.Dc, 68.45.Da, 68.45.Kg

Since the pioneering work of Propst and Piper [1], inelastic electron scattering from surfaces, also known as electron energy loss spectroscopy (EELS), has become one of the most important tools in the study of the vibrational properties of solid surfaces [2,3]. Applications of the technique range from elucidating vibrational structures of chemically and physically adsorbed overlayers to mapping dispersion relations of surface phonons. Some of the advantages of EELS compared, for example, to an optical spectroscopy such as infrared reflection-absorption spectroscopy (IRAS) [4,5] include the following: (1) higher sensitivity, (2) wider dynamic detection range, and (3) selection rules that permit observation of optically forbidden modes (those oriented parallel to the surface). The major disadvantage of EELS has been its relatively poor resolution compared to optical spectroscopies. Much progress has been made in the past 25 years in the design and construction of electron beam monochromators and energy analyzers and their associated electronics [6], and recently Ibach's group have published spectra with a resolution of 1 meV (FWHM of the elastically scattered peak) [7]. It remains, however, rather difficult to obtain energy loss spectra with a FWHM below 4–5 meV, and "high-resolution" EELS is generally applied to those spectra with a FWHM below 10 meV.

Despite these remarkable improvements in the "hardware" associated with EELS, the development of "software" to process the data is still in its infancy. In studies of metal oxide surfaces, deconvolution techniques have been implemented to suppress surface phonon modes [8,9]. Because of difficulties inherent in deconvolution schemes [10,11], this technique improves neither the spectral resolution nor the signal-to-noise ratio (SNR). Curve-fitting techniques have been combined with measurements of the instrument response function (the FWHM of the elastically scattered peak in this case) with the goal of obtaining the true linewidth of surface vibrational modes [12,13]. This procedure is of limited use, however, since a priori knowledge of the number of peaks in a spectrum

and their shapes is required, a problem that is common to all curve-fitting schemes [14].

In this Letter, we describe a novel spectral analysis method which is capable of eliminating all broadening due to the instrument response function. A complete discussion of our procedure, including all details and sensitivity analyses, will be published elsewhere [15]. This procedure allows, for the first time, a determination of the natural line shapes of the physical or chemical system being investigated. In addition to this improvement in resolution, the spectral SNR is also increased by orders of magnitude. Although we apply our method here to the problem of vibrational EELS, the algorithm is quite general and can be used in connection with any spectroscopy for which the instrument response function can be obtained accurately from either experiment or theory.

A measured EEL spectrum can be expressed mathematically as [15]

$$s(E) = i(E) * c(E) + n(E) , \tag{1}$$

where $s(E)$ is the measured spectrum as a function of loss energy E, $i(E)$ is the instrument response function [16], $c(E)$ is the transfer function of the chemical system (a scattering function), $n(E)$ takes into account noise, and the symbol $*$ denotes a convolution operation. Note that

$$c(E) = \delta(E) + c_i(E) , \tag{2}$$

where $\delta(E)$ and $c_i(E)$ account for elastic and inelastic scattering, respectively. Substituting Eq. (2) into Eq. (1) gives

$$s(E) = i(E) + i(E) * c_i(E) + n(E) . \tag{3}$$

It is clear from Eq. (3) that the measured elastic peak is an accurate representation of the instrument response function. Since the elastic peak intensity is typically 2 to 3 orders of magnitude greater than those of the inelastic peaks [2,3], $i(E)$ can be determined experimentally with high accuracy. Taking the Fourier transform of Eq. (1) and rearranging terms gives

1

$$\frac{S(\tau)}{I(\tau)} = C(\tau) + \frac{N(\tau)}{I(\tau)} , \qquad (4)$$

where capital letters denote functions in the Fourier domain, τ. Notice that the left-hand side of Eq. (4) may be constructed from measured spectral data, and the first term on the right-hand side describes fully the scattering function with no interference from the instrument response function, i.e., the latter has been deconvoluted from the former.

The maximum entropy method (MEM) [17-19] may be used for spectral estimation. In this connection we define

$$S'(\tau) \equiv \frac{S(\tau)}{I(\tau)} \quad \text{and} \quad N'(\tau) \equiv \frac{N(\tau)}{I(\tau)} , \qquad (5)$$

which implies that $S'(\tau) = S(\tau) + N'(\tau)$. We next define a "cutoff" point, $\tau_{\max}$, in the Fourier domain such that

$$\left| \frac{S'(\tau)}{N'(\tau)} \right| \equiv \left| \frac{S(\tau)}{N(\tau)} \right| \gg 1, \quad |\tau| \le \tau_{\max} , \qquad (6)$$

and we solve

$$\hat{R}\alpha = q\beta , \qquad (7)$$

where $\alpha = (1, \alpha_1, \alpha_2, \ldots)^T$, $\beta = (1, 0, 0, \ldots)^T$, and $R_{ij} = \langle S'(\tau_n)S'(\tau_{n+i-j}) \rangle$, $i, j = 1, 2, \ldots, m$. Here, $\hat{R}$ is the autocorrelation matrix, α is the autoregression coefficient vector (to be determined), q is a scaling factor (also to be determined), β is a unit vector, and m is the total number of deconvoluted spectral data points in the Fourier domain that satisfy Eq. (6). The scattering function, $c(E)$, can then be estimated by

$$c(E) \approx \frac{|q|}{\left| 1 + \sum_{\ell=1}^{m-1} \alpha_\ell e^{iE\tau_\ell} \right|} . \qquad (8)$$

The approximation in Eq. (8) is due to the truncation of $S'(\tau)$. By taking the second derivative of Eq. (8), the following information can be obtained: (1) the total number of spectral peaks, M; (2) the frequency of each peak, E_k ($k = 1, 2, \ldots, M$); and (3) an approximate estimate of the intensities and linewidths of each peak. Note that the total number of peaks may be inflated both by peaks resulting from a nonflat baseline in the original spectrum and by peaks resulting from excessive noise or extremely low count rates in that part of the spectrum where they appear. The former are characterized by very broad peak widths (FWHM of a few hundred to a few thousand wave numbers) after complete processing, and the latter are characterized by their negligible or even negative intensities during subsequent processing. We found that, for isolated peaks, the accuracy of this method is very high (frequency determination typically to less than 1 cm^{-1}), but this is not the case for peaks that are closely spaced due to the derivative method that

is used. Deviations from the true peak centers thus depend on the spacing, relative intensities, and line shapes of the individual peaks.

Although Eq. (8) supplies a rather accurate estimate of the number of spectral peaks and the frequencies at which they occur, the information regarding intensities and line shapes is usually not accurate and varies depending on the specific algorithm that is used and the size of the autocorrelation matrix, $\hat{R}$. In order to determine intensities more accurately, we note that most of the inelastic peaks have a FWHM smaller than that of the instrument response function. Hence, they can be reasonably treated as δ functions at this level of approximation. Consequently, Eq. (2) may be rewritten as

$$c(E) \approx \delta(E) + \sum_{k=1}^{M} h_k \delta(E - E_k) , \qquad (9)$$

where h_k denotes the integral intensity of the kth vibrational mode, normalized to that of the elastic peak. We next define an error function in the energy domain as follows:

$$\chi_E^2(\mathbf{h}) \equiv \sum_E \left\{ s(E) - i(E) - \sum_{k=1}^{M} h_k i(E - E_k) \right\}^2 , \qquad (10)$$

where $\mathbf{h} \equiv (h_1, h_2, \ldots, h_M)^T$. The solution of the equation

$$\nabla_{\mathbf{h}} \chi_E^2(\mathbf{h}) = 0 \qquad (11)$$

provides an approximate determination of the intensities of the inelastic peaks. The accuracy is dependent on the validity of the δ-function approximation of Eq. (9).

The only remaining issue to be addressed concerns the line shapes of the inelastic peaks, coupled with a refinement of the peak intensities and positions. With this goal in mind, we note that the intrinsic vibrational line shape may be modeled as a Lorentzian function broadened by a Gaussian function (due to a variety of fluctuations normally present in a real system). Consequently, we can construct a system model as follows [cf. Eq. (9)]:

$$C_{\text{model}}(\tau, \mathbf{p}) = 1 + \sum_{k=1}^{M} h_k e^{-iE_k\tau} B_k(\tau) , \qquad (12)$$

where

$$B_k(\tau) = \exp\left[-w_{L,k} |\tau| - \left(\frac{w_{G,k}}{2}\tau \right)^2 \right] ,$$

and

$$\mathbf{p} = (h_1, E_1, w_{L,1}, w_{G,1}, \ldots, h_M, E_M, w_{L,M}, w_{G,M})^T .$$

Here, $w_{L,k}$ is the Lorentzian width, and $w_{G,k}$ is the Gaus-

3327

sian width. Next we define an error function in the Fourier domain as follows:

$$\chi_F^2(\mathbf{p}) \equiv \sum_{|\tau| \le \tau_{max}} |S(\tau) - I(\tau)C_{model}(\tau, \mathbf{p})|^2 \; ; \quad (13)$$

and solving

$$\nabla_{\mathbf{p}} \chi_F^2(\mathbf{p})|_{\mathbf{p}=\mathbf{p_0}} = 0 \quad (14)$$

provides the energies of the inelastic peaks, their intensities, and their line shapes [20]. The system transfer function $c(E)$ may be obtained by evaluating the inverse Fourier transform, i.e.,

$$C_{model}(\tau, \mathbf{p_0}) \to c(E) \, . \quad (15)$$

To demonstrate the power of our methodology, we have applied it to a nearly saturated chemisorbed overlayer of CO on Ru(001), corresponding to a 6 L ($1 \text{ L} = 10^{-6}$ Torr s) exposure at room temperature, a system that has been well studied by low-energy electron diffraction (LEED) [21], vibrational EELS [22], and IRAS [23]. We have collected new vibrational EELS data for this system with a modest resolution (FWHM of the elastically scattered peak) of 6.7 meV $\cong$ 54 cm^{-1}, and the results are presented in Fig. 1(a) in which 4096 data points were collected with a channel resolution of 2 cm^{-1} and a total collection time of 1000 s. A full description of the EEL spectrometer and the data acquisition scheme is presented elsewhere [2,15,24]. The system transfer function $c(E)$, calculated from Eq. (8) using Marple's algorithm [19], is shown in Fig. 1(b); and the final EEL spectrum after complete processing is shown in Fig. 1(c). There are three different CO stretching modes between 1900 and 2100 cm^{-1}, and five frustrated translations and rotations
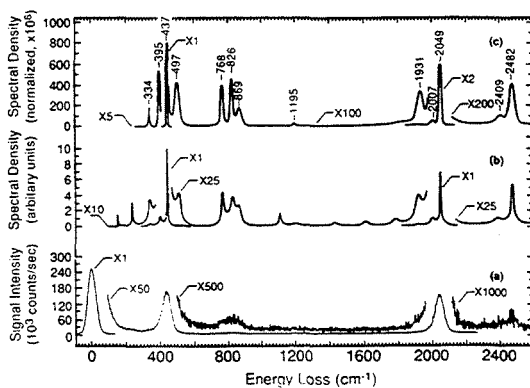

FIG. 1. (a) Measured HREEL spectrum in the specular direction of a saturation coverage of CO on Ru(001) at 300 K. (b) The approximate response function of the CO overlayer given by Eq. (8). (c) The HREEL spectrum after complete processing.

below 500 cm^{-1} [including one at 226 cm^{-1} which is not shown in Fig. 1(c)]. Harmonic and combination bands are apparent between 700 and 900 cm^{-1}, and between 2400 and 2500 cm^{-1}. The three CO stretching modes have a FWHM of 17 cm^{-1} (for the 2049-cm^{-1} peak), 29 cm^{-1} (for the 2007-cm^{-1} peak), and 43 cm^{-1} (for the 1931-cm^{-1} peak); whereas the correlated frustrated translations at 437, 395, and 334 cm^{-1} have FWHM's of 8, 10, and 9 cm^{-1}, respectively. Although a full discussion of these data will be presented elsewhere [15], there are two points to be noted here. First, using IRAS, Pfnür et al. [23] observed a single band centered at 2048 cm^{-1} with a FWHM of 12 cm^{-1} for a saturation coverage of CO on Ru(001) at 300 K [cf. 2049 and 17 cm^{-1} in Fig. 1(c)]. Their slightly more narrow peak and the absence of a small band at 2007 cm^{-1} suggest their overlayer was somewhat better ordered than ours [25]. (Their sensitivity would have precluded their observing the band at 1931 cm^{-1}, even if it had been present.) Furthermore, if we assume that the integrated spectral density is proportional to the concentration of the three different kinds of adsorbed CO, we find that 84% of the CO is associated with the 2049-cm^{-1} peak, 13% with the 2007-cm^{-1} peak, and 3% with the 1931-cm^{-1} peak. The accuracy of our frequency determinations is substantiated by the following: (1) The frequency of the dominant CO stretching mode agrees with IRAS data to 1 cm^{-1}; (2) our peaks on both the energy-gain and energy-loss side of the elastic peak agree within 2 cm^{-1}; and (3) the variation in frequency among numerous different measured spectra (for ostensibly the same CO overlayer) is less than 3 cm^{-1}. The sensitivity of the method should be clear by comparing Figs. 1(a) and 1(c). In this connection we might also note that the CO stretching mode at 2049 cm^{-1} on the energy-gain side of the elastic peak was clearly observed in the processed spectra even though its average count rate was less than 1 count/s.

Several final comments are appropriate concerning our data processing procedure. First, since by definition $i(E)$ includes various properties of the surface, it must be determined from each measured spectrum. Second, the amplitude of the elastic peak is irrelevant so long as $i(E)$ can be measured accurately and the detector is not operated under saturation conditions. Most important, the success of the method (resolution, sensitivity, and reliability of line-shape determination) is a strong function of the range of data in the Fourier domain [cf. Eq. (6)]. An accurate line-shape determination presents the greatest challenge to the method; having a sufficiently narrow elastic peak and a measured spectrum with a sufficiently high SNR ensures the success of even this difficult endeavor.

To summarize, a data processing methodology has been described that renders vibrational EELS an ultrahigh-resolution spectroscopy. Accurate peak positions, peak intensities, and line-shape functions may be

3328

3

extracted from measured EELS data. Our methodology should revolutionize both vibrational and electronic EELS measurements, and generalizations of it should find broad applications in other spectroscopic techniques.

[1] F. M. Propst and T. C. Piper, J. Vac. Sci. Technol. 4, 53 (1967).

[2] W. H. Weinberg, in *Solid State Physics: Surfaces*, edited by R. L. Park and M. G. Lagally, Methods of Experimental Physics Vol. 22 (Academic, Orlando, 1985), p. 23.

[3] H. Ibach and D. L. Mills, *Electron Energy Loss Spectroscopy and Surface Vibrations* (Academic, New York, 1982).

[4] F. M. Hoffmann, Surf. Sci. Rep. 3, 107 (1983).

[5] Y. J. Chabal, Surf. Sci. Rep. 8, 211 (1988).

[6] H. Ibach, *Electron Energy Loss Spectrometers: The Technology of High Performance*, Springer Series in Optical Sciences Vol. 63 (Springer-Verlag, Berlin, 1991).

[7] G. Kisters, J. G. Chen, S. Lehwald, and H. Ibach, Surf. Sci. 245, 65 (1991).

[8] P. A. Cox, W. R. Flavell, A. A. Williams, and R. G. Egdell, Surf. Sci. 152/153, 784 (1985).

[9] W. T. Petrie and J. M. Vohs, Surf. Sci. 245, 315 (1991).

[10] G. K. Wertheim, J. Electron Spectrosc. Relat. Phenom. 6, 239 (1975).

[11] A. F. Carley and R. W. Joyner, J. Electron Spectrosc. Relat. Phenom. 16, 1 (1979).

[12] B. Voigtländer, D. Bruchmann, S. Lehwald, and H. Ibach, Surf. Sci. 225, 151 (1990).

[13] C. Astaldi, A. Bianco, S. Modesti, and E. Tossatti, Phys. Rev. Lett. 68, 90 (1992).

[14] W. F. Maddams, Appl. Spectrosc. 34, 245 (1980).

[15] Youqi Wang and W. H. Weinberg (to be published).

[16] The instrument response function is defined here as the convolution product of the kinetic energy profile of the incident electron beam, the response function of the electron energy analyzer and detector, and a surface-related function describing broadening due to surface roughness, for example. A constant is also included to account for surface reflectivity, normalization, and units conversion. A detailed derivation is presented elsewhere [15].

[17] J. P. Burg, in *Proc. 37th Meeting Soc. Exploration Geophysicists* (1967); J. P. Burg, Ph.D. dissertation, Stanford University, 1975 (unpublished).

[18] J. N. Kapur, *Maximum-Entropy Models in Science and Engineering* (Wiley, New York, 1989), and references therein; *Modern Spectrum Analysis*, edited by D. G. Childers (IEEE, New York, 1978).

[19] L. Marple, IEEE Trans. Acoustics, Speech, and Signal Process. 28, 441 (1980).

[20] The nonlinear optimization procedure of Eq. (14) requires a good starting point to ensure reliable results and rapid convergence. This is accomplished by using the results from both the MEM and the linear optimization procedure [cf. Eqs. (8) and (11), respectively].

[21] E. D. Williams and W. H. Weinberg, J. Chem. Phys. 68, 4688 (1978); Surf. Sci. 82, 93 (1979).

[22] G. E. Thomas and W. H. Weinberg, J. Chem. Phys. 70, 1437 (1979).

[23] H. Pfnür, D. Menzel, F. M. Hoffmann, A. Ortega, and A. M. Bradshaw, Surf. Sci. 93, 431 (1980).

[24] G. E. Thomas and W. H. Weinberg, Rev. Sci. Instrum. 50, 497 (1979).

[25] This is supported by the following two observations: (1) The CO stretching peaks of Fig. 1(c) are dominated by Gaussian (inhomogeneous broadening) functions; and (2) peaks are present that are characteristic of *very small* amounts of hydrogen and hydrocarbon contamination (at 1105, 1195, and 2966 cm^{-1}).

Wang and Weinberg Reply: Frederick and Richardson (FR) [1] have raised three major issues related to our scheme for obtaining ultrahigh resolution electron energy loss spectra [2]. We will address each of these points briefly with elaborations below. First, our method is indeed novel because is it superior to all competing schemes and has not been heretofore employed. The "more powerful commercially available software" is inferior, in principle. Second, although Burg's MEM *may* be rather well understood when applied to time series analysis, the method *must be modified* for spectral deconvolution applications. Third, although Burg's standard MEM may give little line-shape information, this is an irrelevant observation vis-à-vis our *two-step* methodology.

The major confusion concerning our method seems to be caused by the meaning of "Fourier transform." *If* the standard discrete Fourier transform (DFT) [3] is used, noise amplification does present a major difficulty. If a filter is then used, information is distorted; if transformed data are truncated, information is lost. This situation cannot be improved, no matter what mathematical tricks are played [4]. Therefore, we do *not* use the DFT in our methodology but rather employ a Fourier transform which is defined for a pair of *discrete* series with independent variables that are *continuous*. One important property of this transform is *information conservation* which allows truncation of transformed data without loss of information [5].

Using this transform [5], noise can be treated properly, and our expression for the autocorrelation matrix turns out to have the same *form* as that of Burg's MEM. As may be seen in Fig. 1(b) of Ref. [2], our method does *not* generate a series of δ functions, as FR note that Burg's MEM would do. The order of our autocorrelation matrix may be determined objectively and is not a deciding factor in the number of observed peaks *at the level of* "*Burg's MEM approximation.*"

The comments of FR concerning the ability to measure intrinsic line shapes deserve clarification. For ideal (noise-free) data, all three parameters of a (say) Gaussian peak can be determined *exactly* by only three data points, independent of the step size used, be it 2 cm^{-1} or 2000 cm^{-1} (for example). For real data (with noise) oversampling is obviously necessary. The presence of noise is the *only* reason that step size is relevant. If we consider a Gaussian function with a FWHM of 54 cm^{-1} which is sampled at 2 cm^{-1} steps, we have, for example, 27 data points with intensity greater than half the peak height from which three parameters can be extracted with statistical meaning. Statistical error [i.e., the signal-to-noise

ratio (SNR)] will, of course, place limitations on our methodology. We will address this issue in detail elsewhere for simulated data with various levels of statistical noise [5]. In processing *real* data, however, systematic errors are also extant, the most significant one of which is a determination of the background. Indeed, it is just this source of error which has prevented us from estimating the error associated with our peak positions, intensities, and widths. We are continuing to address this crucial issue which is independent of the merit of our methodology.

Finally, we comment on the maximum likelihood and Bayesian methods mentioned by FR. From an information point of view, it is a misconception that division and multiplication in the transformed domain are qualitatively different. All schemes must include noise properly. It is another misconception that resolution enhancement is *only* limited by the SNR in these methods. For noise-free data the final resolution will obviously be limited by the ordinate spacing of the numerical array that is used, a limitation that does not exist in our method [2,5]. Finally, it is very important to note that the maximum entropy principle also states that if we have information (i.e., any *a priori* knowledge), we *must* incorporate it into the processing. For example, if we know the intrinsic line shapes in EELS are Voigt functions, that information *must* be used. Whereas our method meets this criterion, the maximum likelihood and Bayesian methods do not.

Y. Wang and W. H. Weinberg
Department of Chemical Engineering
University of California
Santa Barbara, California 93106

[1] B. G. Frederick and N. V. Richardson, preceding Comment, Phys. Rev. Lett. **73**, 772 (1994).
[2] Y. Wang and W. H. Weinberg, Phys. Rev. Lett. **69**, 3326 (1992).
[3] W. H. Press, B. P. Flannery, S. A. Teukolsky, and W. T. Vetterling, *Numerical Recipes* (Cambridge Univ. Press, Cambridge, 1992), 2nd ed.
[4] C. Lanczos, *Linear Differential Operators* (D. von Nostrand, London, 1961), p. 132.
[5] Y. Wang and W. H. Weinberg (to be published).

773

5

surface science

Enhancing the resolution of electron energy loss spectroscopy by digital signal processing techniques

Youqi Wang and W. Henry Weinberg

Department of Chemical Engineering, University of California, Santa Barbara, CA 93106-5080, USA

A novel spectra analysis method is outlined which enhances markedly the resolution of high-resolution electron energy loss spectroscopy. The method involves Fourier transformation of the measured spectrum, followed by deconvolution of the instrument response function, spectral estimation using the maximum entropy method, and a line shape analysis with Gaussian and Lorentzian functions. In this way broadening due to the instrument response is eliminated, and both the spectral resolution and sensitivity are improved dramatically. The merits of the method are demonstrated with HREELS data for the CO/Ru(001) system for which there are also comparable data from FTIR experiments.

Despite the many advantages of electron energy loss spectroscopy (EELS) compared to optical spectroscopies, one major disadvantage has always been its relatively poor resolution [1–4]. Thus, the so-called "high-resolution" EELS generally refers to those spectra with a resolution of 80 cm^{-1} or below, defined by the full-width at half-maximum (FWHM) of the elastically scattered peak. In the past 25 years, the major advances in EELS have involved hardware development, culminating with the recent report of a resolution of approximately 8 cm^{-1} by Ibach's group [5]. In this paper, we outline a new approach to attack the problem, which is based on advances in signal processing. With the use of several standard digital signal processing techniques, this approach achieves the ultimate resolution of an EEL spectrum by eliminating completely the broadening due to the instrument response function, and, at the same time, provides a dramatic increase in the signal-to-noise ratio (SNR).

It is well known that an observed EEL spectrum is the convolution product of the transfer function of the chemical or physical system being studied and the instrument response function plus a noise term, i.e.,

$$s(E) = i(E) * c(E) + n(E), \qquad (1)$$

where $s(E)$ is the observed EEL spectrum as a function of loss energy E, $i(E)$ is the instrument response function, $c(E)$ is the transfer function of the system under study, $n(E)$ takes into account the presence of noise, and the symbol $*$ denotes the convolution operation. Since the main goal of an EEL experiment is to obtain $c(E)$, it is obvious from eq. (1) that there are two ways of approaching this goal. The first approach is to improve the instrumental hardware to narrow the instrument response function as much as possible, whereas the other is to eliminate $i(E)$ numerically from the measured EEL spectrum. It is this second approach that we describe here.

Fourier transforming eq. (1) gives

$$\frac{S(\tau)}{I(\tau)} = C(\tau) + \frac{N(\tau)}{I(\tau)}, \qquad (2)$$

where capital letters denote the functions of eq. (1) in the Fourier domain, and τ is the conjugate variable of E which we call a pseudo-time vari-

6

able. Notice that $i(E)$, and thus $I(\tau)$, is well defined and contained in an EEL spectrum. Consequently, the left-hand side of eq. (2) is also well defined. Therefore, we can define a quantity, $C'(\tau)$, which is the observed EEL spectrum in the pseudo-time domain without instrumental broadening, as follows:

$$C'(\tau) = C(\tau) + N'(\tau),\qquad (3)$$

where $N'(\tau) = N(\tau)/I(\tau)$ represents noise in the pseudo-time domain. Ideally, if the noise term in eq. (3) can be neglected, then by taking the inverse Fourier transform, we may obtain the true system transfer function, $c(E)$. Unfortunately, this ideal situation never occurs in the real world. Thus, in a classical deconvolution process, a window function has to be introduced, directly or indirectly, in order to suppress the noise. The effect of any kind of windowing can be seen easily by multiplying eq. (3) by a window function, $W(\tau)$, and taking the inverse Fourier transform, which gives

$$s_{\text{final}}(E) = w(E) * c(E) + w(E) * n'(E).\qquad (4)$$

It is evident from eq. (4) that in a classical deconvolution process, the instrument response function is merely replaced by a window function. We should emphasize that although many kinds of deconvolution procedures exist in the literature, they can all be converted into the form of eq. (4) or its equivalent.

The heart of our new processing method [6] is the use of maximum entropy spectral estimation (MESE) [7,8] in connection with eq. (3). The essence of MESE may be stated as follows: given an observation in a limited time domain (real or pseudo), it must produce a spectral estimation which is consistent (usually in the sense of least mean-square deviation) with the observation, while the entropy (viz. information) outside the observation region is maximized. In order to use MESE, one needs to define a cut-off value of τ in eq. (3), τ_{max}, so that

$$C''(\tau) = \frac{C(\tau)}{N'(\tau)} \gg 1, \quad |\tau| < \tau_{\text{max}}.\qquad (5)$$

Applying MESE on $C''(\tau)$ then gives the desired $c(E)$.

We should point out that the fundamental difference between a real-world deconvolution process and a MESE process is that the former
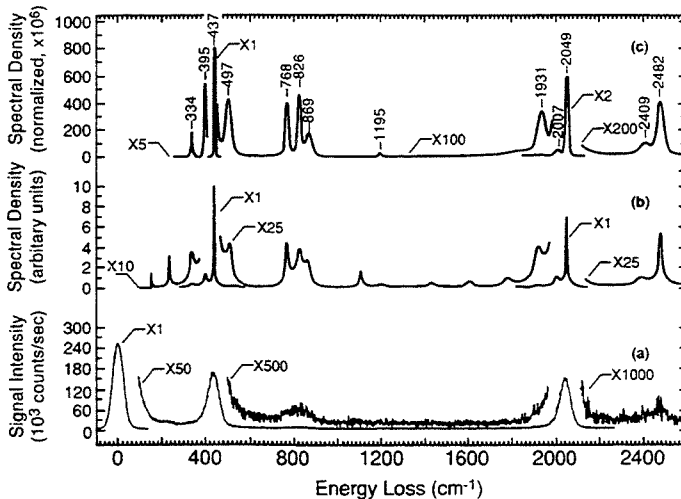

Fig. 1. (a) Measured HREEL spectrum in the specular direction of a saturation coverage of CO on Ru(001) at 300 K; (b) approximate response function of the CO overlayer, derived from eq. (5); (c) HREEL spectrum after complete processing, derived from eq. (7). The raw data in (a) have been smoothed for display purposes.

7

requires the introduction of some false information (i.e., a window function) while the latter simply states the fact that we have no knowledge of the physical system outside the observational region. The evaluation of $c(E)$ for CO chemisorbed on the Ru(001) surface using MESE is shown in fig. 1b. Compared with the raw spectrum shown in fig. 1a (vide infra), which has been smoothed for display purposes, two features are rather evident. First, the peaks have become much sharper in fig. 1b, which is the result of the removal of instrumental broadening. Second, the noise level has been suppressed dramatically in fig. 1b, which is due to two different mechanisms, the first of which is the cut-off introduced in eq. (5) which discards those data points where noise is dominant, and the other of which is the autoregression nature of a MESE process which is insensitive to chaos. Another attractive feature of MESE is that it is most sensitive, in principle, to sinusoidal waves. In our case this means that the more narrow the intrinsic peaks of the spectrum relative to the instrument response function, the better the final spectrum will be, totally opposite to a classical deconvolution process.

Although employing MESE in this fashion will generate a spectrum with superior resolution and sensitivity, which may well be satisfactory for those applications where the only interest is peak recognition, the accuracy of the peak intensity and the line shape is usually not satisfactory, mainly due to the parametric nature of the method. In order to fully recover the information contained in the EEL spectrum, it is necessary to introduce some models for the system under study. Recall that an isolated quantum mechanical oscillator with a finite lifetime has an intrinsic Lorentzian line shape, with inhomogeneous Gaussian broadening. Thus, a reasonable model for a vibrational system may be written, in the Fourier domain, as

$$C_{model}(\tau) = 1 + \sum_{k=1}^{M} h_k \exp\left[-iE_k\tau - \omega_{L,k}|\tau| \right.$$
$$\left. -\left(\frac{\omega_{G,k}}{2}\tau\right)^2 \right], \quad (6)$$

where, h_k is the integral intensity of the kth mode normalized to that of the elastic peak, E_k is the frequency, $\omega_{L,k}$ is the Lorentzian line width, $\omega_{G,k}$ is the Gaussian line width, and the summation is over all modes including multiple scattering events and overtones. Substituting eq. (6) into eq. (2) and rearranging gives

$$N(\tau) = S(\tau) - I(\tau)\left\{ 1 + \sum_{k=1}^{M} h_k \right.$$
$$\left. \times \exp\left[-iE_k\tau - \omega_{L,k}|\tau| - \left(\frac{\omega_{G,k}}{2}\tau\right)^2 \right] \right\}. \quad (7)$$

The final stage of our spectral analysis method involves the application of a nonlinear optimization procedure on eq. (7). Notice that the total number of modes, M, and all four parameters associated with each peak in the spectrum can be estimated, either accurately or approximately, from $c(E)$ which is derived from applying MESE to eq. (5), cf. fig. 1b. Upon completion of the optimization, these parameters allow the reconstruction of the true system transfer function, $c(E)$. An example is shown in fig. 1c. Compared to direct curve fitting in the energy domain, a method used by some research groups [9,10], there are several important differences worth mentioning. First, the number of peaks in a spectrum is determined by MESE rather than by an a priori guess. Second, the elastic peak can be of any shape rather than a strict Gaussian (which never occurs in the real world). Finally, the measured peaks can be either Lorentzian, Gaussian, or their convolution, rather than a pure Gaussian or Lorentzian.

For the purpose of demonstration, we have applied our spectral analysis method to a nearly saturated chemisorbed overlayer of CO on Ru(001), corresponding to a 6 L exposure at room temperature, a system well studied by vibrational EELS [11] and IRAS [12]. The spectrum of fig. 1a was measured with a modest resolution of 54 cm^{-1}, 4096 data points with a channel resolution of 2 cm^{-1}, and a total collection time of 1000 s. Fig. 1b gives the result of the MESE process via Marple's algorithm [13], and fig. 1c is the final

spectrum after complete processing. It is clearly seen from figs. 1b and 1c that there are three different CO stretching modes between 1900 and 2100 cm^{-1}, and five frustrated translations and rotations below 500 cm^{-1} (including one at 226 cm^{-1} which is not shown in fig. 1c). Overtone and combination bands are apparent between 700 and 900 cm^{-1} and between 2400 and 2500 cm^{-1}, and the presence of a trivial amount of hydrocarbon contamination is suggested by the small peak near 1200 cm^{-1} and another one near 2900 cm^{-1} (not shown). The three CO stretching modes have a FWHM of 17 cm^{-1} (for the 2049 cm^{-1} peak), 29 cm^{-1} (for the 2007 cm^{-1} peak), and 43 cm^{-1} (for the 1931 cm^{-1} peak); whereas the correlated frustrated translations at 437, 395, and 334 cm^{-1} have FWHM's of 8, 10, and 9 cm^{-1}, respectively. The IRAS data for the same system gives a band at 2049 cm^{-1} with a FWHM of 12 cm^{-1} [12]. The slightly broader major CO stretching mode and the appearance of the small band at 2007 cm^{-1} in our spectrum suggest that our CO overlayer is not so well ordered as that of ref. [12].

Several final comments are appropriate regarding the spectral analysis method outlined in this paper. First, the successful application of our method is rendered easier by having a high-quality experimentally measured spectrum. Hence, recent advances in spectrometer design remain important [5]. Second, it is evident that the method can be generalized to any spectroscopy for which the instrument response function can be obtained either from experiment or theory, i.e., the method is by no means limited to HREELS. Finally, we should point out that although it is rather easy to obtain information concerning the number of

modes, their position, and their intensities with high accuracy, a definitive determination of line width, and especially line shape, requires much higher SNR in the original data.

References

[1] W.H. Weinberg, in: Solid State Physics: Surfaces, Vol. 22 of Methods of Experimental Physics, Eds. R.L. Park and M.G. Lagally (Academic Press, Orlando, 1985) p. 23.

[2] H. Ibach and D.L. Mills, Electron Energy Loss Spectroscopy and Surface Vibrations (Academic Press, New York, 1982).

[3] F.M. Hoffmann, Surf. Sci. Rep. 3 (1983) 107.

[4] Y.J. Chabal, Surf. Sci. Rep. 8 (1988) 211.

[5] G. Kisters, J.G. Chen, S. Lehwald and H. Ibach, Surf. Sci. 245 (1991) 65.

[6] Y. Wang and W.H. Weinberg, Phys. Rev. Lett. 69 (1992) 3326.

[7] J.P. Burg, in: Proc. 37th Meeting Soc. Explor. Geophys. (1967); Maximum Entropy Spectral Analysis, PhD Dissertation, Stanford University, 1975.

[8] J.N. Kapur, Maximum-Entropy Models in Science and Engineering (Wiley, New York, 1989), and references therein; Modern Spectrum Analysis, Ed. D.G. Childers (IEEE Press, New York, 1978).

[9] B. Voigtlander, D. Bruchmann, S. Lehwald and H. Ibach, Surf. Sci. 225 (1990) 151.

[10] C. Astaldi, A. Bianco, S. Modesti and E. Tosatti, Phys. Rev. Lett. 68 (1992) 90.

[11] G.E. Thomas and W.H. Weinberg, J. Chem. Phys. 70 (1979) 1437.

[12] H. Pfnür, D. Menzel, F.M. Hoffmann, A. Ortega and A.M. Bradshaw, Surf. Sci. 93 (1980) 431.

[13] L. Marple, IEEE Trans. Acoust. Speech Signal Process. ASSP-28 (1980) p. 441.

9

ULTRA-HIGH RESOLUTION ELECTRON ENERGY LOSS SPECTROSCOPY
—PROCESSING STRATEGY

by

Youqi Wang

Department of Chemistry

California Institute of Technology

Pasadena, California 91125

and

W. H. Weinberg

Department of Chemical Engineering

University of California at Santa Barbara

Santa Barbara, California 93106-5080

ABSTRACT

The methodology of ultra-high resolution electron energy loss spectroscopy (UHREELS) is described in detail with graphical examples of real data processing. On the basis of modern digital signal processing techniques, this method promised to yield EEL spectra with ultimate resolution and superior signal to noise ratio (SNR).

As has been demonstrated in [1], the UHREELS methodology offers a new approach to overcome the poor resolution suffered by EELS and similar spectroscopic technologies. Considering the simplicity and maturity of the theories that this method is based on, we think it's appropriate at this time to concentrate mainly on the operational aspects of the method and leave theoretical revelation to future publications. Thus the organization of this writing is to follow the strategy as the method is at work. Graphical examples of EEL spectra taken from atomic hydrogen on Ru(001) surface presaturated with CO at various processing stages are given for illustration purposes. Results and discussions specific to that system is published elsewhere [2]. Note that many comments and suggestions in this paper are based on our observations of both real data processing and simulated data testing. Since including the later is beyond the scope of this paper, we postpone it also to the future publications. We should point out that the method alters quite a bit the way we do EEL experiments. Since experimental aspects themselves are not simple issues, we only include those that are very necessary at this moment and leave complete descriptions to the future.

1. PREPROCESSING

Preprocessing is one of the most crucial stages that have great influence on the quality and reliability of the final result.

1.1 Data Repairing

Any data point in a given spectrum that was corrupted by spark-like noises needs to be repaired. Since noise contained in a data channel obeys Poisson distribution, it is easy to recognize sparks, given the mean value for that channel. If multiple scan method is used, this is a trivial job. If only single scan data are available, local smoothing method

may be used. In either cases, the new value should be calculated exclusive of the spark detected, thus it is in principle an iterative process.

1.2 Baseline Removal

One major contribution to the baseline in a given spectrum is due to the dark current of electron multiplier. Another is electrical noise from preamplifier. Although it may appear as small as 1 cps, it is on the same order or even higher relative to the detection limit of our method. Furthermore, it has large influence on the determination of signal line widths and line shapes, thus cannot be ignored. In recognizing the baseline, one can extensively smooth the raw data and determine the parameters from the resultant spectrum graphically. Caution must be made on both ends of the raw data during smoothing. Keep alert that big peaks will raise the neighborhood spectral level after smoothing. It is also worth to keep accurate records of noise level of the instrument before and after data acquisition and compare them with the parameters obtained from the spectrum. Note that dark current is a function of vacuum pressure, thus one should wait long enough after chemical dosage before taking spectrum.

1.3 Counting Loss Correction

It is well known that counting loss is unavoidable when electron counting techniques are used [3]. It is ignored in normal EEL experiments, since elastic peaks are of no particular interest. This is no longer the case in our processing method where elastic peaks are used as the representative of instrument response function [1]. The following equation may be used [3] to correct counting loss,

$$s(E)_{corrected} = \frac{s(E)_{measured}}{1 - s(E)_{measured} / r_{max}},$$

(1)

where r_{max} is the counting rate limit of the detector system used. Note that the behavior of electron multiplier is a complex issue and the model that results in Eq. (1) is only an approximation. Thus, one should avoid too high counting rates in a spectrum (relative to r_{max}) that require large corrections.

2. DETERMINING ELASTIC PEAK

Two types of method may be used. One is based on the utilization of the convolution property possessed by a given spectrum [1],

$$s(E) = i(E)*c(E) + n(E). \qquad (2)$$

The other is based on pattern recognition techniques. While the former is theoretically simpler and computationally easier, it is not problem free. On the other hand, pattern recognition method requires intensive human involvement, therefore may bring human errors into the processing. The best way is the combination of both techniques. Although computationally more complicate, it insures the quality of the result. Detailed description is obviously beyond the scope of this paper and has to be postponed to future publication. Note that elastic peaks are generally asymmetric and different from data to data. This step has to be performed for every single spectrum. Fig. 1 shows an example for fitting the elastic peak by our method.

3. SPECTRUM SEPARATION

3.1 Separating Elastic Peak

After subtracting elastic peak from raw data, it is necessary to zero pad the elastic peak zone to prevent excessive noises to be brought into processing stages that follow. This may be clarified by the following example. Suppose the elastic peak maximum in a spectrum is about 5×10^5 cps, thus the average noise level around that maximum is on the order of 7×10^2 cps. After subtraction, the elastic peak zone is then dominated by random noises on this order of magnitude (RMS) as shown in Fig. 2a. This is orders higher than most of the signals in the spectrum. Worse than that, the noise is narrow banded, thus will yield strong ripples in the pseudo-time domain.

Zero padding does have its tradeoffs: any signals in the same zone, i.e., those very low frequency peaks will also be blanked out, and nearby peaks may be distorted if their tails happen to extend into this zone. This is evident as shown in Fig. 2b. Note that even an intrinsically very narrow peak will have a profile at least as wide as the elastic peak in the raw spectrum. Zero padding may not be necessary if the residue noise in the elastic peak zone has about the same magnitude as those in the rest of a spectrum, which is frequently the case for typical off-specular spectra.

We emphasize here that it is more important to tune an instrument to yield an elastic peak with narrower tail rather than narrower FWHM for the reason indicated above and those that will be discussed later.

3.2 Removing Broad Band Profiles

Broad band profiles are commonly observed in an EEL spectrum, often appear at the loss side of the elastic peak and may extend over the entire raw data. The origins of these profiles are system dependent. It may be caused by elastically scattered electrons reflected from analyzer walls that get into the detector as pointed out by Ibach and Mills

[4]. It may also be true signals like graphitized carbon contamination on some transition metals or bulk phonon band from semiconductor experiments. It is important not to confuse these profiles with the elastic peak tail in a given spectrum. The later may be distinguished by observing that similar tails also attached to loss features or by convolution analysis as mentioned in section 2. The necessity of this step is due to the fact that MESE is powerful in recognizing narrow band signals but performs poorly on wide band signals [5].

4. DECONVOLUTION

4.1 Data Expansion

The convolution process physically performed by the instrument as shown in Eq. (2) is linear in nature. Accordingly, deconvolution should also be performed linearly. Thus, both raw data and elastic peak profile should be expanded by zero padding on the same side (left or right) to at least the length that is the sum of the original lengths of the two data files. The expanded data can then be Fourier transformed. One should make sure that there is practically no discontinuity in both raw data and elastic peak profile. Whenever possible, keep the overall data length at its minimum to reduce the total band width.

4.2 Determining Average Noise Level

According to Eq. (2), spectrum data obey the following relationship in the pseudo-time domain,

$$S(\tau) = I(\tau) \cdot C(\tau) + N(\tau). \tag{3}$$

Eq. (3) indicates that most part of the time domain will be dominated by noises, since instrument response function is usually broad in energy domain thus narrow in time domain as can be seen in Fig. 3(b). For a typical EEL spectrum, this is usually more than 95% of total data points and noises are white-like, as is evident in Fig. 3(a). It is thus reasonable to assume that noise is white in the entire time domain including where signals are dominant. Based on this assumption, we can easily estimate the average noise level in the time domain,

$$RMS = \left(\frac{1}{n} \sum_{\tau_0 \leq \tau \leq \pi} |S(\tau)|^2 \right)^{\frac{1}{2}}, \tag{4}$$

where n is the data points involved in the summation and τ_0 is where noises starts to have absolute dominance that can be determined graphically or simply take a large enough value like $\pi/4$. Fig. 4(a) indicates that the harmonics due to signals is gone after about 300 time units for our example data and Fig. 4(b) shows that the noise estimation, Eq. (4), is quite close to the truth, since the noise curve traces the spectral data quite closely after 300 units.

4.3 Determining τ_{max}

This step may be performed after deconvolution,

$$S'(\tau) = \frac{S(\tau)}{I(\tau)} = C(\tau) + \frac{N(\tau)}{I(\tau)} = C(\tau) + N'(\tau), \tag{5}$$

where the division only needs to be calculated from $\tau = 0$ up to the first occurrence where $|S'(\tau)| \geq |S'(0)|$ due to the fact that $|C(0)| \geq |C(\tau)|$ and $|N'(\tau)| \propto 1/|I(\tau)|$. The location of the first non-incident crossing point of the data curve, $|S'(\tau)|$, and the noise curve,

17

$RMS / |I(\tau)|$, indicates where noise starts to dominate and τ_{max} should generally be on the left side of this point. For our data, the crossing point is around 212 time units as can be seen in Fig. 5(a), thus τ_{max} may be chosen as 212 units or smaller for this spectrum. Notice that there are still some harmonics exist after the crossing point.

5. MESE

5.1 Constructing Autocorrelation Matrix

Autocorrelation matrix, $\hat{R}$, can be constructed as follows,

$$R_{i,j} = \sum_{n=p-L}^{L} \left\{ w_{|n|}^2 \cdot x_{n-i}^* \cdot x_{n-j} \right\}, \tag{6}$$

where,

$$
\begin{aligned}
w_k &= |I(\tau_k)| \\
x_k &= \begin{cases} S'(\tau_k), & k \geq 0 \\ S'(\tau_k)^*, & k < 0 \end{cases} \\
p &\approx (2L+1)/3 \\
i,j &= 0,1,\ldots,p,
\end{aligned}
\tag{7}
$$

and L is the data index corresponds to τ_{max} and p is the AR model order. Note that the definition of the autocorrelation matrix here is different from those in the literature [5,6]. Derivation of Eq. (6) will be seen in future publication.

5.2 Calculating AR Vector

The linear prediction coefficient vector, $\bar{\alpha}$, can be obtained by solving the following matrix equation,

$$\hat{R}\bar{\alpha}' = \bar{\beta},\tag{8}$$

where,

$$\bar{\alpha}' = \left(\alpha_0', \alpha_1', \ldots, \alpha_p'\right)^T$$
$$\bar{\beta} = (1, 0, \ldots, 0)_{p+1}^T \tag{9}$$
$$\bar{\alpha} = \frac{\bar{\alpha}'}{\alpha_0'}$$

and T denotes transpose operation.

The best way to solve Eq. (8) is to use Singular Value Decomposition (SVD) procedures [7,8]. Briefly, any matrix can be decomposed into the following form,

$$\hat{A}_{MXN} = \hat{U}_{MXN} \cdot \hat{D}_{NXN} \cdot \hat{V}_{NXN}^H$$
$$\hat{U}^H \cdot \hat{U} = \hat{I} \tag{10}$$
$$\hat{V}^H \cdot \hat{V} = \hat{V} \cdot \hat{V}^H = \hat{I}$$

where $\hat{D}$ is a real diagonal matrix, $\hat{I}$ is unity matrix and H denotes Hermitian conjugate operation. Note that the autocorrelation matrix, $\hat{R}$, can be rewritten as,

$$\hat{R} = \hat{A}^H \cdot \hat{A}$$
$$A_{i,j} = w_{|p-L+i|} \cdot x_{p-L+i-j} \tag{11}$$
$$i = 0, 1, \cdots, 2L - p$$
$$j = 0, 1, \cdots, p$$

19

By using SVD to decompose the data matrix, $\hat{A}$, and utilize the properties of Eq. (10), we then have,

$$\bar{\alpha}' = \hat{V} \cdot \hat{D}^{-2} \cdot \hat{V}^H \cdot \bar{\beta}. \tag{12}$$

Particularly,

$$\alpha'_0 = \sum_{j=0}^{p} \left\{ V^*_{0,j} \cdot V_{0,j} \cdot D^{-2}_{j,j} \right\} > 0, \tag{13}$$

which is the required property by definition.

Alternatively, one may want to use a triangular decomposition similar to Cholesky decomposition [7-9] in saving memory and CPU time. Notice the Hermitian symmetry of the autocorrelation matrix in Eq. (6). Thus, $\hat{R}$ can be decomposed into

$$\hat{R} = \hat{T} \cdot \hat{D} \cdot \hat{T}^H, \tag{14}$$

where $\hat{T}$ is a lower triangular matrix with its diagonal elements equal to 1. Eq. (8) can then be solved by forward substitution, division and backward substitution. The advantage of this method is to speed up the calculation by almost 50 times and requires less than 1/6 of the memory compared to the SVD procedure. The disadvantage is the loss of precision due to the summation in Eq. (6). The property of Eq. (13) may not be maintained due to round-off errors in computation.

5.3 Obtaining System Transfer Function

Once $\bar{\alpha}$ is known, the system transfer function, $c(E)$, can easily be calculated as,

$$c(E) \approx \frac{1/|\alpha_0'|}{\left| \sum_{k=0}^{p} \alpha_k \exp\left[i2\pi k \frac{E}{L_E} \right] \right|}, \tag{15}$$

where L_E is the expanded data length in the energy domain. Note that $c(E)$ thus obtained is a periodic function of E with periodicity of L_E. Further note that the center of the elastic peak is now at $E = 0$. When plotting, care must be taken not to take energy step too large or some sharp peaks may be missed. On the other hand, one only needs to plot out the same energy range as the raw data and the rest should be ignored. It is also a good practice to do the same zero blanking in the elastic peak zone as for raw data to recognize the chopping effect. Fig. 6 shows examples of such plotting.

5.4 Spectral Scaling

The scaling relationship can easily be derived from Eq. (2) with the white noise assumption,

$$\int_{-\infty}^{+\infty} s(E)dE = \int_{-\infty}^{+\infty} i(E) * c(E)dE + \int_{-\infty}^{+\infty} n(E)dE$$
$$= \int_{-\infty}^{+\infty} i(E)dE \cdot \int_{-\infty}^{+\infty} c(E)dE \tag{16}$$

6. PEAK INTENSITIES

6.1 Peak Search

The easiest way is derivative method by taking the second derivative of the spectrum obtained from Eq. (15) and searching for zero-crossing pairs. The number of peaks is then

the number of pairs found, the peak center is the middle point of each pair and FWHM is 86.6% of the pair width (assuming Lorentzian line shape). Note that smoothing may be cooperated into numerical derivatives to avoid perturbation from insignificant digits. We recommend to use moving average method, e.g.,

$$f_i'' \propto 5(f_{i+3} + f_{i-3}) - 4f_i - 3(f_{i+1} + f_{i-1}).$$

(17)

The above equation is derived from second order polynomial with seven data points and the proportional constant was dropped out. Note that zero crossing point may be calculated by linear interpolation to preserve accuracy.

It is understandable that separation of closely spaced signals is difficult. In principle, the higher order the derivative is taken, the cleaner the separation will be, but orders higher than second will cause analytical complicity and numerical instability. Incomplete separation, on the hand, would result in shift of peak centers from their true positions for those involved. Likewise, peak widths may also be influenced. The degree of interference depends naturally on how close signals are spaced, their widths and their relative heights. At the worst, some peaks may be inseparable by the derivative method.

6.2 Intensity Calculation

Direct integration on Eq. (15) has limited usage. It is better to do calculation on the original spectrum with delta function approximation [1]. There are two ways to fulfill the task. One is do calculation in the Fourier domain and the other is in energy domain. While the former is simpler, the later is more accurate. The general equation is as follows,

$$\hat{A}\,\vec{h} = \vec{y},$$
$$\vec{h} = (h_1, h_2, \ldots, h_M)^T,$$

(18)

where M is the number of peaks found. For Fourier domain calculation,

$$A_{i,j} = \sum_{\tau=0}^{\tau_{max}} w_\tau^2 \cdot \cos\left[\left(E_i - E_j\right) \cdot \tau\right],$$

$$y_k = \sum_{\tau=0}^{\tau_{max}} w_\tau^2 \cdot \text{Re}\left[S'(\tau) \cdot e^{iE_k\tau}\right].$$

$$(19)$$

For energy domain calculation,

$$A_{j,k} = \sum_{E=E_L}^{E_R} i(E - E_j) \cdot i(E - E_k),$$

$$y_k = \sum_{E=E_L}^{E_R} i(E - E_j) \cdot s(E).$$

$$(20)$$

In both cases, the indexes are ranging from 1 to M, and E_i is the center of the ith peak, E_L and E_R are the boundaries of the raw spectrum section being processed. Eq. (19) and (20) are derived from the following equations,

$$\nabla_{\vec{h}} \chi_F^2 = \nabla_{\vec{h}} \left\{ \sum_{\tau=0}^{\tau_{max}} w_\tau^2 \left| \sum_{k=1}^{M} h_k e^{-iE_k\tau} - S'(\tau) \right|^2 \right\} = 0$$

$$\nabla_{\vec{h}} \chi_E^2 = \nabla_{\vec{h}} \left\{ \sum_{E=E_L}^{E_R} \left[\sum_{k=1}^{M} h_k \cdot i(E - E_k) - s(E) \right]^2 \right\} = 0$$

$$(21)$$

Note that for energy domain calculation, the basis functions are the replica of the instrument response function shifted to new positions. If it is not easy to do so directly, one may use the Fourier transform method as the following,

$$i(E - E_k) = IFT\left[I(\tau) \cdot e^{-iE_k\tau}\right],$$

$$(22)$$

where *IFT* indicates inverse Fourier transform.

The accuracy of the intensities calculated from Eq. (18) is obviously a function of the truthfulness of the delta function assumption. Thus, it is unreasonable to expect an accurate result for those signals that are as broad as, or even broader than, the elastic peak. On the other hand, noise has the least influence to the intensity compared to other parameters, such as position, line width and line shape. This feature makes quantitative comparison possible. One should be aware that the intensity thus obtained is normalized by elastic peak and this is a necessity when different spectra are in comparison.

Note that the results of intensity calculation are not necessarily all positive. There are two categories for those negative peaks. One indicates the existence of dips in the original data. Since Eq. (15) only take positive value, they may appear as peaks in MESE spectrum. This type of peaks is featured by their location that is remote to other peaks and where noise level is high or small sparks are not cleaned away in the raw data. The other category is an indication that a signal peak nearby is either sharper than Lorentzian, e.g., Gaussian, or its tail was chopped off in the original data. This type of peaks thus always appears near some other signal peaks. Note that the later case is a sufficient but not necessary condition in line shape justification, i.e., a signal peak could be more Gaussian like or its tail being chopped away without having a negative peak on its side.

For most of the spectra that we have processed, it appears that a Lorentzian function approximation usually gives better estimation of peak intensities than delta function approximation. Thus, Eq. (19) may be modified to the following,

$$A_{i,j} = \sum_{\tau=0}^{\tau_{max}} w_\tau^2 \cdot e^{-(W_{L,i}+W_{L,j})\tau} \cdot \cos\left[\left(E_i - E_j\right)\tau\right],$$

$$y_k = \sum_{\tau=0}^{\tau_{max}} w_\tau^2 \cdot e^{-W_{L,k}\tau} \cdot \mathrm{Re}\left[S'(\tau) \cdot e^{iE_k\tau}\right],$$

(23)

where $W_{L,k}$ is the Lorentzian width for the kth peak and can be estimated from MESE spectrum. The calculation of Eq. (18) can then only be done in the Fourier domain.

7. LINE SHAPE ANALYSIS

Line shape analysis is basically a curve fitting procedure [10]. It is different from a normal fitting process in that the operation is performed in the Fourier domain where the distortion due to the instrument response function has been removed completely. Another important difference compared to energy domain curve fitting schemes [11,12] is that the size of the basis functions is determined *objectively* from MESE result instead of some *a priori* knowledge. On the other hand, it still bears the same requirement of choosing the type of basis functions. The advantage of performing curve fitting in the Fourier domain is then that some physically important functions can be expressed in a simple form while their correspondence in energy domain may not.

7.1 System Model

It is well known that a quantum mechanical oscillator has an intrinsic Lorentzian line shape, while inhomogeneous environment with small random perturbation will convolute that line shape with Gaussian distribution function. Thus, a reasonable choice of the format of basis functions in Fourier domain is the product of an exponential function and a Gaussian function as follows,

$$B_k(\tau) = h_k \exp\left[-iE_k\tau - W_{L,k}|\tau| - \left(\frac{W_{G,k}}{2}\tau\right)^2 \right], \tag{24}$$

where, h_k, E_k, $W_{L,k}$, $W_{G,k}$ are the intensity, peak position, Lorentzian width and Gaussian width for the kth peak, respectively. With the basis function of Eq. (24), we can construct the system model as,

$$C_{Model}(\tau) = \sum_{k=1}^{M} B_k(\tau), \qquad (25)$$

and the object function is then,

$$\chi_C^2 = \sum_{\tau=0}^{\tau_{max}} w_\tau^2 |C_{Model}(\tau) - S'(\tau)|^2 \qquad (26)$$

Note that the size of the basis in Eq. (26), M, may be different from the number of peaks obtained from MESE spectrum. Those negative peaks that associated with other peaks must be excluded since they are the compensating components for sharper signals (sharper than Lorentzian). For stability reason, it is better not to allow intensity to take negative values during optimization, thus negative dips may also be excluded. With these two exceptions, all other peaks should, in general, be kept as input.

7.2 Algorithm

The best algorithm for the optimization is the Levenberg-Marquardt method [7]. Note that the gradient vector and the curvature matrix derived from Eq. (26) (we exclude the expressions here due to its complicity) can both be expressed as real numbers and the curvature matrix can be shown to be positive definite. Thus, Cholesky decomposition [9] may be used without modification. It is worth including the second partial derivatives in the curvature matrix. This will lengthen the time in calculating matrix elements, but speeds up convergence, thus overall time is less.

7.3 Starting Point

Minimizing Eq. (26) is obviously a non-linear process, thus it is important to have a good starting point. MESE usually gives accurate determination of peak positions and this turns out to be the most influential parameters during the optimization. Intensities also have great effect on the process, while good estimation can be made from Eq. (18). The line widths are not very sensitive to the procedure compared to the two factors just mentioned. This implies that the uncertainty of line widths may be bigger than position and intensity. It also implies that the line widths from MESE may be used as initial trial values for Lorentzian line widths. Naturally, initial value of Gaussian width should generally be set to zero or a small fraction of Lorentzian widths.

7.4 Optimization Strategy

Due to the least-square nature in minimizing Eq. (26), it is important not to start full optimization right away or some small peaks may be driven out of their true position in the hyper space and may never come back to it. Note that, among the four parameters for each peak, the most uncertain one is the Gaussian line width, the next uncertain one is the Lorentzian line width, the intensity is usually fairly close to the truth and the peak position is the most certain parameter. Thus it is a good practice to take a four phase strategy for the optimization task. At phase 1, only $W_{G,k}$ are optimized while the rest of the parameters are fixed. At phase 2, both $W_{L,k}$ and $W_{G,k}$ are optimized. At phase 3, only the peak positions are fixed and at the final stage, all the parameters are optimized. Although it seems more complicate, the performance is much better, characterized by its faster convergence and lower object function value, Eq. (26). After the final phase of processing, it is worth inspecting the resultant spectrum in both the time domain and energy domain, as shown in Fig. 5 and Fig. 7, to insure the quality and seek for further improvement.

8. SIGNAL RECOGNITION

Peak assignment and signal recognition are different in this contest. While the former is to assign signal peaks to its physical contents, the later is to justify if a peak is a signal, that is the issue in this section. Due to the space limitation, we only give brief discussion here.

8.1 Spectral distortion

One major source of spectral distortion is the zero padding in the elastic peak zone as mentioned before. Thus, peaks near that region are usually not very trustful, especially their shapes. Similar situation may also happen at the right end of a spectrum due to the discontinuity of data. Another source is spark-like noise corruption that is small enough to escape statistical check in section 1.1 but large enough to either give false signals or distort true signals nearby. This usually happens to small signals as in the high energy region of the spectra shown in Fig. 6 and Fig. 7.

8.2 Broad Band Signals

The major problem of MESE treatment is that it cannot handle broad band signals properly. As has been demonstrated in [5], a broad band signal will result in several sharp peaks in MESE spectrum that is indistinguishable from the case where a broad profile is actually composed by several sharp signals. Note that line shape analysis will not help to clarify the situation, since it only gives a better description of a true system response function that may look broad even without instrumental broadening (cf. Fig. 7(a)). Thus, justification may either based on the physical understanding of the system being studied or the reproducibility of spectral features. The basis for the later is that the splitting of broad band signals is a strong function of AR orders and noise characters that will vary from spectrum to spectrum while true signals should not be changed. From this point of

view, we can justify that most peaks resolved from Fig. 6 are true signals since Fig. 6(a) and Fig. 6(b) were from the spectra taken at different times from the same (almost) physical system but different AR orders and noise figures.

8.3 Resolvability

In our methodology, the signal resolvability is mainly based on MESE. Besides the possibility of false signals due to broad band signal splitting as discussed above, the opposite situation may also happen, i.e., MESE may fail to resolve two closely spaced signals. The major factor to degrade resolvability is the resource limitation, i.e., the order of the autocorrelation matrix, p. When information content in a given spectrum is high, it requires higher order, but the later is limited by the available data in the time domain. Comparison of simulated spectrum and real data processing shows that, for a given order p while varying the data lengths, MESE yields virtually identical spectra, indicating that they are stable to noise.

The procedure described in section 4.3 is a conservative approach. Frequently, one may find that some part of the data points on the right side of noise curve crossing point may still be usable. When this kind of situation is encountered, we use smaller data size first and run through the whole procedure. At the end of the processing, we compare the optimized model, Eq. (25), to the raw data in the Fourier domain. This gives a good justification that if we could include those data points in the calculation. In the case of our example data, comparison of Fig. 5(a) and Fig. 5(b) shows that the data points between 212 and 265 time units still contain fair amount of signals, thus are safe to use. After redo the calculation, it is necessary to check again to make sure that the decision was made right, as indicated in Fig. 5(c). Note that there are other alternatives to increase resources or reduce demands. Details have to be postponed to the future.

9. CONCLUSION

The UHREELS methodology has been described in detail that offers a novel approach that one can follow to achieve scientific accomplishment that may not be expected before. While a lot more information can now be extracted from a single experiment, the method also put a much higher standard for the definition of a *good* spectrum.

REFERENCE

[1]   Y. Wang and W. H Weinberg, Phys. Rev. Lett. **69** (1992) 3326; Surf. Sci. **287/288** (1992) 1102.

[2]   W. J. Mitchell, J. Xie, Y. Wang, and W. H. Weinberg, J. Electron Spec. Related Pheno. **64/65** (1993) 427.

[3]   E. Bleuler, in *Electronic Methods*, *Methods of Experimental Physics* Vol. 2, E. Bleuler and R. O. Haxby ed. (Academic, New York, 1975), Chapter 9.1, and references therein.

[4]   H. Ibach and D. L. Mills, *Electron Energy Loss Spectroscopy and Surface Vibrations* (Academic, New York, 1982).

[5]   S. M. Kay and S. L. Marple, Proc. IEEE **69** (1981) 1380.

[6]   L. Marple, IEEE Trans. Acoustics, Speech, and Signal Process. **28** (1980) 441.

[7]   W. H. Press, S. A. Teukolsky, W. T. Vetterling and B. P. Flannery, *Numerical Recipes*, 2nd ed. (Cambridge, Cambridge, 1992) and references therein.

[8]   C. L. Lawson and R. J. Hanson, *Solving Least Squares Problems* (Prentice-Hall, 1974).

[9]   J. C. Nash, *Compact Numerical Methods for Computers* (Adam Hilger, 1979).

[10]   W. F. Maddams, Appl. Spectrosc. **34** (1980) 245.

[11]   B. Voigtländer, D. Bruchmann, S. Lehwald, and H. Ibach, Surf. Sci. **225** (1990) 151.

[12]   C. Astaldi, A. Bianco, S. Modesti, and E. Tossatti, Phys. Rev. Lett. **68** (1992) 90.

FIGURE CAPTION

Fig. 1. Fitted elastic peak compared to raw data. The spectrum was taken at on-specular direction for the experiment of dosing 200L atomic hydrogen on Ru(001) surface at 150K presaturated with CO. Data length 4096 channels. Step resolution 1 cm^{-1}. Total acquisition time 682s. Raw data has been smoothed before processing.

Fig. 2. Zero padding elastic peak zone: (a) after removal of elastic peak, (b) after zero padding.

Fig. 3. Spectral data of Fig. 1 in the pseudo-time domain: (a) $|S(\tau)|$, (b) $|I(\tau)|$. The raw spectrum and elastic peak profile were expanded by 4 times due to the slow decay of the elastic peak tail. Forward Fourier transform was used without scaling. Only the first quarter of the data is shown. Note that both (a) and (b) are symmetric about the time origin.

Fig. 4. Comparison of $|S(\tau)|$ and $|S'(\tau)|$: (a) signal dominated portion of $|S(\tau)|$; (b) $|S'(\tau)|$ versus $RMS / |I(\tau)|$ (the smooth one).

FIG. 5. Determining τ_{max}: (a) data curve versus noise curve around crossing point (notice the harmonics is almost gone after 265); (b) $|C_{Model}(\tau)|$ resulted from the processing of $\tau_{max}= 212$ and $p = 141$; (c) $|C_{Model}(\tau)|$ resulted from the processing of $\tau_{max}= 265$ and $p = 177$.

Fig. 6. MESE spectra calculated from (a) the raw spectrum as in Fig. 1; (b) from similar experiment as (a) with 450L atomic hydrogen dosage and spectrum was taken three weeks apart with acquisition time 410s. Note that electrical measurement of sweep width

and the true spectral range may not be identical and calibration should be made before the units conversion. Also note that calibration factor is instrument and configuration dependent.

Fig. 7. Quality of the processing: (a) $c(E)$, (b) $s(E)$, (c) $i(E)*c(E)$, (d) $n(E)$.
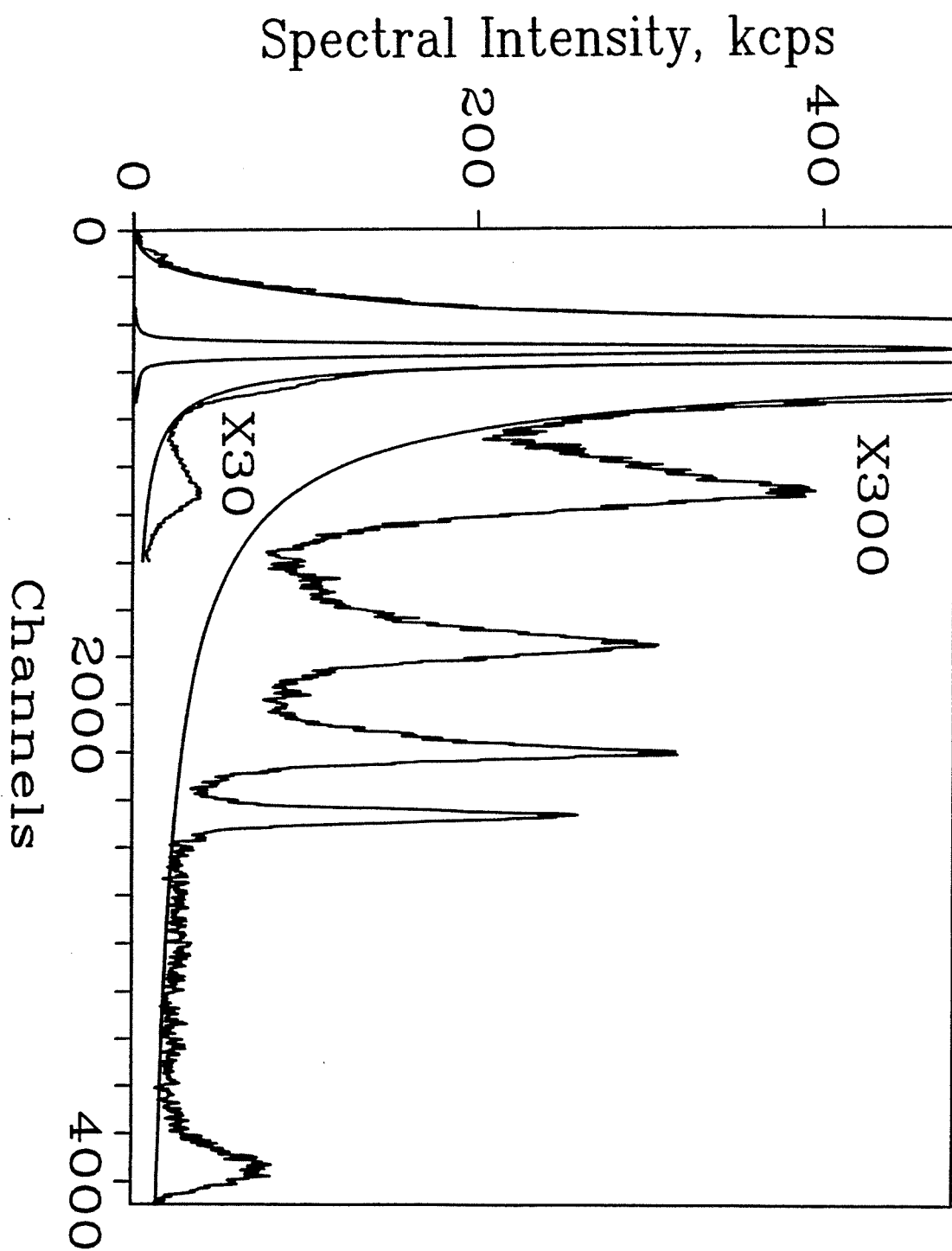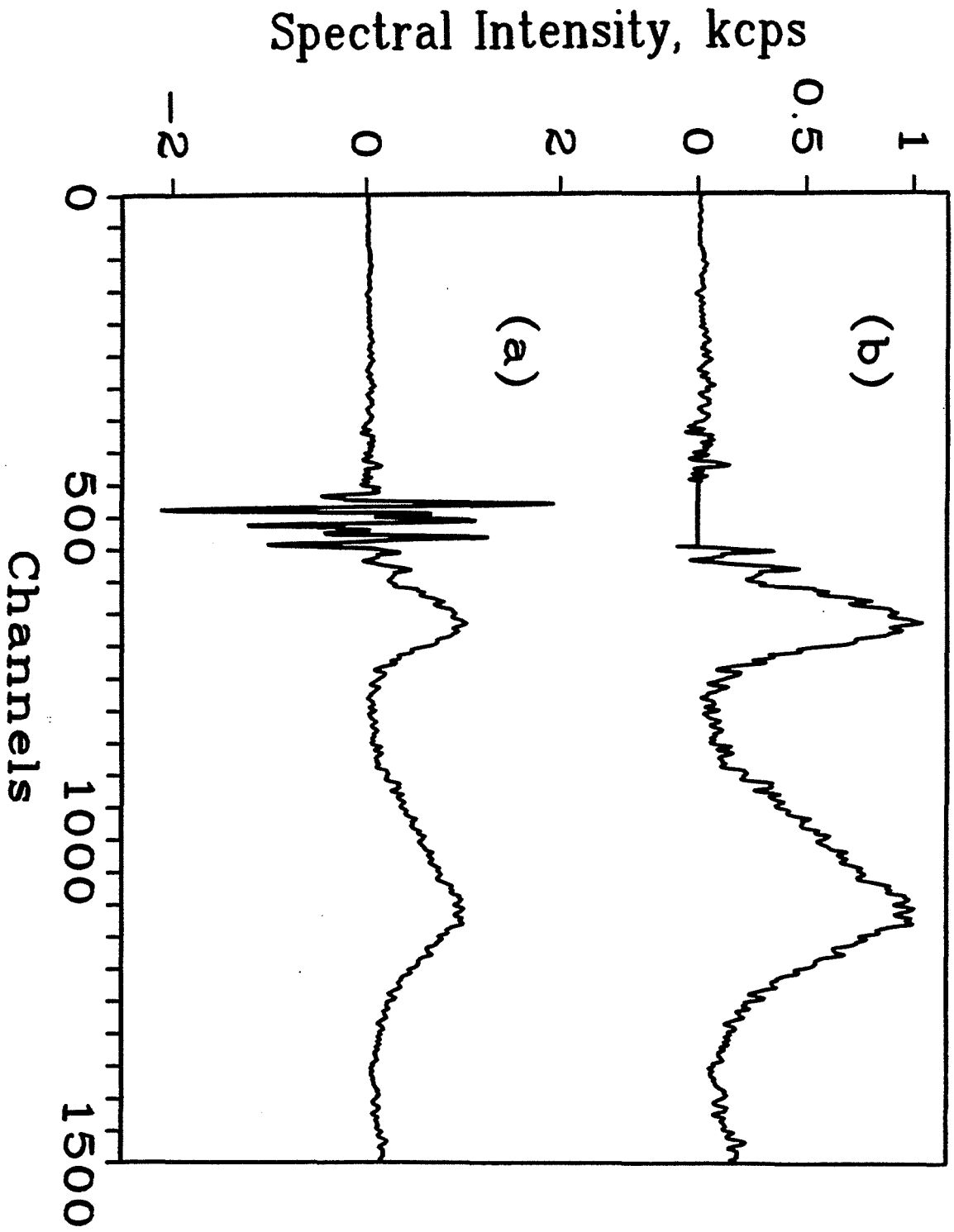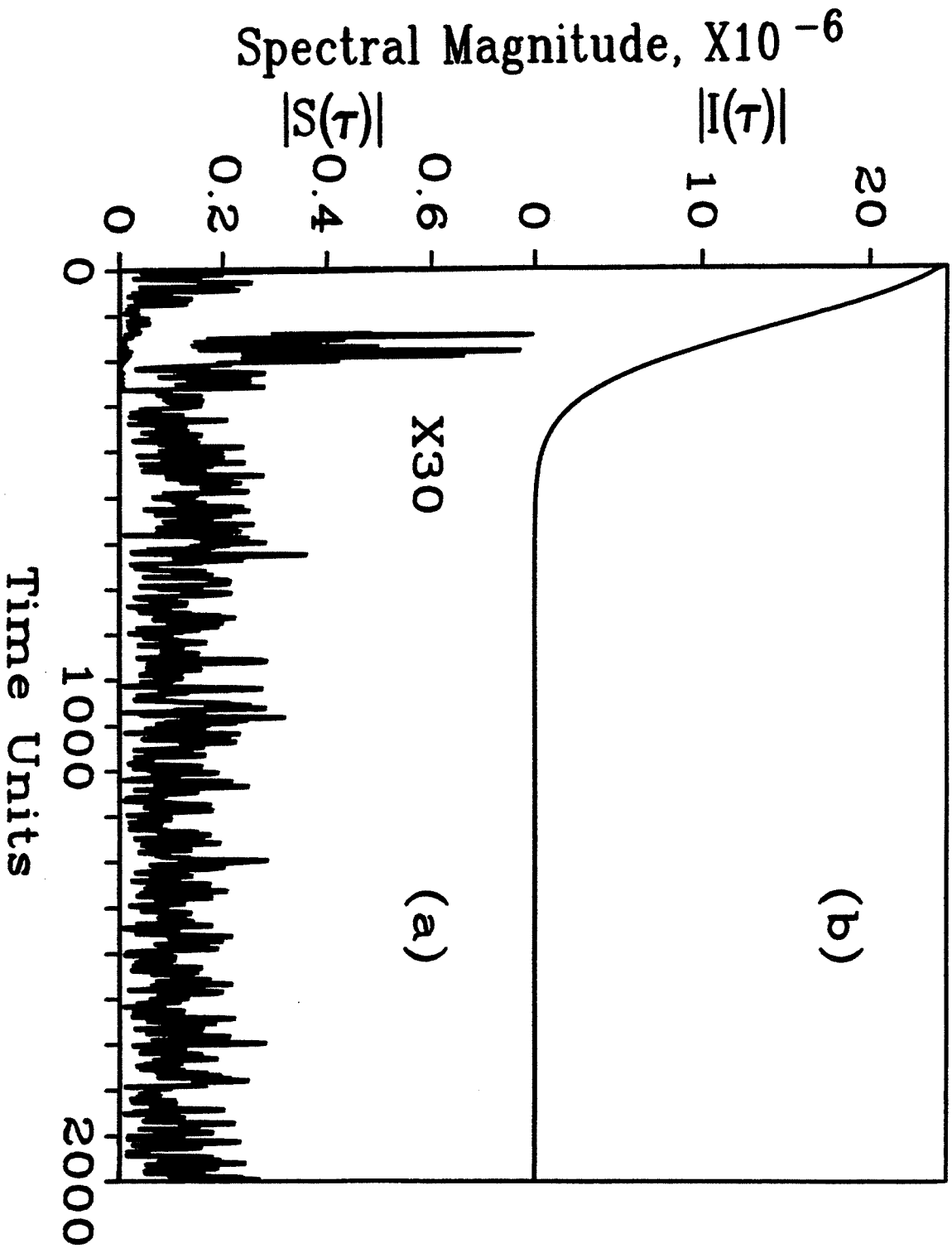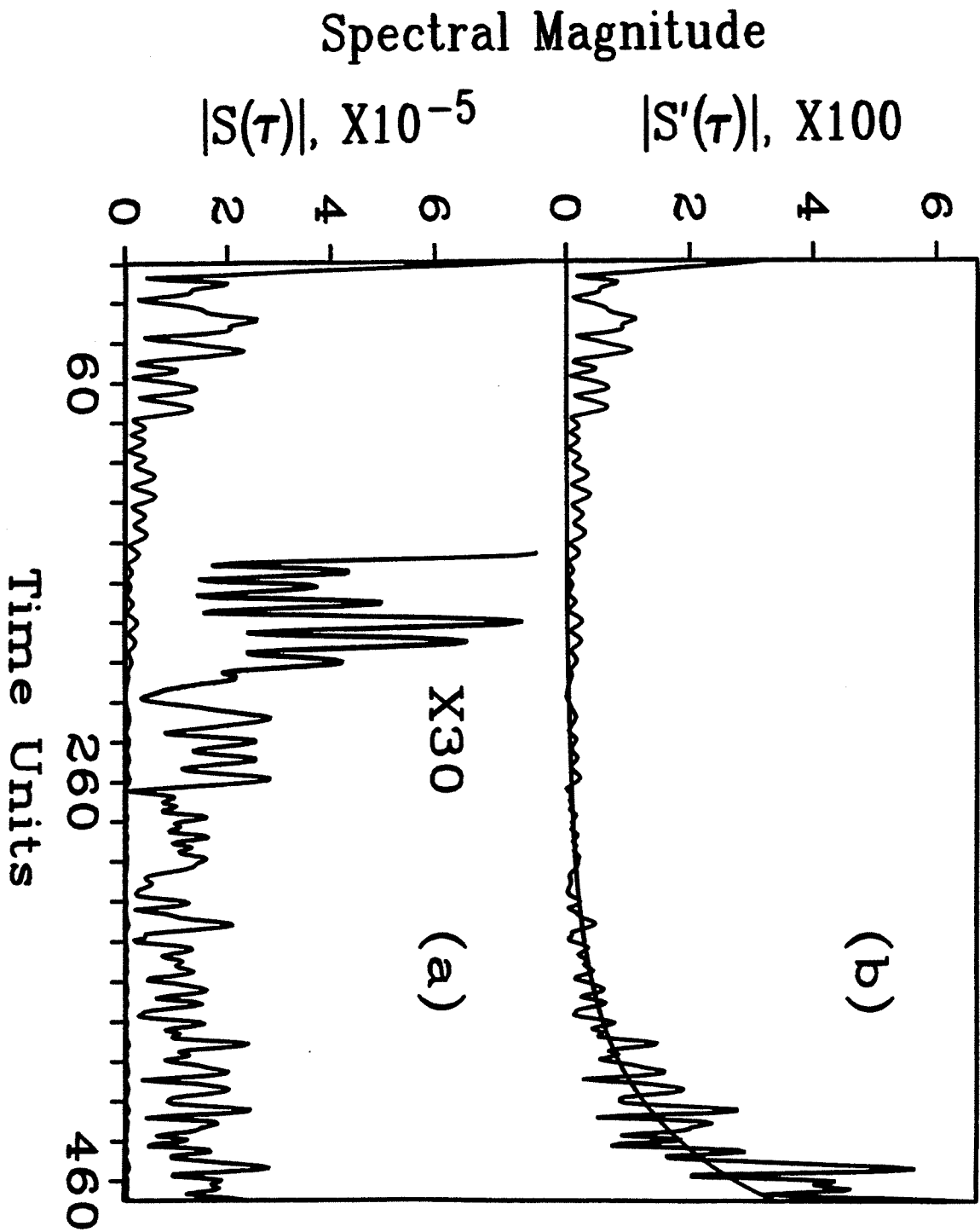
Fig. 1

34

Fig. 2

Fig. 3

36

Fig. 4

37

Fig. 5

Spectral Magnitude, X1000

$|S'(\tau)|$ $|C_{Model}(\tau)|$ $|C_{Model}(\tau)|$

(a)   (b)   (c)

Time Units

RMS$/|I(\tau)|$

Fig. 6

39

Fig. 7

40

SURFACE SCIENCE LETTERS

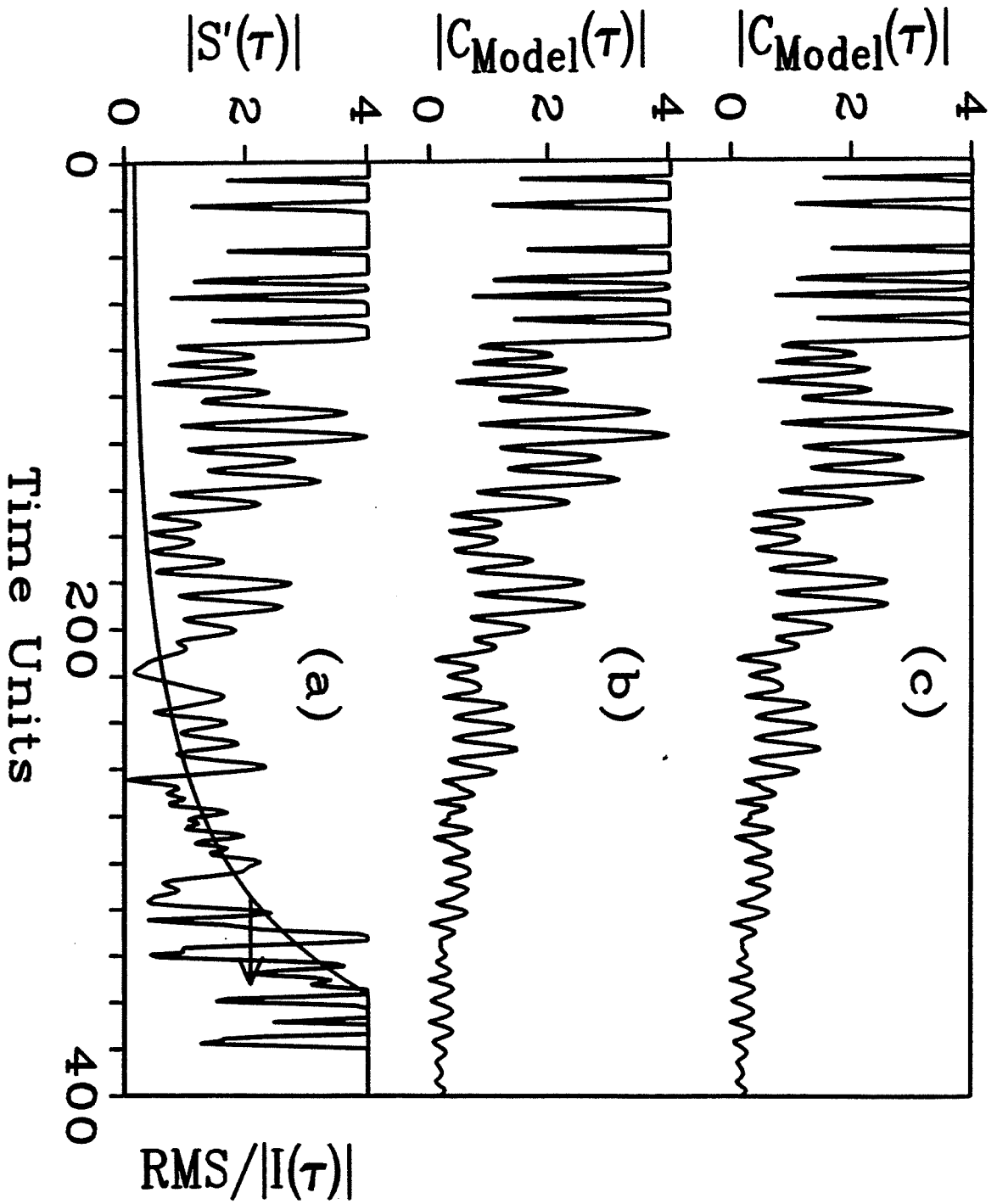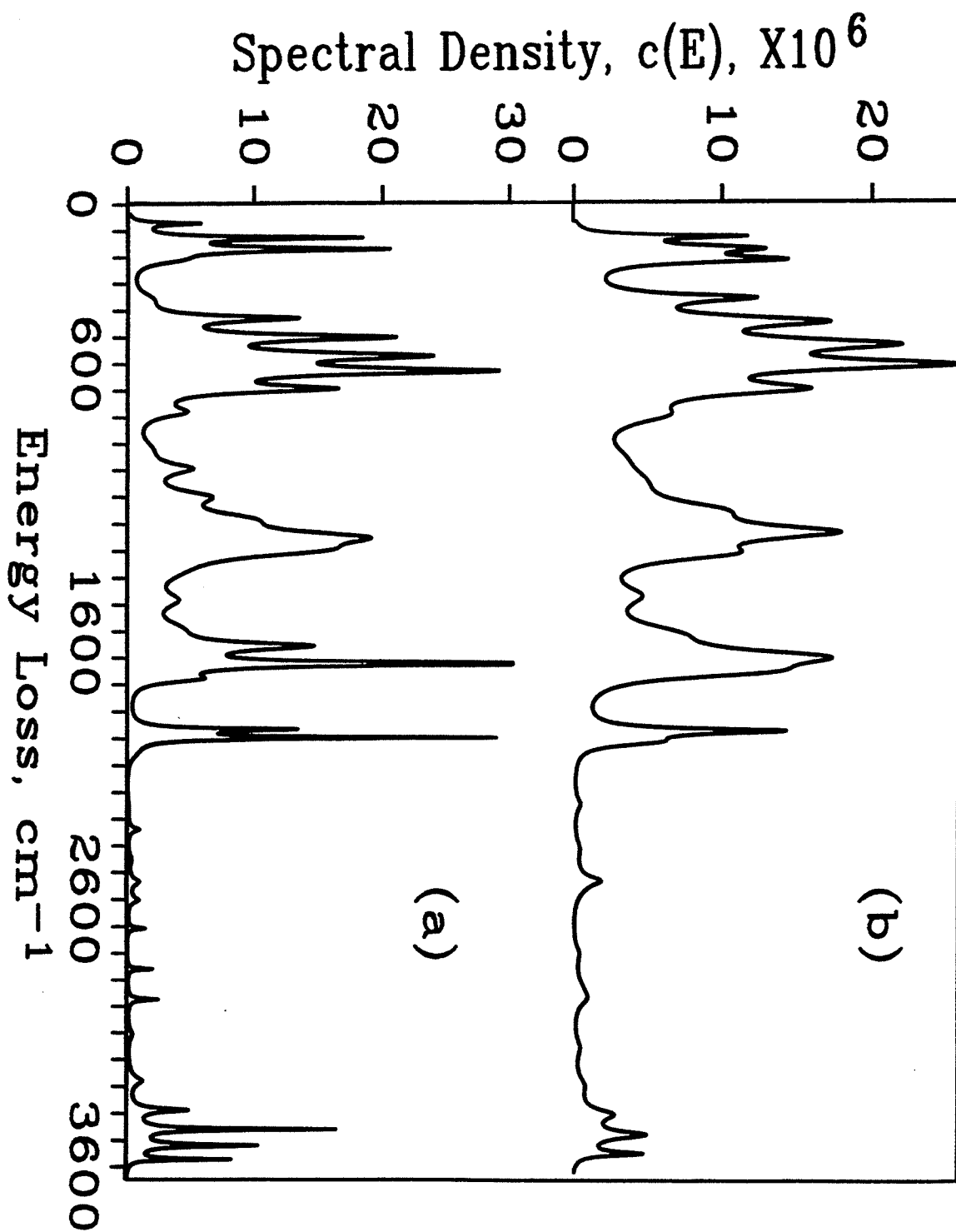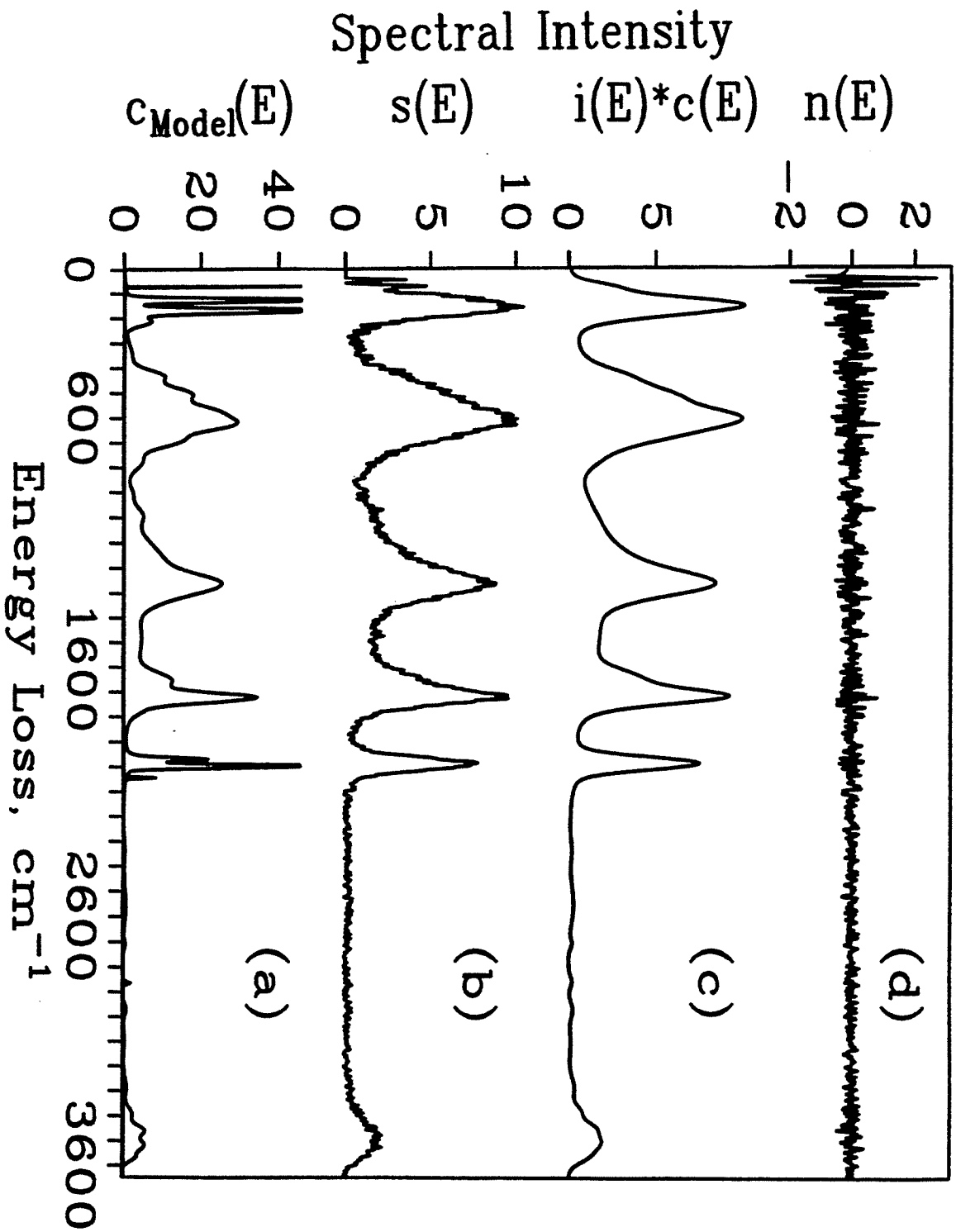## Surface Science Letters

The identification of $\mu_3-\eta^2$-coordinated CN from the dehydrogenation of methylamine on the Ru(001) surface

W.H. Weinberg, D.F. Johnson, Y.-Q. Wang

Department of Chemical Engineering, University of California, Santa Barbara, CA 93106, USA

J.E. Parmeter [1] and M.M. Hills [2]

Division of Chemistry and Chemical Engineering, California Institute of Technology, Pasadena, CA 91125, USA

Results of thermal desorption mass spectrometry and high-resolution electron energy loss spectroscopy (HREELS) indicate that the dehydrogenation of monomethylamine (CH_3NH_2) on the clean Ru(001) surface produces side-on bonded cyanide (CN) that engages in $\mu_3 - \eta^2$ coordination with the threefold site of the hexagonally closed packed surface, resulting in a bond order of two for the CN adsorbate.

Careful characterization of the bonding interactions of CN adsorbates with single crystalline surfaces is important for several reasons, of which three are delineated here. First, as an electrolyte in solution, the cyanide anion is observed to chemisorb on the surfaces of noble metal electrodes and to participate in oxidation/reduction reactions during cyclic voltammetry experiments [1–3]. Second the adsorption of cyanogen (C_2N_2) on single-crystalline surfaces has led to speculation that a two-dimensional surface polymer analogous to paracyanogen is responsible for the characteristic "β_1" and "β_2" C_2N_2 thermal desorption and semi-ordered LEED features observed for some platinum-group metals (vide infra). Third, and most important, a fundamental understanding of the selective activation of C–H, N–H and C–N bonds by transition metal surfaces must have as its foundation the results of careful decomposition studies of simple molecules containing these bonds.

The formation of CN on single crystalline surfaces has been observed from the decomposition of C_2N_2 on Pt(111) [4,5], Pt(110) [6,7], Pt(100) [8–10], Ag(110) [7], Cu(110) and oxygen-precovered Cu(110) [11], Cu(111) and oxygen-precovered Cu(111) [12], Rh(111) and oxygen-precovered Rh(111) [13], Ru(100) [14], Ni(111) [15], Pd(111) [16–18] and Pd(100) [17,19]; and from the dehydrogenation of CH_3NH_2 on Pt(111) [20] and Ni(111) [21]. There is tentative evidence that the adsorbed CN coordinates through both the carbon and nitrogen on a number of these clean surfaces. X-ray photoelectron spectroscopic (XPS) studies of C_2N_2 on Ru(100) show that upon annealing above 250 K, the N(1s) level shifts from 401.3 to 397.6 eV, indicative of a strong interaction between the nitrogen atom and the surface. Similarly, the absence of either an UV-photoemission feature or an electronic transition in EELS in the region near 5 eV, which is characteristic of metal–ligand charge transfer in terminally-coordinated platinum cyanide complexes [22], has led Wille et al. [8] and Conrad et al. [9], in independent studies of C_2N_2 on Pt(100), to conclude that adsorbed CN must involve significant interaction of the nitrogen atom with the surface.

[1] Current address: Chemistry Department, Texas A&M University, College Station, TX 77843-3255, USA.
[2] Current address: Aerospace Corp., P.O. Box 92957, Los Angeles, CA 90009, USA.

Other than the study reported here, the only other HREELS experiments conducted with CN on single crystalline surfaces are for Pd(111) and Pd(100) [17], and Cu(111) and oxygen-precovered Cu(111) [23]. Both Pd(111) and Pd(100) yield the same HREELS loss features associated with CN: 280 cm^{-1} for ν(Pd–CN) and 1895 cm^{-1} for ν(CN) stretching modes. The CN was interpreted by these authors as lying parallel to the surface with a $\sigma + \pi$ bonding interaction arising from metal to 5σ donation with some 1π to metal donation, partially counterbalancing the metal to adsorbate charge transfer. A near edge X-ray absorption fine structure (NEXAFS) study of CN on Pd(111) [18] suggested that the CN bond axis is tilted 14° above the plane of the surface. The authors prefer a parallel bonding orientation and state that "some other source of error associated with the NEXAFS experiment itself is responsible for the small deviation". The HREELS loss features of the ν(CN) stretching mode on Cu(111) and oxygen-precovered Cu(111) are at 2045 and 2140 cm^{-1}, respectively [23]. The authors interpret these results as the CN being oriented in a parallel $\sigma + \pi$ bonding configuration on the clean surface, but that in the presence of oxygen it reorientates to a terminal coordination through the carbon atom. This reorientation is purportedly driven by a competition for the available charge that the copper surface is able to transfer and an assumption that the 5σ orbital of CN is better able to withdraw electron density when directed at a copper surface atom. In our view, this interpretation for cyanide adsorbed on Cu(111) and oxygen-precovered Cu(111) is not credible. We believe that on both surfaces the cyanide adsorbs terminally via lone-pair donation to the metal surface from the 5σ orbital of the carbon atom. The ν(CN) stretching mode is at a higher frequency in the presence of the oxygen overlayer because the more highly electronegative oxygen adatoms withdraw electron density from the copper surface, thereby reducing the amount of charge which would otherwise be backdonated into the antibonding π^* orbitals of CN. The blue-shift of 95 cm^{-1} for the oxygen-precovered Cu(111) versus the clean Cu(111) surface is understood easily in light of these simple principles.

There are several organometallic complexes that exhibit $\sigma + \pi$ bonding interactions for bridging ligands containing CN triple bonds. Acetonitrile, CH$_3$CN, coordinates in a μ_3–η^2 fashion to the threefold site of Fe$_3$(CH$_3$CN)(CO)$_9$ with ν(CN) = 1610 cm^{-1} [24]. The p-tolylisonitrile ligand bridges the dimanganese complex (μ-p-CH$_3$C$_6$H$_5$NC)-Mn$_2$(dppm)$_2$(CO)$_4$, in a μ_2–η^2 fashion with ν(CN) = 1661 cm^{-1} [25a,25b]. Three isonitriles coordinate in a similar manner in the di-molybdenum complex Cp$_2$Mo$_2$(CO)$_4$(μ_2–η^2-CNR) with ν(CN) = 1725 cm^{-1} for R = CH$_3$, 1666 cm^{-1} for R = phenyl, and 1690 cm^{-1} for R = t-butyl [26]. In Ni$_4$[CNC(CH$_3$)$_3$]$_7$, bridging isonitriles coordinate either across the edges or the faces of the tetrahedron generated by the four nickel atoms, yielding values of ν(CN) between 1605 and 1610 cm^{-1} [27].

Within organometallic clusters, bridging CN ligands are most often found to be di-σ bonded in a linear fashion between two metal atoms [28a–28c]. The corresponding values of ν(CN) range from approximately 2000 to 2150 cm^{-1}, indicating that the CN triple bond is retained. One exception, however, is the μ_2–η^2-CN ligand observed in the cationic di-rhodium complex [Rh$_2$(μ_2–CN)(μ–CO)(CO)$_2$(μ–dppm)$_2$]$^+$ in which ν(CN) = 2044 cm^{-1}, and X-ray crystallographic measurements show the CN to be inclined 55° above the plane containing the rhodium atoms and dppm ligands [29]. For comparison to these ν(CN) stretching frequencies, those of CH$_3$NC and methylene imine, H$_2$CNH, are 2166 and 1638 cm^{-1}, respectively [30,31].

Thermal desorption and HREELS experiments for the decomposition of CH$_3$NH$_2$ and its deuterated isotopes CH$_3$ND$_2$ and CD$_2$ND$_2$ [32] were conducted in two ultrahigh vacuum systems described elsewhere [33a,33b]. A combination of thermal desorption and Auger spectra shows that the decomposition products arising from a saturation coverage of CH$_3$NH$_2$ adsorbed on Ru(001) at 80 K are H$_2$, N$_2$, NH$_3$ and surface carbon. In particular, neither HCN nor C$_2$N$_2$ are observed. The HREELS measurements indicate that below 270 K molecular CH$_3$NH$_2$ adsorbs via electron lone pair donation from the nitrogen atom. The isolation and identification of adsorbed CH$_2$NH$_2$
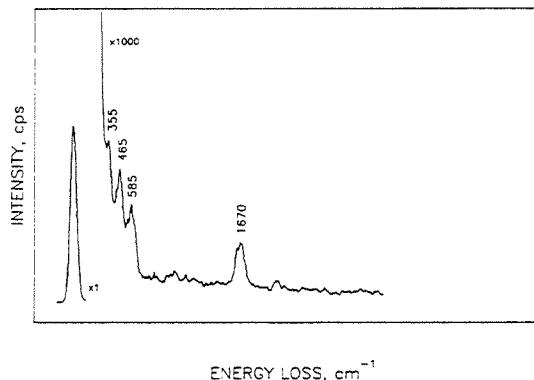
42

ENERGY LOSS, cm^{-1}

Fig. 1. High-resolution electron energy loss spectrum after adsorption of methylamine on the Ru(001) surface at 80 K, followed by annealing to 425 K. The modes at 1670, 465 and 355 cm^{-1} are due to ν(CN), ν_a(Ru–CN) and ν_s(Ru–CN) of adsorbed cyanide; and the peak at 585 cm^{-1} is due to the overlapping ν(RuC) and ν(RuN) modes.

and CHNH$_2$ are achieved after annealing to approximately 290 and 320 K, respectively. Competing reaction pathways open between 330 and 360 K leading to the formation of both NH$_3$ and further dehydrogenated adsorbates retaining C–N bonds. Thermal desorption measurements indicate that essentially all of the hydrogen-containing reaction products — H$_2$ and NH$_3$ — have desorbed by 425 K.

All three isotopes of methylamine produce identical EELS spectra after annealing to 425 K, and that of CH$_3$NH$_2$ is shown in fig. 1. There are four peaks observed at 355, 465, 585 and 1670 cm^{-1}. The 585 cm^{-1} peak increases in intensity after annealing to 500–550 K, and by 600 K, it is the only feature remaining. Between 800 and 1000 K, where recombinative desorption occurs, its intensity decreases but does not disappear entirely; hence, it is assigned to the overlapping ν(Ru–N) and ν(Ru–C) stretching modes. The remaining three peaks can only be attributed to a side-on bonded CN species. The 1670 cm^{-1} peak is assigned to the ν(CN) stretching mode, and the 355 and 465 cm^{-1} peaks are the symmetric and asymmetric ν(Ru–CN) stretching modes. Note that the CN bond is cleaved irreversibly on the Ru(001) surface at temperatures between 500 and 600 K.

The frequency of the CN stretching mode at 1670 cm^{-1} is typical of a CN adspecies with a bond order of two. Based on the observed value of ν(CN), X-ray crystallographic measurements of analogous organometallic complexes, and the electron-donating nature of the CN adsorbate, we think it is most plausible to describe the bonding as a $\sigma + 2\pi$ interaction resulting from $\mu_3-\eta^2$ coordination of CN in a threefold surface site. In this picture, the carbon atom is σ-bonded to one ruthenium atom with the CN bond axis inclined across the center of the site. In this manner, the valence d-orbitals of the surface ruthenium atoms can overlap with both of the π systems of the CN triple bond, thereby allowing donation from the π systems and/or backdonation from the ruthenium surface atoms to the π^* antibonding orbitals.

In summary, we have characterized the side-on bonded CN adsorbate on Ru(001) which stands in sharp contrast to similar species on clean Pd(111) and Pd(100) surfaces. At first glance it might be thought that the bonding and catalytic behavior would be nearly the same in each case since each CN is described by similar $\sigma + \pi$ interactions. However, unlike the other surfaces where the CN adspecies is believed to exist as CN$^{\delta-}$ with δ approaching unity, strong electron donation to the ruthenium surface from the π systems of the CN adsorbate reduce significantly its bond order from three to two. This interaction and the concomitant d–π rehybridization explains the observed propensity of ruthenium surfaces toward activating the cleavage of the formidable CN triple bond.

References

[1] R.E. Benner, K.U. von Raben, R. Dornhaus, R.K. Chang, B.L. Laube and F.A. Otter, Surf. Sci. 102 (1981) 7.
[2] R.E. Benner, R. Dornhaus, R.K. Chang and B.L. Laube, Surf. Sci. 101 (1980) 341.
[3] K. Kunimatsu, H. Seki, W.G. Golden, J.G. Gordon II and M.R. Philpott, Surf. Sci. 158 (1985) 596.

[4] J.R. Kingsley, D. Dahlgren and J.C. Hemminger, Surf. Sci. 139 (1984) 417.

[5] W. Hoffmann, E. Bertel and F.P. Netzer, J. Catal. 60 (1979) 316.

[6] M.E. Bridge and R.M. Lambert, Surf. Sci. 63 (1977) 315.

[7] M.E. Bridge, R.A. Marbrow and R.M. Lambert, Surf. Sci. 57 (1976) 415.

[8] R.A. Wille, F.P. Netzer and J.A.D. Matthews, Surf. Sci. 68 (1977) 259.

[9] H. Conrad, J. Küppers, F. Nitschke and F.P. Netzer, Chem. Phys. Lett. 46 (1977) 571.

[10] F.P. Netzer, Surf. Sci. 61 (1976) 343.

[11] D.A. Outka, S.W. Jorgensen, C.M. Friend and R.J. Madix, J. Mol. Catal. 21 (1983) 375.

[12] F. Solymosi and J. Kiss, Surf. Sci. 108 (1981) 368.

[13] F. Solymosi and L. Bugyi, Surf. Sci. 147 (1984) 685.

[14] N.J. Gudde and R.M. Lambert, Surf. Sci. 124 (1983) 372.

[15] J.C. Hemminger, E.L. Muetterties and G.A. Somorjai, J. Am. Chem. Soc. 101 (1979) 62.

[16] M.E. Kordesch, W. Stenzel and H. Conrad, J. Electron. Spectrosc. Relat. Phenom. 39 (1986) 89.

[17] M.E. Kordesch, W. Stenzel and H. Conrad, Surf. Sci. 186 (1987) 601.

[18] J. Somers, M.E. Kordesch, Th. Linder, H. Conrad, A.M. Bradshaw and G.P. Williams, Surf. Sci. 188 (1987) L693.

[19] K. Besenthal, G. Chiarello, M.E. Kordesch and H. Conrad, Surf. Sci. 178 (1986) 667.

[20] S.Y. Hwang, E.G. Seebauer and L.D. Schmidt, Surf. Sci. 188 (1987) 219.

[21] I. Chorkendorff, J.N. Russell, Jr. and J.T. Yates, Jr., J. Chem. Phys. 86 (1987) 4692.

[22] J.J. Alexander and H.B. Gray, J. Am. Chem. Soc. 90 (1968) 4260.

[23] M.E. Kordesch, W. Stenzel, H. Conrad and M.J. Weaver, J. Am. Chem. Soc. 109 (1987) 1878.

[24] M.A. Andrews and H.D. Kaesz, J. Am. Chem. Soc. 101 (1979) 7255.

[25] (a) A.L. Balch and L.S. Benner, J. Organomet. Chem. 135 (1977) 339;
(b) L.S. Benner, M.M. Olmstead and A.L. Balch, J. Organomet. Chem. 159 (1978) 289.

[26] R.D. Adams, D.A. Katahira and L.-W. Yang, Organometallics 1 (1982) 231.

[27] V.W. Day, R.O. Day, J.S. Kristoff, F.J. Hirsekorn and E.L. Muetterties, J. Am. Chem. Soc. 97 (1975) 2571.

[28] (a) G.A. Carriedo, M.C. Crespo, V. Riera, M.L. Valin, D. Moreiras and X. Solans, Inorg. Chim. Acta 121 (1986) 191;
(b) H.M. Dawes, M.B. Hursthouse, A.A. del Paggio, E.L. Muetterties and A.W. Parkins, Polyhedron 4 (1985) 379;
(c) J.K. Ruff, Inorg. Chem. 8 (1969) 86.

[29] S.P. Deraniyagala and K.P. Grundy, Inorg. Chim. Acta 84 (1984) 205.

[30] Y. Hase and O. Sala, An. Acad. Bras. Cienc. 45 (1973) 381.

[31] Y. Hamada, K. Hasiguchi and M. Tsuboi, J. Mol. Spectrosc. 105 (1984) 70.

[32] D.F. Johnson, J.E. Parmeter, M.M. Hills, Y.-Q. Wang and W.H. Weinberg, in preparation.

[33] (a) E.D. Williams and W.H. Weinberg, Surf. Sci. 82 (1979) 93;
(b) G.E. Thomas and W.H. Weinberg, Rev. Sci. Instrum. 50 (1979) 497.

44

Interaction of Ammonia with Chemically Modified Ru(001) Surfaces

Y.-K. Sun,[†] Y.-Q. Wang, C. B. Mullins,[‡] and W. H. Weinberg*

*Department of Chemical Engineering, University of California, Santa Barbara,
Santa Barbara, California 93106*

The interaction of ammonia with the Ru(001)–($\sqrt{3}\times\sqrt{3}$)$R30°$–N, Ru(001)–p(2×2)–O, and Ru(001)–p(1×2)–O surfaces has been investigated by using thermal desorption mass spectrometry and low-energy electron diffraction and compared with the interaction of ammonia with the initially clean Ru(001) surface. Ammonia adsorbs and desorbs reversibly on all four surfaces with no detectable decomposition. The ammonia–surface binding energy is increased on the nitrogen-modified surface relative to the clean Ru-(001) surface, and the binding energy is further increased on the oxygen-modified surfaces. On the Ru-(001)–($\sqrt{3}\times\sqrt{3}$)$R30°$–N surface at a temperature of 245 K, with a fractional coverage of ammonia of approximately 0.1, the ($\sqrt{3}\times\sqrt{3}$)$R30°$–N low-energy electron diffraction (LEED) pattern transforms into a (2×2) LEED pattern. Following ammonia desorption the ($\sqrt{3}\times\sqrt{3}$)$R30°$–N superstructure can be retrieved by annealing the surface. Ammonia forms an ordered p(2×2) overlayer on the clean surface. No ordered overlayers due to the presence of ammonia are observed, however, on any of the chemically modified surfaces.

1. Introduction

The interaction of ammonia with clean and chemically modified Ru(001) surfaces has been the focus of several previous investigations.[1-7] This subject is of considerable interest because it relates to one of the more important industrial catalytic processes, ammonia synthesis, and because results from recent studies of a supported potassium-promoted ruthenium catalyst have found it to be a better ammonia synthesis catalyst than the doubly promoted iron catalyst.[8-11] From a fundamental point of view, there is interest in the interaction of ammonia with clean and chemically modified transition-metal surfaces because ammonia is a prototypical example of a weak donor ligand that bonds to metal atoms both in organometallic compounds and on surfaces via donation of electron density from the lone pair to the empty density of states of the metal. We report here the results of an experimental investigation of the interaction of ammonia with the Ru-(001)–($\sqrt{3}\times\sqrt{3}$)$R30°$–N, Ru(001)–p(2×2)–O, and Ru-(001)–p(1×2)–O surfaces employing low-energy electron diffraction (LEED) and thermal desorption mass spectrometry (TDMS).

It is instructive to review previous studies of the interaction of ammonia with *clean* Ru(001) prior to any discussion regarding ammonia chemisorption on chemically modified Ru(001) surfaces. Danielson et al. studied

ammonia adsorption, decomposition, and desorption on Ru(001) using TDMS, Auger electron spectroscopy, and LEED and concluded that for adsorption temperatures less than 300 K the adsorbed ammonia desorbed completely reversibly, with negligible dissociation occurring during annealing of the sample.[1,2] Significant dissociation could be induced by electron bombardment of the adsorbed ammonia or by exposing the surface to large fluences of ammonia with the surface temperature greater than 300 K. Benndorf and Madey employed LEED, TDMS, electron stimulated desorption ion angular distribution (ESDIAD) measurements, and work function ($\Delta\phi$) measurements in their study of the clean surface, and they also concluded that for low adsorption temperatures (~80 K) ammonia adsorption is completely reversible.[3] They showed that a large ammonia exposure at 80 K leads to ammonia desorption over a broad temperature range, with monolayer desorption between approximately 150 and 350 K, desorption of second-layer ammonia at 140 K, and multilayer desorption in a sharp peak at 115 K. Both ESDIAD and $\Delta\phi$ measurements support an assignment for monolayer bonding via the lone pair of electrons on the nitrogen atom. Benndorf and Madey also estimated the saturation monolayer coverage to be 0.25 monolayer (or 3.9×10^{14} molecules cm^{-2}) and suggested that ammonia adsorbs in 3-fold hollow sites on this surface.[3] Tsai and Weinberg investigated the catalytic decomposition of ammonia on Ru(001) between pressures of 1×10^{-6} and 2×10^{-6} Torr with surface temperatures, T_S, ranging from 500 to 1250 K.[4] For T_S approximately equal to 750 K or greater, they found that the steady-state decomposition kinetics were controlled by a competition between ammonia desorption and a surface reaction involving the cleavage of an N–H bond. The rate of decomposition in this regime is first order in ammonia pressure and exhibits a primary kinetic isotope effect with an apparent activation energy of 5.0 ± 0.3 kcal/mol. At lower temperatures, the steady-state decomposition kinetics are controlled by the rate of recombinative desorption of nitrogen adatoms, and the decomposition rate is independent of ammonia pressure. The apparent activation energy in this regime is equal to the measured activation energy for the desorption of nitrogen, namely

† Present address: Department of Chemistry BG-10, University of Washington, Seattle, WA 98195.
‡ Present address: IBM Almaden Research Center, San Jose, CA 95120-6099.
(1) Danielson, L. R.; Dresser, M. J.; Donaldson, E. E.; Dickinson, J. T. *Surf. Sci.* **1978,** *71,* 599.
(2) Danielson, L. R.; Dresser, M. J.; Donaldson, E. E.; Sandstrom, D. R. *Surf. Sci.* **1978,** *71,* 615.
(3) Benndorf, C.; Madey, T. E. *Surf. Sci.* **1983,** *135,* 164.
(4) Tsai, W.; Weinberg, W. H. *J. Phys. Chem.* **1987,** *91,* 5302.
(5) Parmeter, J. E.; Wang, Y.; Mullins, C. B.; Weinberg, W. H. *J. Chem. Phys.* **1988,** *88,* 5225.
(6) Benndorf, C.; Madey, T. E. *Chem. Phys. Lett.* **1983,** *101,* 59.
(7) Zhou, Y.; Akhter, S.; White, J. M. *Surf. Sci.* **1988,** *202,* 357.
(8) Ozaki, A.; Aika, K.; Hori, H. *Bull. Chem. Soc. Jpn.* **1971,** *44,* 3216.
(9) Uchiyama, S.; Hattori, Y.; Ozaki, A.; Aika, K. *Chem. Lett.* **1981,** 1463.
(10) Aika, K. *Angew. Chem., Int. Ed. Engl.* **1986,** *25,* 558.
(11) Bond, G. C. In *The Physical Basis for Heterogeneous Catalysis;* Drauglis, E., Jaffee, R. I., Eds.; Plenum: New York, 1975; p 53.

43 ± 3 kcal/mol. Parmeter et al. studied the interaction of ammonia with Ru(001) employing high-resolution electron energy loss spectroscopy (HREELS), and their results were in substantial agreement with the results of earlier investigations.[5] They also showed that the symmetric deformation mode of ammonia on Ru(001) shifts down nearly linearly with increasing coverage, from 1160 cm^{-1} in the low coverage limit to 1070 cm^{-1} at a saturated monolayer, and that this shift could be correlated with the large decrease in the work function upon ammonia adsorption. Parmeter et al. concluded that both their HREELS results and the organometallic literature concerning NH$_3$ ligands are more consistent with ammonia adsorption at an on-top site.

The catalytic properties of clean transition-metal surfaces can be altered significantly by the presence of both electropositive[12] and electronegative[13] adsorbates, including sulfur,[13] oxygen,[14,15] phosphorus,[16] and nitrogen.[17-19] Studies of the effects of these adsorbates on the chemisorption, reaction, and desorption of molecules from metal surfaces are useful in elucidating the effects of promoters and poisons on industrial catalysts. In a particularly relevant investigation to the work we report here, Benndorf and Madey employed ESDIAD, TDMS, and LEED to investigate the effect of preadsorbed oxygen and sodium on the interaction of ammonia with Ru(001), concentrating on low, fractional-monolayer coverages of ammonia in order to minimize the effects of lateral interactions between adsorbed ammonia molecules.[6] Their results indicate that the coadsorption of ammonia with oxygen leads to an increase in the ammonia binding energy, while coadsorption with sodium leads to a decrease. The work we report here concerning the interaction of ammonia with nitrogen- and oxygen-modified Ru(001) surfaces confirms and extends the earlier work of Benndorf and Madey.[6]

2. Experimental Details

The experiments were carried out in an ion-pumped (200 L/s) stainless steel, ultrahigh vacuum (UHV) chamber equipped with quadrupole mass spectrometry, Auger electron spectroscopy, and low-energy electron diffraction.[20] The base pressure of the bell jar was below 1 × 10^{-10} Torr. The Ru(001) crystal was mounted on a manipulator by two 0.010-in. tantalum wires that were spotwelded to the back of the crystal, which can be heated resistively, and cooled conductively by liquid nitrogen. The temperature of the Ru(001) surface was measured by a 0.003-in. W/5% Re–W/26% Re thermocouple that was also spotwelded to the back of the crystal. Oxygen cleaning was effected by cycling the temperature of the crystal between 400 and 1100 K in 7 × 10^{-8} Torr of oxygen, backfilled into the bell jar. Chemisorbed oxygen was removed by annealing the crystal to over 1600 K. The cleanliness of the surface was verified by Auger electron spectroscopy.

Ammonia, obtained from Matheson (99.99%), was introduced into the UHV chamber through a directional beam doser, which effectively reduced the amount of NH$_3$ that must be leaked into the UHV system to achieve a particular exposure, as compared to backfilling the bell jar. For example, with the manipulator cooled by liquid nitrogen, the increase in the background pressure was less than 2 × 10^{-11} Torr during dosing; i.e., the cold

(12) Bonzel, H. P. *Surf. Sci. Rep.* **1988**, *8*, 43, and references therein.
(13) Kiskinova, M. P. *Surf. Sci. Rep.* **1987**, *8*, 359, and references therein.
(14) Parmeter, J. E.; Schwalke, U.; Weinberg, W. H. *J. Am. Chem. Soc.* **1987**, *109*, 5083.
(15) Anton, A. B.; Avery, N. R.; Madey, T. E.; Weinberg, W. H. *J. Chem. Phys.* **1986**, *85*, 507.
(16) Kiskinova, M.; Goodman, D. W. *Surf. Sci.* **1981**, *108*, 64.
(17) Kiskinova, M.; Goodman, D. W. *Surf. Sci.* **1981**, *109*, L555.
(18) Tsai, W.; Weinberg, W. H. *J. Phys. Chem.* **1988**, *92*, 1245.
(19) Sun, Y.-K.; Weinberg, W. H. To be submitted for publication in *Surf. Sci.*
(20) Sun, Y.-K.; Chan, C.-Y.; Weinberg, W. H. *J. Vac. Sci. Technol., A* **1989**, *7*, 4298.

manipulator acted as an effective ammonia getter. The mass spectrometer was enclosed in a glass envelope which has an orifice with a diameter of 3 mm, in order to limit contributions to the thermal desorption spectra to the well-characterized front face of the crystal.[21] During measurements of the thermal desorption spectra, the Ru(001) surface was positioned 3 mm from the orifice. Enclosure of the mass spectrometer in the glass envelope also reduced the current of stray electrons from the mass spectrometer to the manipulator assembly, including the Ru(001) surface, to less than 5 nA during thermal desorption measurements. Without the glass envelope, the stray electron current was approximately 4 μA at a mass spectrometer emission current of 2 mA, which may cause electron-stimulated processes such as desorption or dissociation of the NH$_3$.[2]

The Ru(001)–p(1×2)–O surface was prepared by exposing the Ru(001) surface to 1.5 × 10^{-7} Torr of oxygen for 120 s (18 L) at 310 K, followed by annealing to 510 K.[22] The resulting surface had a sharp (2×2) LEED pattern[23] and an oxygen Auger intensity (defined as the ratio of peak-to-peak intensities of the oxygen KLL to ruthenium MNN transitions) of 0.060 (±0.004). The Ru(001)–p(2×2)–O surface was obtained by annealing the above surface to desorb 50% of the oxygen adatoms, as judged by a 50% reduction of the oxygen Auger intensity. The surface that resulted also had a sharp (2×2) LEED pattern. The fractional surface coverage of atomic oxygen on these surfaces is approximately one-half for the Ru(001)–p(1×2)–O surface and approximately one-fourth for the Ru(001)–p(2×2)–O surface. The Ru(001)–(√3×√3)R30°–N surface was prepared by decomposing ammonia thermally on the Ru(001) surface at an ammonia pressure of 2.8 × 10^{-6} Torr and a surface temperature of 480 K for 600 s, followed by a brief annealing to 520 K.[19] The fractional coverage of atomic nitrogen on this surface is approximately one-third. All heating rates employed in the thermal desorption experiments were 3 K s^{-1}. All LEED observations were made after cooling the crystal to below 150 K. Adsorption of ammonia from the background is negligible during the cooling due to the low ammonia-background pressure.

3. Results and Discussion

3.1. Ammonia on Clean Ru(001). Thermal desorption mass spectra of ammonia from clean Ru(001), following various exposures at 120 K, are shown in Figure 1. A clear (2×2) LEED pattern was observed following adsorption of ammonia to the same coverage as in curve d of Figure 1, with subsequent brief annealing to 150 K. Both the thermal desorption and the LEED results are in excellent agreement with those obtained previously by Benndorf and Madey.[3] The sharp peak centered at approximately 150 K is believed to correspond to desorption from a second layer of ammonia, on top of the first layer of chemisorbed ammonia, the latter of which has a fractional coverage of one-fourth at saturation.[3] Since the thermal desorption peaks due to the first layer and the second layer are not completely resolved, the ammonia overlayer obtained following adsorption at 120 K to the same coverage as in curve d of Figure 1, with subsequent brief annealing to 150 K, was taken as a monolayer. The absolute coverages of ammonia were then calculated by comparing the time-integrated area beneath each of the thermal desorption spectra to that of the monolayer. These absolute coverages are given in the caption of Figure 1. The broad thermal desorption spectrum corresponding to the saturated monolayer of ammonia, essentially curve b of Figure 1, is indicative of an (effectively) repulsive interaction among the ammonia admolecules on the surface. As would be expected,[18] a post-thermal-desorp-

(21) Feulner, P.; Menzel, D. *J. Vac. Sci. Technol.* **1980**, *17*, 662.
(22) Rahman, T. S.; Anton, A. B.; Avery, N. R.; Weinberg, W. H. *Phys. Rev. Lett.* **1983**, *51*, 1979.
(23) The three independent domains of (1×2) superstructure that are rotated by 120° with respect to one another give rise to an apparent (2×2) LEED pattern.
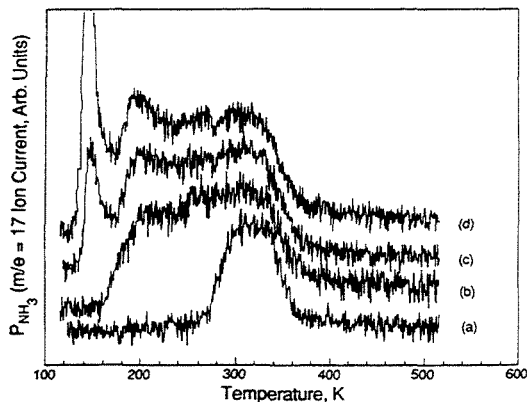
Figure 1. Thermal desorption spectra of ammonia on Ru(001) following increasing ammonia exposures from parts a to d at a surface temperature of 120 K. The heating rate is 3 K s^{-1}. The corresponding fractional coverages of NH_3 are (a) 0.11, (b) 0.24, (c) 0.28, and (d) 0.35. The low-temperature peak does not saturate with increasing exposure. The absolute coverage is calculated by comparison of the time-integrated area beneath each of the thermal desorption spectra (a to d) to that of the thermal desorption spectrum of a monolayer of ammonia on clean Ru(001), the fractional coverage of which is believed to be one-fourth.[3]

Figure 2. Thermal desorption spectra of ammonia on Ru(001)– $(\sqrt{3}\times\sqrt{3})R30°$–N at increasing ammonia exposures from parts a to f. The low-temperature peak does not saturate with increasing exposure. The heating rate is 3 K s^{-1}. The corresponding fractional coverages of ammonia are (a) 0.01, (b) 0.04, (c) 0.11, (d) 0.16, (e) 0.22, and (f) 0.42. The absolute coverage is determined in the same way as described in the caption of Figure 1; i.e., it is referenced to a saturation monolayer coverage of one-fourth on the clean surface.

tion analysis of the surface with Auger electron spectroscopy revealed a clean surface; no dissociation of ammonia was observed under these conditions.

3.2. Ammonia on Ru(001)–$(\sqrt{3}\times\sqrt{3})R30°$–N. The Ru(001)–$(\sqrt{3}\times\sqrt{3})R30°$–N surface, which has a fractional coverage of atomic nitrogen of one-third, was prepared by thermally decomposing ammonia on the Ru(001) surface at an ammonia pressure of 2.8×10^{-6} Torr and at a surface temperature of 480 K for 600 s, followed by brief annealing to 520 K.[19] A surface prepared in this way gives a sharp $(\sqrt{3}\times\sqrt{3})R30°$–N LEED pattern.

Thermal desorption spectra of ammonia following various exposures on the Ru(001)–$(\sqrt{3}\times\sqrt{3})R30°$–N surface at 120 K are shown in Figure 2. With increasing ammonia exposure, the high-temperature peak increases in area and shifts down in temperature. After saturation of the monolayer, a low-temperature peak is observed that does not saturate with increasing ammonia exposure. There is no distinct boundary in the thermal desorption spectra between the first layer and the multilayer of ammonia, similar to that which was observed on clean Ru(001); cf. Figure 1. Hence, the coverage of ammonia corresponding to the first layer cannot be determined completely unambiguously. The thermal desorption spectra of Figure 2 suggest, however, that the first layer saturates at a fractional coverage of approximately 0.16. The peak temperature corresponding to the first layer of ammonia is higher on the Ru(001)–$(\sqrt{3}\times\sqrt{3})R30°$–N surface than on the clean Ru(001) surface: at the same coverage of approximately 0.10 monolayer, it is 320 K on the clean Ru(001) surface and 355 K on Ru(001)–$(\sqrt{3}\times\sqrt{3})R30°$–N; cf. curve a in Figure 1 and curve c in Figure 2. This indicates an increase in the binding energy, by clean Ru-(001) surface: at the same coverage of approximately 0.10 monolayer, it is 320 K on the clean Ru(001) surface and 355 K on Ru(001)–$(\sqrt{3}\times\sqrt{3})R30°$–N; cf. curve a in Figure 1 and curve c in Figure 2. This indicates an increase in the binding energy, by approximately 2–3 kcal mol^{-1}, of ammonia to the nitrogen-modified Ru(001) surface.

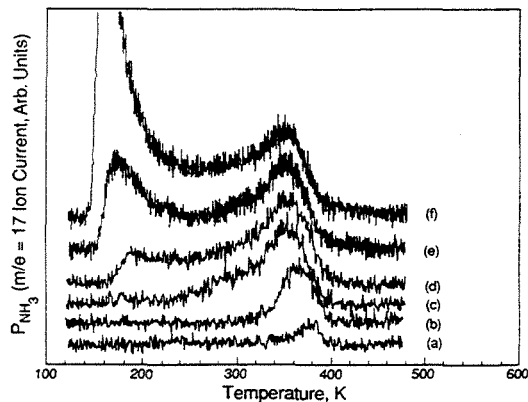The increase in the binding energy of ammonia to the Ru(001) surface in the presence of an electronegative

adsorbate such as atomic nitrogen can be explained in light of the bonding mechanism of ammonia to the surface. Ammonia chemisorbs on the surface via donation of the lone pair of electrons on the nitrogen atom to the unoccupied local density of electronic states of the metal, which results in a net transfer of charge to the surface and a decrease in the work function. The presence of electronegative atoms on the surface causes a reduction in the local density of occupied states near the Fermi level, which enhances the interaction between the ammonia and the surface.[24,25] Hence, the binding energy of ammonia on the nitrogen-modified Ru(001) surface is enhanced largely via an indirect, surface-mediated interaction, in addition to possible direct electrostatic interactions between the atomic nitrogen and the ammonia admolecules. At low coverages of ammonia, the binding energy on the nitrogen-modified surface is approximately 10–15% greater than that on the clean surface.

Although the Ru(001)–$(\sqrt{3}\times\sqrt{3})R30°$–N surface has a sharp LEED pattern, only a less intense (1×1) LEED pattern with a diffuse background was observed following the adsorption of ammonia at 120 K with an ammonia fractional surface coverage of 0.75. A "fuzzy" $(\sqrt{3}\times\sqrt{3})$–$R30°$–N LEED pattern was observed following the annealing of this surface to 150 K. This "fuzzy" $(\sqrt{3}\times\sqrt{3})$–$R30°$–N LEED pattern persisted up to 200 K. Further annealing to 245 K, however, resulted in the disappearance of this $(\sqrt{3}\times\sqrt{3})R30°$ LEED pattern and the appearance of a rather "fuzzy" (2×2) LEED pattern (which was most apparent at an electron beam energy of 53 eV). When the surface was then heated to 400 K to desorb all of the adsorbed ammonia (cf. Figure 2), the $(\sqrt{3}\times\sqrt{3})R30°$–N LEED pattern reappeared, but it was much more diffuse compared to that observed prior to the ammonia adsorption. The $(\sqrt{3}\times\sqrt{3})R30°$–N pattern, however, became as sharp as the pattern observed prior to the adsorption of ammonia when the surface was annealed further to 490 K. Note that all these annealing procedures resulted in no loss of nitrogen adatoms through recombinative desorption.[19]

(24) Feibelman, P. J.; Hamann, D. R. *Phys. Rev. Lett.* **1984,** *52,* 61.
(25) Feibelman, P. J.; Hamann, D. R. *Surf. Sci.* **1985,** *149,* 48.

In another experiment, the $(\sqrt{3}\times\sqrt{3})R30°$–N surface was exposed to ammonia at a surface temperature of 245 K. (The crystal was heated resistively while the manipulator was cooled by liquid nitrogen.) When equilibrium was established between the adsorption and desorption of ammonia, the surface was removed from the ammonia beam and cooled to below 150 K in less than 8 s. By use of this protocol, the fractional coverage of ammonia is estimated to be approximately 0.10; cf. Figure 2. The surface was then examined with LEED (using a low current density in the electron beam and an observation time of no more than 6 s in order to minimize electron-induced dissociation of ammonia). The diffuse (2×2) LEED pattern was observed in this case also. No $(\sqrt{3}\times\sqrt{3})$-$R30°$–N LEED pattern was observed at any beam voltage. Evidently, the presence of approximately 0.1 monolayer of NH_3 on the Ru(001)–$(\sqrt{3}\times\sqrt{3})R30°$–N surface at 245 K induces a transition from the well-ordered $(\sqrt{3}\times\sqrt{3})$-$R30°$ superstructure of the nitrogen adatoms to one that gives rise to a poorly ordered (2×2) LEED pattern. The latter is the ground state of the system, and the temperature of 245 K is required to overcome kinetic barriers to nitrogen-adatom hopping in the coadsorbed system. These barriers impose kinetic limits on the rate of the observed phase transition. It is interesting that, *after the ammonia has desorbed*, annealing to a higher temperature (490 K) is required for the (2×2) overlayer to transform back to the $(\sqrt{3}\times\sqrt{3})R30°$ superstructure, the latter of which is the ground state of the system, on a similar time scale as the original $(\sqrt{3}\times\sqrt{3})R30°$–N → (2×2) transformation *in the presence of ammonia*. The presence of ammonia lowers the barrier to nitrogen-adatom hopping. Although the detailed structure of the (2×2) overlayer is not known, two possible candidates are the following: (1) a p(2×2)–N overlayer with 8% of a monolayer of randomly adsorbed nitrogen adatoms; (2) a mixture of p(2×2)–N and p(1×2)–N phases with the former comprising approximately two-thirds of the surface and the latter comprising the remaining one-third.

3.3. Ammonia on Ru(001)–p(2×2)–O. Ammonia, due to the nature of its bonding to the surface (donation of a lone pair of electrons), increases its binding energy to the surface in the presence of electronegative nitrogen adatoms; cf. section 3.2. On this basis, one would expect qualitatively similar and quantitatively stronger effects on the binding energy of ammonia on oxygen-modified Ru(001) surfaces, since oxygen is more electronegative than nitrogen. Indeed, the peak temperature in the thermal desorption spectra of ammonia from Ru(001), at a fractional coverage of 0.05, was found to increase with increasing coverage of oxygen adatoms up to a fractional coverage of 0.5.[6] We have investigated the thermal desorption of ammonia from the Ru(001)–p(2×2) surface at various initial ammonia coverages. The thermal desorption spectra of ammonia following adsorption on the Ru-(001)–p(2×2) surface at 120 K are shown in Figure 3. It is obvious that the ordered oxygen overlayer strengthens the bonding of ammonia to the surface, and to a greater extent than does the nitrogen overlayer. As a result, the high-temperature peak, which corresponds to a chemisorbed monolayer of ammonia, is well resolved from the low-temperature, multilayer peak. This clear separation was not observed, for example, on either the clean Ru-(001) surface or the Ru(001)–$(\sqrt{3}\times\sqrt{3})R30°$–N surface; cf. Figures 1 and 2. The fractional coverage of this ammonia monolayer, determined by comparison of the time-integrated area with the monolayer on the clean Ru-
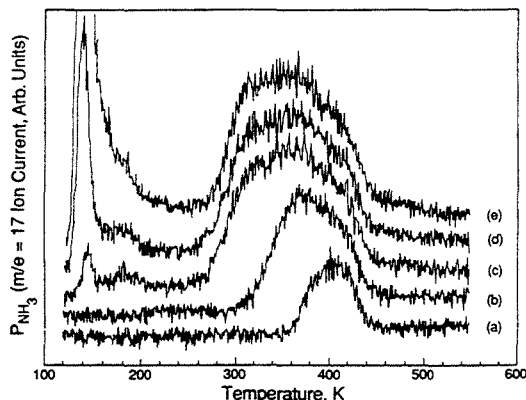

Figure 3. Thermal desorption spectra of ammonia on Ru(001)–p(2×2)–O at increasing ammonia exposures from parts a to e. The low-temperature peak does not saturate with increasing exposure. The heating rate is 3 K s^{-1}. The corresponding fractional coverages of ammonia are (a) 0.02, (b) 0.13, (c) 0.26, (d) 0.33, and (e) 0.56.

(001) surface, is approximately 0.24, approximately equal to that which is observed on the clean Ru(001) surface.

The (2×2) LEED pattern persisted with a brighter diffuse background following the adsorption of a "multilayer" of ammonia on Ru(001)–p(2×2)–O (an ammonia fractional coverage of 0.80). Annealing of this surface to 250 K, which caused desorption of the ammonia multilayer without removing the monolayer (cf. Figure 3), resulted in a decrease in the thermal diffuse background. Visually, the half-integral spots had the same intensity as the integral-order spots prior to annealing. After desorption of the ammonia monolayer, the half-integral spots became less intense than the integral spots, which is consistent with that observed for a Ru(001)–p(2×2)–O surface. No measurable amount of oxygen was removed from the surface following the desorption of ammonia, as verified by Auger electron spectroscopy, and no nitrogen-containing molecule (other than ammonia) was observed to desorb; i.e., the adsorption and desorption of molecular ammonia were completely reversible.

3.4. Ammonia on Ru(001)–p(1×2)–O. Thermal desorption spectra of ammonia, following various exposures of ammonia to the Ru(001)–p(1×2)–O surface, are shown in Figure 4. *In the limit of low-surface coverage*, the binding energy of ammonia, as judged by the temperature of desorption, is approximately the same on the Ru(001)–p(2×2)–O and Ru(001)–p(1×2)–O surfaces. The binding energy of the donor bond on both oxygen-modified surfaces is stronger than on either the nitrogen-modified surface or the clean surface. Compared to the clean surface, the binding energy is increased by approximately 20–25%. As may be seen in Figure 4, the most important difference between the desorption spectra of ammonia from the Ru-(001)–p(1×2)–O surface and the other three surfaces (cf. Figures 1–3) is the relative sharpness of the desorption peaks. This can be seen more clearly in Figure 5 where desorption from the clean Ru(001) surface is compared to desorption from the Ru(001)–p(1×2)–O surface and in Figure 6 where desorption from the Ru(001)–p(2×2)–O surface is compared with desorption from the Ru(001)–p(1×2)–O surface.

The results of LEED observations following the adsorption of ammonia on the Ru(001)–p(1×2)–O surface are essentially the same as those described earlier con-
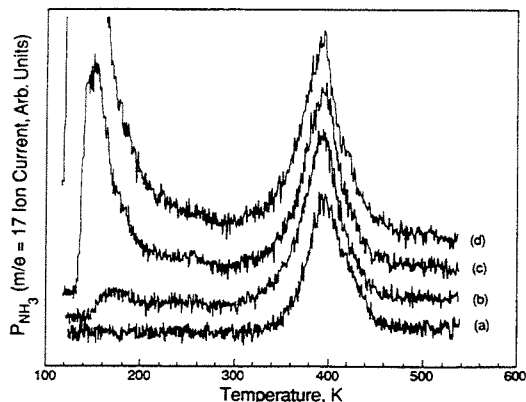
Figure 4. Thermal desorption spectra of ammonia on Ru(001)–p(1×2)–O at increasing ammonia exposures from parts a to d. The low-temperature peak does not saturate with increasing exposure. The heating rate is 3 K s^{-1}. The corresponding fractional coverages of ammonia are (a) 0.14, (b) 0.23, (c) 0.46, and (d) 0.89.
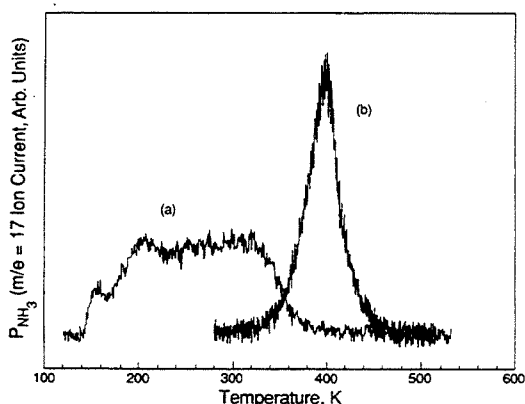

Figure 5. Comparison of the thermal desorption spectra of ammonia from (a) clean Ru(001) and the (b) Ru(001)–p(1×2)–O surface. The heating rate is 3 K s^{-1}. The corresponding fractional coverages of ammonia are (a) 0.30 and (b) 0.19.

Figure 6. Comparison of the thermal desorption spectra of ammonia from the (a) Ru(001)–p(2×2)–O and (b) Ru(001)–p(1×2)–O surfaces. The heating rate is 3 K s^{-1}. The corresponding fractional coverages of ammonia are (a) 0.23 and (b) 0.19.

Table I. The Binding Energy of Ammonia in the Low-Coverage Limit and the Fractional Coverage of the Saturated Monolayer of Ammonia on Ru(001) and Three Chemically Modified Surfaces of Ru(001)

surface	$E_d(\theta_{NH_3} \rightarrow 0)$, kcal/mol	$\theta_{NH_3}{}^S$
Ru(001)	21.5	0.25
$-(\sqrt{3}\times\sqrt{3})R30°$–N	24.2	0.16
–p(2×2)–O	26.2	0.24
–p(1×2)–O	26.2	0.22

This corresponds to an average static dipole moment per oxygen adatom that is approximately 3 times as great for the p(1×2) overlayer compared to the p(2×2) overlayer.[22] The strong depletion in the local density of occupied states of the Ru(001) surface in the presence of the p(1×2)–O overlayer obviates to a great extent the decrease in the binding energy of ammonia on this surface at higher coverages of ammonia compared to the other three surfaces that were studied; cf. Figures 2, 5, and 6. An additional contribution to this screening may be due to anisotropies in the binding site(s) of ammonia on the p(1×2)–O surface versus the clean surface.

4. Summary

The interaction of ammonia with three chemically modified surfaces of Ru(001), the Ru(001)–$(\sqrt{3}\times\sqrt{3})$-$R30°$–N, the Ru(001)–p(2×2)–O, and the Ru(001)–p(1×2)–O, has been investigated and compared with the adsorption of ammonia on the initially clean Ru(001) surface. On all four surfaces, adsorption at low temperature followed by transient thermal desorption measurements results in no detectable decomposition of the ammonia. Only molecular desorption of ammonia is observed in the thermal desorption.

There is an increase in the binding energy of the ammonia to the nitrogen-modified surface relative to the clean surface, and an even greater increase in the binding energy to the oxygen-modified surfaces. The binding energies in the low-ammonia-coverage limit on the four different surfaces are given in Table I. These binding energies were calculated assuming a constant preexponential factor of the first-order desorption rate coefficient of ammonia, the value of which is 5 × 10^{13} s^{-1}. Although the low-coverage binding energy of ammonia is the same

cerning adsorption on the Ru(001)–p(2×2)–O surface. Only the apparent (2×2) LEED pattern was observed at all coverages of ammonia, and at high coverages the thermal diffuse background increased in intensity. Just as on the other surfaces, the adsorption and desorption were completely reversible on Ru(001)–p(1×2)–O. There was neither oxygen depletion nor nitrogen desorption during the adsorption and desorption cycles. The saturated monolayer fractional coverage of ammonia on the Ru-(001)–p(1×2)–O surface is 0.22, which can be compared to 0.25 on the clean surface, 0.24 on the Ru(001)–p(2×2)–O surface, and approximately 0.16 on the Ru(001)–($\sqrt{3}\times\sqrt{3}$)-$R30°$–N surface.

The relative sharpness of the thermal desorption spectra of ammonia from the Ru(001)–p(1×2)–O surface is indicative of the fact that repulsive interactions among the adsorbed ammonia molecules are "screened" in some sense on this surface. The principal nature of this "screening" is qualitatively clear and is due to the electronic structure of the surface. The work function of the Ru(001) surface increases by 0.2 eV when the p(2×2)–O overlayer is formed, and it increases by 0.8 eV for the p(1×2)–O overlayer.[26]
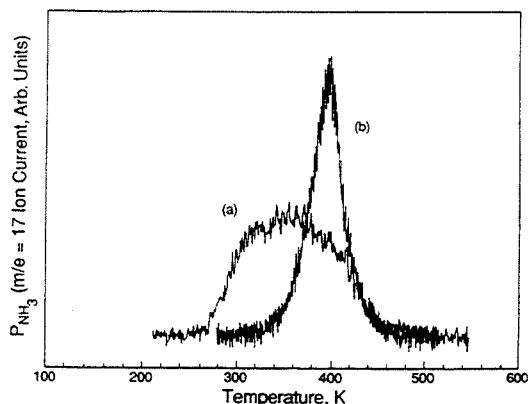
(26) Madey, T. E.; Engelhardt, H. A.; Menzel, D. *Surf. Sci.* 1975, 48, 304.

on both of the oxygen-modified surfaces, there are important differences between the two surfaces that become evident at higher fractional coverages of ammonia; cf. Figure 6. The p(1×2)–O overlayer is far more effective in "screening" the through-metal electron–electron repulsion that is an inevitable consequence of the nature of the electron-donor bonding of ammonia to the metallic substrate.

The saturation fractional coverages of the chemisorbed ammonia monolayer on the four surfaces are also listed in Table I. On the clean surface, the ammonia forms an ordered p(2×2) overlayer with one ammonia admolecule per four *substrate* unit cells. On the three chemically

modified surfaces, no ordered overlayers due to the presence of the ammonia are observed. At a temperature of 245 K, corresponding to a fractional coverage of ammonia of approximately 0.1, the $(\sqrt{3}\times\sqrt{3})R30°$–N superstructure transforms to a (2×2) LEED pattern, however. After desorption of the ammonia, the ground state of the nitrogen overlayer, i.e., the $(\sqrt{3}\times\sqrt{3})R30°$–N superstructure, is retrieved either by extended annealing at 400 K or by brief annealing at 500 K.

Chemisorption and Thermal Decomposition of Methylamine on the Ru(001) Surface

Dale F. Johnson, Youqi Wang, John E. Parmeter,[†] Malina M. Hills,[‡] and W. Henry Weinberg*

Contribution from the Department of Chemical Engineering, University of California, Santa Barbara, California 93106. Received October 21, 1991

Abstract: The adsorption and decomposition of monomethylamine on Ru(001) have been studied using high-resolution electron energy loss spectroscopy and thermal desorption mass spectrometry. Molecular adsorption of CH_3NH_2 occurs via lone pair donation of the nitrogen atom, and the desorption of reversibly adsorbed methylamine from a saturated first layer is observed over the temperature range 200–340 K. Thermal decomposition of irreversibly adsorbed methylamine ($\Theta_{CH_3NH_2} = 0.15 \pm 0.01$ monolayer) produces H_2, N_2, NH_3, and surface carbon adatoms. Between 280 and 300 K cleavage of a C–H bond produces μ-η^2-H_2CNH_2, and annealing above 300 K initiates competitive C–H and C–N bond cleavage reactions. The majority path (~70%) results in preferential cleavage of C–H bonds between 300 and 330 K to produce a mixture of η^1-(C)-HCNH$_2$ [ν(CN) = 1450 cm^{-1}] and μ-CNH$_2$ [ν(CN) = 1640 cm^{-1}] plus hydrogen adatoms. The minority path (~30%) gives rise to C–N bond cleavage between 300 and 320 K to yield short-lived CH_2 and NH_2 intermediates which react to form CH, NH, NH_3, and hydrogen adatoms. The ammonia is stabilized by the presence of electron-withdrawing intermediates and desorbs with a peak temperature of 365 K. Annealing between 330 and 360 K induces N–H bond cleavage in the majority path intermediates to form μ_3-η^2-HCNH [ν(CN) = 1450 cm^{-1}]. Cleavage of the final C–H bond between 370 and 380 K produces η^1-(C)-CNH [ν(CN) = 2275 cm^{-1}] and μ-CNH [ν(CN) = 1665 cm^{-1}], and this is followed by cleavage of the remaining N–H bond between 390 and 400 K to yield μ_3-η^2-CN [ν(CN) = 1660 cm^{-1}]. Rupture of the C–N bond over the temperature range 450–575 K forms carbon and nitrogen adatoms, the latter recombining to desorb as N_2 between 800 and 1000 K leaving only carbon on the surface.

I. Introduction

The study of the interaction of monomethylamine, CH_3NH_2, on the close-packed Ru(001) surface has been undertaken for a number of reasons. The selectivity of this surface toward activating CH, NH, and CN bonds can be determined by studying the decomposition of CH_3NH_2 with thermal desorption mass spectrometry and high-resolution electron energy loss spectroscopy. Such an analysis will also allow for the identification of stable reactive intermediates and, hence, provide insight into the mechanistic details of related catalytic reactions. Finally, it is of interest to contrast the interaction and decomposition of this amine to that of ammonia on the Ru(001) surface, as well as to its chemical reactivity on other single-crystalline surfaces.

The commercial importance of amines, amides, and isocyanates illustrates that there is much to be gained by the study and characterization of CN bond-containing molecules on single-crystalline transition-metal surfaces. Heterogeneous catalytic applications found in practice include hydrodenitrification,[1] reductive amination of alcohols,[2,3] reduction of nitriles,[4] and production of HCN.[5,6] Homogeneous catalytic processes of related importance include hydrocyanation[7] and reductive carbonylation[8] reactions; the former being applied in the manufacture of adiponitrile, $NC(CH_2)_4CN$, used to produce Nylon 66, and the latter being a route to produce aromatic isocyanates and possibly diisocyanates for use in the manufacture of polyurethanes. The isolation and identification of intermediates from the decomposition of methylamine on the close-packed Ru(001) surface will assist in clarifying the mechanistic details of these commercial processes. In particular the dehydrogenated surface species characterized here may play crucial roles in the disproportionation reactions observed[2,3,9] to occur during the production of long chain, aliphatic amines.[2,3,9] The findings of this study should be of wide interest and use to researchers in commercially applied catalysis.

Previous studies of monomethylamine on Pt(111),[10,11] Rh-(111),[11,12] Mo(100),[13] W(100), and carbon- and oxygen-modified W(100),[14] Cr(111) and Cr(100),[15] Ni(111),[15,16] Ni(100),[15,17] and Pt(100)[18] surfaces have been conducted with a variety of sur-face-sensitive techniques. Dehydrogenation of methylamine occurs on all surfaces between approximately 300 and 500 K, and the desorption of reversibly adsorbed molecular methylamine ceases near 400 K. The reactivity of each surface toward activating C–N bond cleavage varies dramatically, as determined by the gas-phase products other than H_2 formed from CH_3NH_2 decomposition. On Pt(111) methylamine undergoes no CN bond dissociation with only HCN and cyanogen produced, while on Rh(111), Pt(100), and Mo(100), it experiences partial dissociation as evidenced by cyanogen, HCN, N_2, and surface carbon production. On Ni(111), Ni(100), and W(100) surfaces it is completely dissociated, with only N_2 and surface carbon formed.

(1) (a) Ryan, R. C.; Adams, C. T.; Washecheck, D. M. U.S. Patent 4530911, 1985; *Chem. Abstr.* 1985, *103*, 382. (b) Laine, R. M. *Catal. Rev. Sci. Eng.* 1983, *25*, 459–474.
(2) Baiker, A.; Caprez, W.; Holstein, W. L. *Ind. Eng. Chem. Prod. Res. Dev.* 1983, *22*, 217–225.
(3) Baiker, A.; Richarz, W. *Ind. Eng. Chem. Prod. Res. Dev.* 1977, *16*, 261–266.
(4) Volf, J.; Pasek, J. In *Catalytic Hydrogenation*; Cerveny, L., Ed.; Studies in Surface Science and Catalysis; Elsevier Science: Amsterdam, 1986; Vol. 27, Chapter 4.
(5) Endter, F. *Platinum Met. Rev.* 1962, *6*, 9–10.
(6) Pirie, J. M. *Platinum Met. Rev.* 1958, *2*, 7–11.
(7) Collman, J. P.; Hegedus, L. S.; Norton, J. R.; Finke, R. G. *Principles and Applications of Organotransition Metal Chemistry*; University Science: Mill Valley, CA, 1987; pp 568–571.
(8) Reference 7, pp 643–644.
(9) Adams, R. D.; Kim, H.-S.; Wang, S. *J. Am. Chem. Soc.* 1985, *107*, 6107–6108; and references therein.
(10) Hwang, S. Y.; Seebauer, E. G.; Schmidt, L. D. *Surf. Sci.* 1987, *188*, 219–234.
(11) Cordonier, G. A.; Schüth, F.; Schmidt, L. D. *Vacuum* 1990, *41*, 278–281.
(12) Hwang, S. Y.; Kong, A. C. F.; Schmidt, L. D. *J. Phys. Chem.* 1989, *93*, 8327–8333.
(13) Walker, B. W.; Stair, P. C. *Surf. Sci.* 1981, *103*, 315–337.
(14) Pearlstine, K. A.; Friend, C. M. *J. Am. Chem. Soc.* 1986, *108*, 5842–5847.
(15) Baca, A. G.; Schulz, M. A.; Shirley, D. A. *J. Chem. Phys.* 1985, *83*, 6001–6008.
(16) Chorkendorff, I.; Russell, J. N., Jr.; Yates, J. T., Jr. *J. Chem. Phys.* 1987, *86*, 4692–4700.
(17) Schoofs, G. R.; Benziger, J. B. *J. Phys. Chem.* 1988, *92*, 741–750.
(18) Thomas, P. A.; Masel, R. I. *J. Vac. Sci. Technol. A* 1987, *5*, 1106–1108.

†Present address: Division 1126, Sandia National Laboratories, Albuquerque, NM 87185.
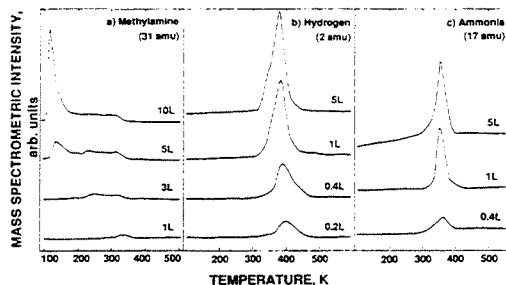‡Present address: Materials and Mechanics Technology Center, The Aerospace Corp., El Segundo, CA 90009.

Figure 1. Thermal desorption mass spectra of (a) molecular methylamine, (b) hydrogen, and (c) ammonia following the indicated exposures of CH_3NH_2 on Ru(001) at 80 K and annealed with a heating rate, β, of ~15 K s^{-1}.

II. Experimental Details

The high-resolution EEL spectrometer used in these studies as well as the ultrahigh vacuum chamber in which it is contained have been described in detail elsewhere.[19] Briefly, the stainless steel ultrahigh vacuum (UHV) chamber is pumped by both a 220 L s^{-1} noble ion pump and a titanium sublimation pump which reduce the base pressure to below 10^{-10} Torr. The home-built HREEL spectrometer is of the Kuyatt-Simpson type, with 180° hemispherical deflectors serving as the energy dispersing elements in both the monochromator and the analyzer. The monochromator is spatially fixed, but the analyzer is rotatable to allow off-specular spectra to be measured. On- and off-specular spectra were collected during these experiments, but all spectra presented in this paper were collected in the on-specular direction. The impact energy of the incident electron beam was between 4 and 6 eV in all cases, and the beam was incident on the Ru(001) crystal at an angle of 60° with respect to the surface normal. The instrumental energy resolution in these studies, defined as the full width at half maximum of the elastically scattered beam, varied between 60 and 80 cm^{-1}, while maintaining count rates in the elastic peak between 1.5 and 3.5 × 10^5 counts s^{-1}.

The Ru(001) crystal was cooled to 80 K with liquid nitrogen and was heated resistively with the temperature monitored by a W-5% Re/W-26% Re thermocouple spotwelded to the back of the crystal. The crystal was cleaned by using periodic ion sputtering and routine annealing to 1000 K in 1 × 10^{-7} Torr of O$_2$, followed by annealing to 1625 K in vacuo. Surface cleanliness was determined by both HREELS and H$_2$ thermal desorption mass spectrometry.

A second UHV chamber was used to conduct the thermal desorption mass spectrometry and low-energy electron diffraction measurements.[20] This chamber also has a base pressure below 10^{-10} Torr using similar pumping techniques. Liquid nitrogen cooling and resistive heating of the Ru(001) crystal were similarly employed. It contains a UTI-100C quadrupole mass spectrometer enclosed in a glass envelope for selective sampling of gases that desorb only from the well-oriented front face of the single crystal. Low-energy electron diffraction optics and a rotatable Faraday cup are available for the display of LEED patterns and the measurement of LEED beam profiles. No ordered LEED structures other than the (1 × 1) pattern of the unreconstructed substrate were observed following the adsorption of various coverages of methylamine and annealing to higher temperatures. Hence, no LEED results are discussed here. A single-pass cylindrical mirror electron energy analyzer with an integral electron gun is available for Auger electron spectroscopy. The Ru(001) crystal mounted in this chamber was cleaned as described above, and cleanliness was determined by both AES and H$_2$ thermal desorption mass spectrometry.

Methylamine, CH_3NH_2 (98.0% min), was obtained from Matheson, and N,N-dideuteromethylamine (99.1% minimum, 98% CH_3ND_2) was obtained from MSD Isotopes. Perdeuteromethylamine (98% minimum, 95% CD_3ND_2) was obtained from Protech. All three isotopes of methylamine were further purified by several freeze-pump-thaw cycles prior to use. The purity of all gases was verified by mass spectrometry in both chambers. Gas exposures are reported in units of langmuirs, where 1 langmuir = 1 × 10^{-6} Torr s. The quoted exposures have not been corrected for the relative ionization probabilities of methylamine and nitrogen.
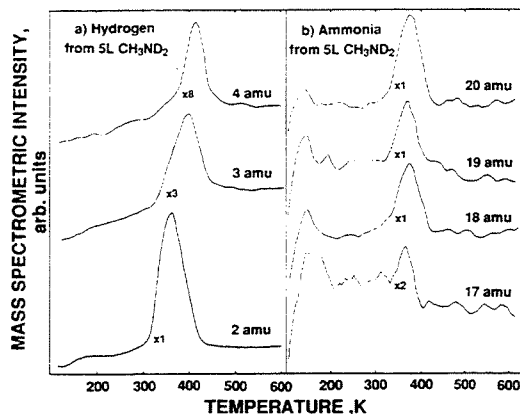
(19) Thomas, G. E.; Weinberg, W. H. *Rev. Sci. Instrum.* **1979**, *50*, 497–501.
(20) Williams, E. D.; Weinberg, W. H. *Surf. Sci.* **1979**, *82*, 93–101.

Figure 2. Thermal desorption mass spectra of (a) hydrogen and (b) ammonia following a 5-langmuir exposure of CH_3ND_2 on Ru(001) at 80 K and annealed with a heating rate, β, of ~15 K s^{-1}.

III. Results

A. Thermal Desorption Mass Spectrometry. Thermal desorption spectra measured after the adsorption of CH_3NH_2 and CH_3ND_2 on Ru(001) at temperatures below 100 K and subsequently ramped with heating rates, β, of 15 K s^{-1} are shown in Figures 1 and 2. Only molecular methylamine, hydrogen, nitrogen, and ammonia desorb from these overlayers with surface carbon also deposited as a result of the reaction. In particular, cyanogen, hydrogen cyanide, and methane are not observed. In Figure 1a, molecular methylamine desorbs in a peak at 330 K for low initial coverages of between 0.2 and 1 langmuir, and this peak downshifts and broadens with increasing coverage. Assuming a preexponential factor of the desorption rate coefficient of 10^{13} to 10^{14} s^{-1}, the activation energy of desorption of methylamine at low coverages is estimated by the Redhead method[21] to be 23 ± 2 kcal mol^{-1}. At intermediate exposures a second peak appears at 240–250 K, which saturates for exposures of 3 to 4 langmuirs. Finally, at high exposures a peak at 130 K, which does not saturate with increasing exposures, appears and is due to desorption from multilayer methylamine.

In addition to reversibly adsorbed CH_3NH_2, the observed desorption of H$_2$, N$_2$, and NH$_3$ indicates that irreversible, dissociative adsorption of methylamine occurs. From Figure 1b, it is seen that with increasing exposures the peak desorption temperature of H$_2$ shifts from 395 to 375 K. From a saturated monolayer of methylamine, a low-temperature shoulder at approximately 350 K appears. For the heating rate of 15 K s^{-1} employed in these thermal desorption experiments, all of the H$_2$ is seen to desorb from the surface by 450–460 K.

Ammonia produced from the decomposition of methylamine desorbs over the temperature range of 300 to 400 K with a peak desorption temperature of 365–370 K independent of the initial coverage of methylamine; cf. Figure 1c. This desorption behavior differs from that of similarly low coverages of ammonia on clean Ru(001) where desorption is complete by approximately 360 K and the peak temperature is 315 K.[22,23] Thermal desorption spectra of N$_2$ (not shown) indicate that the desorption peak temperature shifts from 950 to 875 K with increasing methylamine coverage. This coverage dependence and the high desorption temperatures indicate that desorption results from the second-order recombination of nitrogen adatoms. The desorption of N$_2$ from the decomposition of ammonia on Ru(001)[24] exhibits a similar coverage dependence although the desorption temperature is

(21) Redhead, P. A. *Vacuum* **1962**, 203–211.
(22) Benndorf, C.; Madey, T. E. *Surf. Sci.* **1983**, *135*, 164–183.
(23) Parmeter, J. E.; Wang, Y.; Mullins, C. B.; Weinberg, W. H. *J. Chem. Phys.* **1988**, *88*, 5225–5236.
(24) Tsai, W.; Weinberg, W. H. *J. Phys. Chem.* **1987**, *91*, 5302–5307.

Methylamine on the Ru(001) Surface

J. Am. Chem. Soc., Vol. 114, No. 11, 1992 4281

approximately 100 K lower. The presence of carbon adatoms causes the recombinative desorption of dinitrogen to occur at higher temperatures by either increasing the ruthenium–nitrogen bond energy, hindering nitrogen adatom surface diffusion via a site blocking mechanism, or a combination of both effects.

Figure 2 shows the thermal desorption spectra of masses 2, 3, and 4 amu (panel a) and masses 17, 18, 19, and 20 amu (panel b) that result from annealing a 5-langmuir exposure of *N,N*-dideuteromethylamine adsorbed at 95 K. The hydrogen isotopes are all desorbed by 460 K with the peak desorption temperatures being 360, 395, and 415 K, respectively, for H_2, HD, and D_2. Thermal desorption of isotopically pure, saturated H and D coverages on clean Ru(001)[25] gives virtually identical desorption spectra with their peak desorption temperatures occurring at 370 K and a high temperature shoulder at 415–420 K.

Figure 2b shows the desorption spectra of ammonia isotopes and their fragments formed from CH_3ND_2. The two parent isotopes, ND_3^+ (20 amu) and ND_2H^+ (19 amu), are responsible for the signals at masses 17 and 18 amu. Cleavage of one N–D bond in ND_3 yields the fragment ND_2^+ as does cleavage of the N–H bond in ND_2H. Likewise, the cleavage of one of the two N–D bonds of ND_2H yields the fragment NDH^+ of mass 17 amu. Mass spectrometric and high-resolution EEL spectroscopic verification of the purity of N,N-dideuteromethylamine eliminates the possibility of H–D exchange at the nitrogen atom in the parent molecule, and hence there is no possibility that these spectrometric fragment signals at 17 and 18 amu arise from ammonia molecules, NH_2D^+ and NH_3^+. Furthermore, as discussed in section IVB, hydrogenation of either surface nitrogen adatoms or deuterated imidogen, ND, to form NH_3 and NH_2D is not at all likely under these ultrahigh vacuum conditions.[24] The integrated areas under the desorption peaks reveal that $ND_3^+ > ND_2^+ > ND_2H^+ > NDH^+$, and that their relative areas, uncorrected for varying spectrometric sensitivities, are respectively 0.42:0.35:0.17:0.06.

The high-resolution EELS data presented in the next section demonstrate that side-on bonded cyano, CN, is formed as the product of complete dehydrogenation of methylamine. The detection of ammonia in the thermal desorption experiments shows that C–N bond cleavage competes with complete dehydrogenation. Analysis of the NH_3 and H_2 thermal desorption spectra resulting from several experiments of saturated coverages of CH_3NH_2 yields the fractional coverages of ammonia and atomic hydrogen: $\Theta_{NH_3} = 0.02 \pm 0.01$ and $\Theta_H = 0.70 \pm 0.03$. These fractional coverages are obtained by comparing the areas of the products to those for saturated exposures of NH_3 and H_2 and applying the known saturated coverages:[22,26] $\Theta_{NH_3}^{satd} = 0.25$ and $\Theta_H^{satd} = 1.00$. Applying a hydrogen mass balance on these data yields a fractional coverage of irreversibly adsorbed methylamine of $\Theta_{CH_3NH_2} = 0.15 \pm 0.01$. Quantification of the branching ratio between competing C–N bond cleavage and complete dehydrogenation reaction paths will be discussed in section IVB.

B. High-Resolution Electron Energy Loss Spectroscopy. While the thermal desorption data suggest the overall course followed by the surface-catalyzed decomposition of methylamine, it is the high-resolution EELS results which allow a *direct* observation of the chemical changes that occur as the reaction proceeds. The production of ammonia indicates that C–N bond breaking takes place in some fraction of the adsorbed CH_3NH_2, and, as will be developed in this section, this path competes with complete dehydrogenation. Careful analysis of the HREEL spectra allows numerous surface intermediates to be identified and, in particular, that one which is present prior to the branching of the reaction and hence common to both competing pathways.

High-resolution EEL spectra were measured with two different types of experimental annealing treatments. In order to coincide with the temperature-dependent features of the thermal desorption spectra, flash annealing ($\beta \approx 20$ K s^{-1}) of the crystal to the desired temperature was followed by rapid cooling to liquid nitrogen

(25) Feulner, P.; Pfnür, H.; Hofmann, P.; Menzel, D. *Surf. Sci.* **1987**, *184*, L411–L414.
(26) Sun, Y.-K.; Weinberg, W. H. *Surf. Sci.* **1989**, *214*, L246–L252.
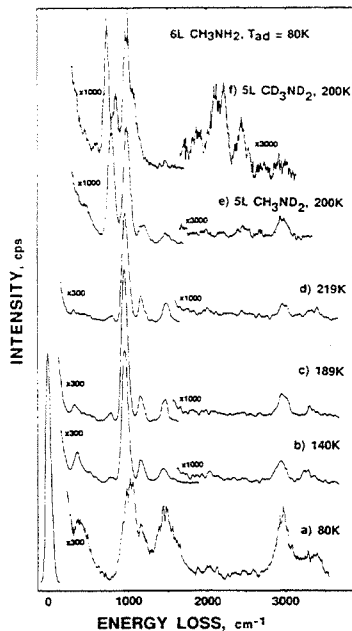

Figure 3. High-resolution EEL spectra resulting from saturation exposures of methylamine and its deuterated isotopes on the Ru(001) surface at 80 K and then annealed rapidly to the indicated temperatures: (a) 80 K, this spectrum is characteristic of partial multilayers of methylamine; (b) 140 K, this spectrum is characteristic of second-layer methylamine; (c) 189 K; (d) 219 K, this spectrum is characteristic of first-layer molecular methylamine; (e and f), 200 K, these spectra are characteristic of first-layer molecular CH_3ND_2 and CD_3ND_2, respectively. See text.

temperature. A second series of HREEL spectra to investigate the surface intermediates of the reaction required similarly rapid but careful annealing in order to control the extent of conversion. The spectra in this second set of data were typically measured at 10-degree increments, and upon observing significant change in a spectrum, a second and sometimes third spectrum was obtained at that annealing temperature. Numerous off-specular spectra (typically 5–10°) were measured, and, while none are shown here, the findings of these spectra are embodied in the discussion in the text. During the course of the experiments, CO from the chamber background adsorbed on the crystal. Its surface concentration is always extremely low, and only because of the very large dynamic dipole moment for the CO stretching frequency is it observed in the spectra. Readsorption of methylamine was kept to a minimum by use of a cyropanel throughout the duration of the experiments.

The HREEL spectra following saturation exposures of either CH_3NH_2, CH_3ND_2, or CD_3ND_2 (typically between 4 and 6 langmuir exposures adsorbed at 80–90 K) and subsequently annealed to the indicated temperatures are presented in Figures 3–6. A spectrum characteristic of methylamine multilayers is shown in Figure 3a when the crystal at a temperature of 80 K is exposed to greater than 6 langmuirs of methylamine. Annealing this multilayer coverage to 140 K induces the desorption of the multilayers (cf. Figure 1a) and results in the spectrum of Figure 3b. This spectrum is that of second-layer methylamine, a designation supported by observed changes as the surface is further annealed to above 200 K. The librational mode, or frustrated rotation parallel to the surface plane, R_{xy}, at 365 cm^{-1}, is seen to attenuate upon annealing to 189 K, and its disappearance by 200–220 K coincides precisely with the second-layer desorption results of Figure 1a.

Upon the desorption of the second layer, the overlayer present on the surface is that of a saturated first layer of methylamine. Parts d–f of Figure 3 represent the spectra for molecularly ad-

Table I. Vibrational Frequencies (cm^{-1}) of First and Second Layer Methylamine and Spectroscopic Reference Data[d]

mode	2nd layer 140 K	satd 1st layer, 200–220 K			CH$_3$NH$_2$		CH$_3$ND$_2$		CD$_3$ND$_2$	
		CH$_3$NH$_2$	CH$_3$ND$_2$	CD$_3$ND$_2$	gas[a]	solid[b]	gas[a]	solid[b]	gas[a]	solid[b]
ν_a(NH$_2$) or ν_a(ND$_2$)	3240	3255			3427	3331	2556	2484	2556	2485
			2460	2450						
ν_s(NH$_2$) or ν_s(ND$_2$)	3190	3200			3361	3260	2479	2443	2477	2445
ν_a(CH$_3$) or ν_a(CD$_3$)					2985	2942	2985	2941	2238	2220
	2905	2920	2920	2200						
ν_a(CH$_3$) or ν_a(CD$_3$)					2961	2887	2961	2863	2202	2190
ν_s(CH$_3$) or ν_s(CD$_3$)	2840	2865	2895	2085	2820	2793	2817	2801	2073	2061
δ(NH$_2$) or δ(ND$_2$)	1555	1560[c]	1210	n.r.	1623	1651	1234	1220	1227	1217
δ_a(CH$_3$) or δ_a(CD$_3$)					1485	1492	1485	1470	1077	1121
	n.r.	n.r.	n.r.	n.r.						
δ_a(CH$_3$) or δ_a(CD$_3$)					1473	1467	1468	1448	1065	1070
δ_s(CH$_3$) or δ_s(CD$_3$)	1425	1425	1465	1055	1430	1441	1430	1421	1123	1050
τ(NH$_2$) or τ(ND$_2$)	n.o.	n.o.	n.o.	n.o.	1455	1353	1140	1130	1110	1070
ω_a(CH$_3$) or ω_a(CD$_3$)					1195	1172	1187	1189	910	929
	1180	1190	1170	850						
ω_s(CH$_3$) or ω_s(CD$_3$)					1130	1182	1117	1130	880	919
ν(CN)	1000	1025[c]	995	975	1044	1048	997	1005	942	942
ω(NH$_2$) or ω(ND$_2$)	1000	980[c]	780	730	780	955	624	751	601	730
NH$_2$ or ND$_2$ torsion	n.o.	n.o.	n.o.	n.o.	264	498	229	360	201	365
ρ(NH$_2$) or ρ(ND$_2$)	775	780	n.r.	n.r.						
R_{xy}	365									
ν(Ru–N)	n.r.	340	335[c]	n.r.						

[a] Reference 27. [b] Reference 28. [c] Resolved off-specular. [d] Key: n.r., not resolved; n.o. not observed; a, asymmetric; s, symmetric.

sorbed, saturated first-layer coverages of CH$_3$NH$_2$, CH$_3$ND$_2$, and CD$_3$ND$_2$, respectively. Mode assignments for the first- and second-layer methylamine and vibrational gas and solid phase references[27,28] are listed in Table I. It is evident that no bonds have been broken, and, furthermore, the molecule is bonded to the surface through the nitrogen atom's donation of its lone pair of electrons. Evidence for this bonding interaction lies in the strong wagging and overlapping deformation modes of the methyl group, ω(CH$_3$) at 1180 cm^{-1} and δ_a(CH$_3$) and δ_s(CH$_3$) at 1425 cm^{-1}, and the hydrogenic stretching modes, ν(NH$_2$) at 3200–3300 cm^{-1} and ν(CH$_3$) at 2900–2950 cm^{-1}. The nitrogen's coordination to the surface is borne out by the ν(Ru–N) stretching mode at 340–350 cm^{-1} in the spectra of the three isotopes between 200 and 220 K, in excellent agreement with that observed for NH$_3$ on Ru(001).[23]

Annealing the saturated first layer above 220 K results in competitive molecular desorption and conversion, via C–H bond cleavage, to form chemisorbed methyleniminium, CH$_2$NH$_2$. From examination of the spectra, these two processes appear to act in consort with one another in that as one molecule desorbs, an active site on the surface becomes available to catalyze the cleavage of a CH bond in a neighboring methylamine molecule. This reaction to form H$_2$CNH$_2$ occurs most rapidly over the temperature range of 280–300 K, as illustrated in Figure 4a–c where the deformation modes of the methyl group at 1460 cm^{-1} are lost, while a strong loss feature at 555 cm^{-1} appears. The methyleniminium intermediate coordinates to the surface in a side-on bridging manner in which the carbon and nitrogen atoms bond to neighboring Ru atoms on the surface. This μ-η^2-H$_2$CNH$_2$ coordination gives rise to the broad intense loss features observed at 555 cm^{-1} for CH$_2$NH$_2$, 540 cm^{-1} for CH$_2$ND$_2$, and 510 cm^{-1} for CD$_2$ND$_2$ and assigned to the symmetric and antisymmetric stretching modes of the Ru–CN complex. The di-σ bonding configuration is further supported by the agreement of the CH$_2$ scissoring and wagging modes at 1430 and 1195 cm^{-1}, respectively, to those of di-σ bonded ethylene on clean Ru(001) which appear at 1450 and 1145 cm^{-1}.[29] If the CH$_2$NH$_2$ intermediate were π-bonded to the surface, this would require sp^2 hybridization for the carbon and nitrogen atoms, resulting in δ(CH$_2$) and ω(CH$_2$) frequencies closer to values of unperturbed gas-phase ethylene, i.e., 1444 and 949 cm^{-1}, respectively,[30] or of π-bonded ethylene in Zeise's salt, K[PtCl$_3$-

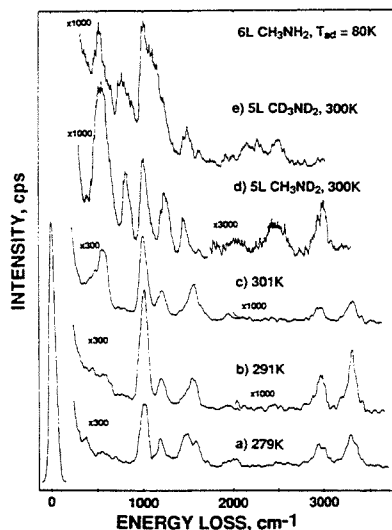**Figure 4.** High-resolution EEL spectra resulting from saturation exposures of methylamine and its deuterated isotopes on the Ru(001) surface at 80 K and rapidly annealed to the indicated temperatures: (a and b) 279–291 K, these spectra illustrate the conversion of molecularly adsorbed methylamine to the bridging iminium intermediates; (c) 301 K, this spectrum is characteristic of μ-η^2-H$_2$CNH$_2$; (d and e) 300 K, these spectra are characteristic of the deuterated bridging iminium intermediates, μ-η^2-H$_2$CND$_2$ and μ-η^2-D$_2$CND$_2$, respectively. See text.

(C$_2$H$_4$)],[31] in which δ(CH$_2$) = 1515 cm^{-1} and ω(CH$_2$) = 975 cm^{-1}. Organometallic analogues of the bridging CH$_2$NH$_2$ intermediate have been synthesized and crystallographically characterized by Adams et al.[32] The bridging (dimethylamino)iminium ligand, μ-η^2-H$_2$CNMe$_2$, in the triosmium compound, Os$_3$(CO)$_{10}$(μ-η^2-H$_2$CNMe$_2$)(μ-H) has a C–N bond distance of 1.53 Å and internal bond angles that indicate sp^3 hybridization of both the carbon and

(27) Gray, A. P.; Lord, R. C. J. Chem. Phys. 1957, 26, 690–705.
(28) Durig, J. R.; Bush, S. F.; Baglin, F. G. J. Chem. Phys. 1968, 49, 2106–2117.
(29) Hills, M. M.; Parmeter, J. E.; Mullins, C. B.; Weinberg, W. H. J. Am. Chem. Soc. 1986, 108, 3554–3562.

(30) Shimanouchi, T. Tables of Molecular Vibrational Frequencies; National Institute of Standards and Technology: Washington, DC, 1972; Consolidated Volume, NSRDS-NBS-39, p 74.
(31) Hiraishi, J. Spectrochim. Acta, Part A 1969, 25A, 749–760.
(32) (a) Adams, R. D.; Babin, J. E. Organometallics 1988, 7, 963–969.
(b) Adams, R. D.; Babin, J. E.; Kim, H.-S. Organometallics 1987, 6, 749–754.

Table II. Vibrational Frequencies (cm⁻¹) and Mode Assignments for Side-on Bonded Methyleniminium, $\mu\text{-}\eta^2\text{-}H_2CNH_2$, Terminally Bound Secondary Aminocarbene, $\eta^1\text{-(C)-HCNH}_2$, Bridging Aminocarbyne, $\mu\text{-CNH}_2$, and Ammonia, NH_3[a,d]

mode	methyleniminium, 280–320 K			secondary aminocarbene, 310–350 K			aminocarbyne, 310–360 K		ammonia, 310–370 K	
	H_2CNH_2	H_2CND_2	D_2CND_2	$HCNH_2$	$HCND_2$	$DCND_2$	CNH_2	CND_2	NH_3	ND_3
$\nu_a(NH_2)$ or $\nu_a(ND_2)$	3340	2510	2510	3250	2450	2450	3250	2450		
$\nu_s(NH_2)$ or $\nu_s(ND_2)$	3300	2400	2450	3175	2325	2325	3175	2325		
$\nu_a(NH_3)$ or $\nu_a(ND_3)$										
$\nu_s(NH_3)$ or $\nu_s(ND_3)$									3250	2500
$\nu_a(CH_2)$ or $\nu_a(CD_2)$	2950	2950	2225							
$\nu_s(CH_2)$ or $\nu_s(CD_2)$	2900	2900	2150							
$\nu(CH)$ or $\nu(CD)$				2920	2920	2200				
$\delta(NH_2)$ or $\delta(ND_2)$	1545	1260	1250	1545	1260	1250	1545	1260		
$\delta(CH_2)$ or $\delta(CD_2)$	1430[b]	1425	1100							
$\delta_s(NH_3)$ or $\delta_s(ND_3)$									1215	1000
$\delta(CH)$ or $\delta(CD)$				740	740	550				
$\pi(CH)$ or $\pi(CD)$				980	980	720				
$\omega(CH_2)$ or $\omega(CD_2)$	1190	1180	900							
$\omega(NH_2)$ or $\omega(ND_2)$	980[b]	810	800	740	550	550	740	550		
$\nu(CN)$	1005	1000	1000	1420	1430	1430	1620	1620		
$\rho(NH_2)$ or $\rho(ND_2)$	790[c]	n.r.	n.r.	1050	750	750	1050	750		
$\rho(CH_2)$ or $\rho(CD_2)$	680[b]	n.r.	n.r.							
$\nu_a(Ru\text{-}CN)$	555	540	540							
$\nu_s(Ru\text{-}CN)$										
$\nu(Ru\text{-}C)$				n.r.	n.r.	n.r.	n.r.	n.r.		
$\nu(Ru\text{-}N)$									n.r.	n.r.

[a] Indicated temperatures in the column headings correspond to the ranges in which each intermediate populates the surface and influences the high-resolution EEL spectra; refer to text and figures. [b] Resolved off-specular. [c] Reproducibly observed in other HREEL spectra. [d] Key: n.r., not resolved; a, asymmetric; s, symmetric.

nitrogen atoms. The interpretation of the broad intense loss features at 555 cm⁻¹ for CH₂NH₂ as the overlapping bridge-bonded symmetric and asymmetric stretching modes is supported by strong infrared absorption bands between 506 and 589 cm⁻¹ for bidentate ethylenediamine in Pt, Pd, Cu, and Ni organometallic complexes[33] and also by a very strong HREELS loss feature centered at 565 cm⁻¹ for ethylenediamine adsorbed on Pd(111).[34] The complete mode assignments for $\mu\text{-}\eta^2\text{-}H_2CNH_2$ and its isotopes present on the surface at 300 K are given in Table II.

Requiring comment beyond the mode assignments of Table II is the appearance of a loss feature at 1430 cm⁻¹ in Figure 4e. While this feature is assigned as the symmetric deformation, or scissoring, mode of the CH₂ group in the spectra of H₂CNH₂ and H₂CND₂ in parts c and d of Figure 4, respectively, the intermediate D₂CND₂ generates no loss feature assignable to that observed at 1430 cm⁻¹. The possibility of contamination by some hydrogen-containing methylamine is discarded because the purity of these isotopes was verified by mass spectrometric characterization prior to their use. The appearance of this loss feature results from the reaction having progressed beyond pure D₂CND₂, and there being subsequent decomposition products on the surface as well as the deuterated methyleniminium, D₂CND₂. Additional evidence of the reaction having proceeded beyond pure D₂CND₂ is the comparatively weak ν(Ru–CN) stretching modes at 510 cm⁻¹ relative to loss features at 540 and 555 cm⁻¹ in the spectra of H₂CND₂ and H₂CNH₂, respectively. While the temperature indicated in Figure 4e is 300 K, it is likely that in the operation of flash annealing the crystal, this temperature was actually overshot slightly, thereby inducing the decomposition reaction to proceed beyond pure CD₂ND₂, vide infra.

Careful annealing of the crystal between 300 and 330 K produces dramatic changes in the spectra as illustrated in Figure 5a–c. Three loss features assignable to bridging methyleniminium at 300 K are no longer present at 330 K: The strong Ru–CN stretching modes at 555–565 cm⁻¹, the CN stretching mode at 1000 cm⁻¹, and the CH₂ stretching modes at 2800–3000 cm⁻¹.

(33) (a) Adams, D. M. *Metal-Ligand and Related Vibrations*; Edward Arnold: London, 1967; p 309. (b) Powell, D. B.; Sheppard, N. *Spectrochim. Acta* **1961**, *17*, 68–76.
(34) Kordesch, M. E.; Stenzel, W.; Conrad, H. *Surf. Sci.* **1987**, *186*, 601–623.
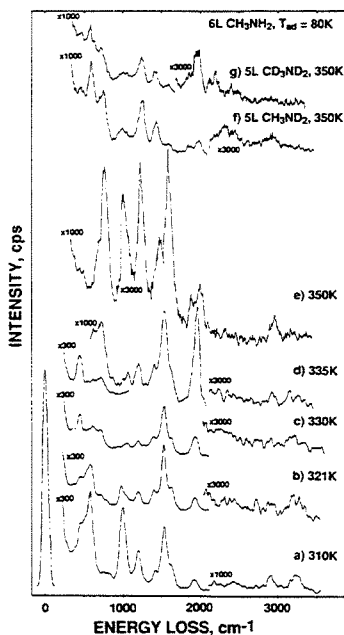

Figure 5. High-resolution EEL spectra resulting from saturation exposures of methylamine and its deuterated isotopes on the Ru(001) surface at 80 K and rapidly annealed to the indicated temperatures: (a and b) 310–321 K, these spectra illustrate the conversion of bridging iminium to the mixture of bridging aminocarbyne and secondary aminocarbene intermediates; (c) 330 K, this spectrum is characteristic of $\eta^1\text{-(C)-}$ HCNH₂ and $\mu\text{-CNH}_2$; (d and e) 335–350 K, these spectra illustrate the conversion of secondary aminocarbene to formimidoyl; (f and g) 350 K, these spectra are characteristic of mixtures of the deuterated isotopes of the bridging carbyne, secondary aminocarbene, and formimidoyl intermediates. See text.

In place of these loss features appear new peaks at 1070, 1220, and 730 cm⁻¹, accompanied by a noticeable sharpening of the

amine scissoring mode at 1545 cm^{-1} with resolvable features at 1420 and 1640 cm^{-1}. The disappearance of the 1000-cm^{-1} peak assigned to the overlapping ν(CN) and ω(NH$_2$) modes of μ-η^2-H$_2$CNH$_2$ coincides with the loss of the ν(Ru–CN) stretching modes. The changes seen between 300 and 330 K can be interpreted best by the decomposition of methyleniminium into several new surface products.

Cleavage of one CH bond occurs to form the secondary aminocarbene, HCNH$_2$, which is bound to the surface through the carbon atom only, possibly at an on-top site of a single Ru atom. This terminally bound coordination is represented as η^1-(C)-HCNH$_2$ in which both the carbon and nitrogen atoms are sp^2 hybridized with a partial double bond between them. Back donation from the surface to the antibonding π^* orbital of the planar HCHN$_2$ intermediate serves to yield a CN stretching frequency of 1420–1430 cm^{-1}. The assignment of this loss feature to the ν(CN) of η^1-(C)-HCNH$_2$ is supported by its presence in the spectra of the deuterated isotopes that have been annealed to 350 K in Figure 5f,g.

The precedence for this terminally bound secondary aminocarbene is obtained from organometallic cluster chemistry. Adams et al.[35] in a very thorough series of studies of triosmium cluster compounds have demonstrated the stability of the terminally bound (dimethylamino)carbene ligand, HCNMe$_2$. Its crystallographic characterization yields a CN bond distance of 1.27–1.29 Å, in excellent agreement with that of a CN double bond,[36] and a planar geometry with the carbon and nitrogen both having nearly ideal sp^2 hybridization. Infrared data on the (dimethylamino)carbene ligand are not reported, but as a point of reference the CN stretching frequency in gas-phase methylenimine, H$_2$C=NH, is 1638 cm^{-1}.[37]

Cleavage of both CH bonds of the H$_2$CNH$_2$ intermediate produces the aminocarbyne intermediate, CNH$_2$, which has its CN bond axis perpendicular to the surface and bonds in a bridging fashion across a 2-fold surface Ru site. This μ-CNH$_2$ product is characterized by a very strong scissoring deformation of the NH$_2$ group and a CN stretching mode of 1640 cm^{-1}. The aminocarbyne intermediate appears to be produced upon annealing the surface above 300 K and is stable to 360 K. (Dimethylamino)carbyne ligands are found in organometallic cluster compounds, such as Ru$_3$(CO)$_{10}$(μ-CNMe$_2$) synthesized by Churchill[38] and in a variety of compounds synthesized by Adams et al.[32,35,39]

Both η^1-(C)-HCNH$_2$ and μ-CNH$_2$ have sp^2 valence hybridization and planar geometries. As a result of this rehybridization, the wagging and rocking modes of the amine group undergo significant shifts. A compilation of documented shifts in these and other modes of –CH$_2$ and –CH groups as the carbon-atom hybridization varies is provided by Ibach and Mills.[40] For both the secondary aminocarbene and the bridging aminocarbyne, the ω(NH$_2$) mode has a large red shift to 720–750 cm^{-1}, and the ρ(NH$_2$) mode has a blue shift to 1070 cm^{-1}. As noted earlier, similar shifts in these fundamental modes of an sp^3-hybridized methylene group are seen for di-σ-bonded ethylene on Ru(001)[29] when compared to sp^2-hybridized methylene groups in gas-phase ethylene and π-coordinated ethylene in Zeise's salt.[30,31]

As will be discussed later in relation to the quantification of the branching ratio between the dehydrogenation and CN bond cleavage reaction pathways, the methyleniminium, H$_2$CNH$_2$, is
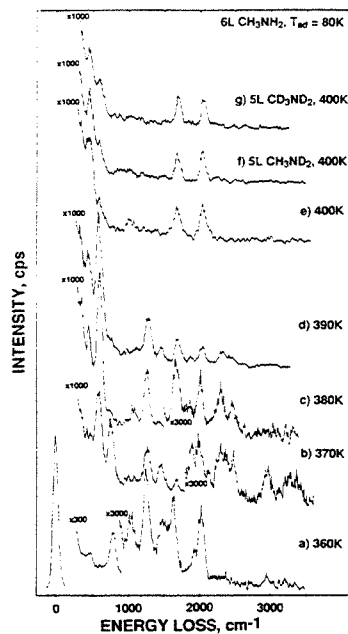

Figure 6. High-resolution EEL spectra resulting from saturation exposures of methylamine and its deuterated isotopes on the Ru(001) surface at 80 K and rapidly annealed to the indicated temperatures: (a) 360 K, this spectrum is characteristic of the mixture of μ-CNH$_2$ and μ_3-η^2-HCNH, (b and c) 370–380 K, these spectra illustrate the conversion of the overlayer present at 360 K to the mixture of terminally bound and bridge bound hydrogen isocyanide; (d) 390 K, this spectrum is characteristic of η^1-(C)-CNH and μ-CNH; (e–g) 400 K, these spectra are characteristic of μ_3-η^2-CN. See text.

the intermediate from which C–N bond cleavage leads to the production of ammonia. Upon annealing above 300 K and by 330 K the loss feature at 1185 cm^{-1} assigned to the ω(CH$_2$) mode of H$_2$CNH$_2$ is attenuated and in its place appears a higher energy loss feature at 1215 cm^{-1}. This feature is from the symmetric deformation of the ammonia product, δ_s(NH$_3$), and is blue shifted in its frequency due to the presence of electron-withdrawing intermediates on the surface. On clean Ru(001) ammonia's symmetric deformation mode monotonically shifts from 1160 cm^{-1} at low coverages to 1070 cm^{-1} at saturation coverages.[23] In the presence of a p-(1×2) overlayer of oxygen on Ru(001), low coverages of ammonia exhibit δ_s(NH$_3$) at 1220 cm^{-1}.[41]

When the C–N bond cleaves, surface methylene and amido groups are formed. Neither CH$_2$ nor NH$_2$ are stable surface intermediates on Ru(001) under these conditions: the former dehydrogenating to methylidyne, CH, and hydrogen adatoms, and the latter either dehydrogenating to imidogen, NH, and hydrogen or being hydrogenated to produce adsorbed ammonia.[24,42] High-resolution EELS loss features of methylidyne and imidogen demonstrate CH and NH bending deformation modes at 800 and 1340 cm^{-1}, respectively.[43,44] Methylidyne and imidogen bending modes are unresolved from overlapping loss features of the predominant η^1-(C)-HCNH$_2$ and μ-CNH$_2$ intermediates. Furthermore, there is such a low coverage of imidogen, methylidyne, and ammonia that their respective loss features are just at or below the HREELS experimental detection limits, and this issue shall

(35) (a) Adams, R. D.; Babin, J. E.; Kim, H.-S.; Tanner, J. T.; Wolfe, T. A. *J. Am. Chem. Soc.* **1990**, *112*, 3426–3435. (b) Adams, R. D.; Babin, J. E.; Kim, H.-S. *J. Am. Chem. Soc.* **1987**, *109*, 1414–1424. (c) Adams, R. D.; Babin, J. E. *Organometallics* **1987**, *6*, 1364–1365. (d) Adams, R. D.; Babin, J. E.; Kim, H.-S. *Inorg. Chem.* **1986**, *25*, 4319–4320. (e) Adams, R. D.; Babin, J. E.; Kim, H.-S. *Organometallics* **1986**, *5*, 1924–1925.

(36) (a) *International Tables for X-ray Crystallography*; Kynoch Press: birmingham, England, 1975; Vol. III, Table 4.2.4, p 276. (b) Pearson, R.; Lovas, F. J. *J. Chem. Phys.* **1977**, *66*, 4149–4156.

(37) Hamada, Y.; Hashiguchi, K.; Tsuboi, M. *J. Mol. Spectrosc.* **1984**, *105*, 70–80.

(38) Churchill, J. R.; DeBoer, B. G.; Rotella, F. J. *Inorg. Chem.* **1976**, *15*, 1843–1853.

(39) Adams, R. D.; Babin, J. E. *Organometallics* **1987**, *6*, 2236–2241.

(40) Ibach, H.; Mills, D. L. *Electron Energy Loss Spectroscopy and Surface Vibrations*; Academic: New York, 1982; pp 193–198.

(41) Wang, Y.; Weinberg, W. H. University of California, Santa Barbara, unpublished results.

(42) George, P. M.; Avery, N. R.; Weinberg, W. H.; Tebbe, F. N. *J. Am. Chem. Soc.* **1983**, *105*, 1393–1394.

(43) Parmeter, J. E.; Hills, M. M.; Weinberg, W. H. *J. Am. Chem. Soc.* **1986**, *108*, 3563–3569.

(44) Parmeter, J. E.; Schwalke, U.; Weinberg, W. H. *J. Am. Chem. Soc.* **1988**, *110*, 53–62.

be dealt with later as the branching ratio is discussed in section IVB. The complete mode assignments for the mixture of η^1-(C)-HCNH$_2$, μ-CNH$_2$, and NH$_3$ present on the surface at 330 K (and their deuterated isotopes) are given in Table II.

Over the temperature range 330–360 K, shown in Figures 5c–g and 6a, it is apparent that dehydrogenation at the amine group is occurring. Proof of this statement lies in the significant disappearance of the NH$_2$ scissoring deformation at 1545 cm^{-1}, which dominates the spectrum of η^1-(C)-HCNH$_2$ at 330 K in Figure 5c. The presence of a loss feature at 1590–1600 cm^{-1} at 350–360 K coupled with the observed frequency shift to 1255 cm^{-1} upon deuteration at the amine group in Figure 5f,g indicates that an intermediate retaining the amine functional group still remains on the surface at 360 K. Coincident with changes in the NH$_2$ deformation, there appears a very broad and intense loss feature at 720–780 cm^{-1}. This feature was assigned at 330 K to the overlapping δ(CH) and ω(NH$_2$) modes of η^1-(C)-HCNH$_2$ and μ-CNH$_2$, but with the dehydrogenation of most of the amine groups, this very strong feature at 720–780 cm^{-1} is predominantly comprised of a CH bending deformation. A similarly strong CH bending mode is observed at 765 cm^{-1} for molecularly chemisorbed acetylene on Ru(001)[43] in which the carbon atoms are nearly sp^3 hybridized. The loss feature at 1235–1240 cm^{-1} is seen in Figures 5d,e and 6a to maintain its intensity, while that of the δ(NH$_2$) signal attenuates and is assignable to an NH deformation mode. The feature at 1440 cm^{-1} does not shift upon either selective or complete deuteration of the intermediate (cf. Figure 5f,g) and is assigned to the CN stretching mode.

The interpretation consistent with these observed changes in the spectra between 330 and 360 K requires separately addressing the fates of the η^1-(C)-HCNH$_2$ and μ-CNH$_2$ intermediates. Organometallic studies[35b,e,39] have demonstrated that the terminally bound, secondary (dimethylamino)carbene ligand in Os$_3$(CO)$_9$-(HCNMe$_2$)(μ-SPh)(μ-H) readily converts to a bridging (dimethylamino)carbyne ligand, μ-CNMe$_2$, upon either pyrolysis at 475 K or photodecarbonylation of the starting compound. Thus, below 360 K the bridging aminocarbyne, μ-CNH$_2$, is stable, thereby giving rise to the weak, but observed, scissoring deformation of the amine group as well as the CN stretching mode at 1600 cm^{-1}, which is resolved upon deuteration of the methylamine (cf. Figure 5f,g). The marked attenuation of the δ(NH$_2$) feature at 360 K relative to 330 K indicates that the population of bridging aminocarbyne is quite low and that the surface at 330 K is populated predominantly by the terminally bound aminocarbene. While the aminocarbyne undergoes no reaction over this temperature range, η^1-(C)-HCNH$_2$ experiences N–H bond cleavage to yield chemisorbed formimidoyl, HCNH, which dominates the surface at 360 K.

On the Ru(001) surface the formimidoyl intermediate has both the carbon and nitrogen atoms bonded to adjacent Ru atoms with the molecular plane tilted across a surface 3-fold site allowing for coordination to a third surface atom either via π electron density donation to the surface or by surface electron density back donation to the adsorbate's π^* antibonding orbital. This triply bridging configuration involving bonding by both the carbon and nitrogen atoms is designated μ_3-η^2-HCNH. The justification for this tilted coordination comes from the CN stretching frequency lying between that for a single and double bond and the appearance of all four bending modes for the CH and NH in Figure 6a. Were the molecular plane of the intermediate parallel to the surface normal, the in-plane deformations, δ(CH) and δ(NH), at 770 and 1235 cm^{-1} would dominate the spectrum and the out-of-plane deformations, π(CH) and π(NH), at 1015 and 1600 cm^{-1} would be detectable only through impact scattering interactions with the incident electron beam, and their vanishing dipolar derivatives in the direction of the surface normal would render their loss features very weak relative to the in-plane deformations. With the formimidoyl intermediate inclined across the 3-fold surface Ru site, both the in-plane and out-of-plane bending modes of the CH and NH groups are indubitably assigned. The final mode assignment consistent with this coordination of HCNH is the CN stretching mode at 1440–1450 cm^{-1}. As noted earlier, the double

bond CN stretching frequency is 1638 cm^{-1} in methylenimine,[37] H$_2$C=NH, and its bond length is 1.273 Å.[36b] With π donation to or π^* back donation from the surface, the CN bond stretching frequency appears at 1440–1450 cm^{-1}, only slightly shifted from the ν(CN) loss feature at 1420–1430 cm^{-1} of the preceding intermediate, η^1-(C)-HCNH$_2$.

A related organometallic analogue to chemisorbed HCNH is the acetimidoyl ligand in the triiron cluster compound, HFe$_3$(CH$_3$C=NH)(CO)$_9$.[45] The μ_3-η^2-CH$_3$C=NH ligand is triply bridging and has a CN bond length of 1.344 Å and a stretching frequency of 1353 cm^{-1}. This virtually planar ligand has the carbon and nitrogen atoms retaining nearly pure sp^2 hybridization, and, while each is coordinated to adjacent Fe atoms, the ligand tilts approximately 45° across the 3-fold site to allow coordination to the third Fe atom. Yin and Deeming[46] also report a triply bridging acetimidoyl ligand in Os$_3$(μ-H)(CO)$_9$(μ_3-η^2-CH$_3$C=NH). On the W(100)-(1×5)-C surface, HCN is purported to undergo self-hydrogenation upon annealing to 475 K to yield terminally coordinated formimidoyl, η^1-(C)-HCNH; HREELS[47] and NEXAFS[48] experiments have been conducted that indicate CN, CH, and NH stretching modes at 1400, 2940, and 3360 cm^{-1}, yet neither CH nor NH deformation modes are reported. The planar HCNH product with sp^2 hybridization at both the carbon and nitrogen is believed to have its CN bond vector inclined at an angle of $58 \pm 10°$ from the surface normal with only the carbon atom bonded to the surface and the molecular plane perpendicular to the surface.

From the preceding analysis it is known that at 350 K the conversion of the secondary aminocarbene, η^1-(C)-HCNH$_2$, to the bridging formimidoyl, μ_3-η^2-HCNH, is not yet complete and that bridging aminocarbyne, μ-CNH$_2$, is also present. When saturated coverages of CH$_3$ND$_2$ and CD$_3$ND$_2$ are annealed to 350 K, the spectra of Figure 5f,g are obtained and must be interpreted as mixtures of their respective deuterated aminocarbyne, secondary aminocarbene, and formimidoyl intermediates. Upon deuteration the δ(ND$_2$), ρ(ND$_2$), and ω(ND$_2$) appear respectively at 1255, 755, and 580 cm^{-1}, while the δ(ND) and π(ND) modes appear at 1010 and 1255 cm^{-1}. The deformation δ(CD) and π(CD) modes appear at 585 and 715 cm^{-1}, and, of course, the CN bond frequency does not shift noticeably upon deuteration and appears at 1425–1435 cm^{-1}. The complete mode assignments for these chemisorbed species and their deuterated isotopes are provided in Table III.

Annealing between 370 and 390 K induces the changes in the spectra of Figure 6b–d, indicating that both intermediates present at 360 K, μ_3-η^2-HCNH and μ-CNH$_2$, have undergone dehydrogenation reactions. The very strong δ(CH) mode at 720–780 cm^{-1} is gone from the spectrum at 390 K, and, as it attenuates, a very intense feature at 595–605 cm^{-1} appears. The δ(NH) mode at 1260–1280 cm^{-1} retains its intensity, and by 380 K a resolvable feature at 1665 cm^{-1}, characteristic of a CN double bond, appears. The feature at 1590–1600 cm^{-1}, assigned to the NH$_2$ scissoring deformation of the low-coverage intermediate, μ-CNH$_2$, is lost upon annealing to 370 K.

The surface intermediate formed by 380 K and appearing to be stable to 390 K is chemisorbed hydrogen isocyanide, HNC. There are two possible bonding configurations for HNC, and the analogous system of methylisocyanide, CH$_3$NC, adsorbed on Pt(111) has been thoroughly investigated by Avery and Matheson.[49] Terminal, linear bound CH$_3$NC revealed a very strong CN stretching frequency of 2240–2265 cm^{-1}, accompanied by a similar strong Pt–C stretch at 385 cm^{-1}. The terminally bound methylisocyanide coexisted at higher coverages with a bridge-

(45) (a) Andrews, M. A.; Kaesz, H. D. *J. Am. Chem. Soc.* **1979**, *101*, 7238–7244. (b) Andrews, M. A.; van Buskirk, G.; Knobler, C. B.; Kaesz, H. D. *J. Am. Chem. Soc.* **1979**, *101*, 7245–7254.
(46) Yin, C. C.; Deeming, A. J. *J. Organomet. Chem.* **1977**, *133*, 123–138.
(47) Serafin, J. G.; Friend, C. M. *J. Phys. Chem.* **1988**, *92*, 6694–6700.
(48) Stevens, P. A.; Madix, R. J.; Friend, C. M. *Surf. Sci.* **1988**, *205*, 187–206.
(49) (a) Avery, N. R.; Matheson, T. W. *Surf. Sci.* **1984**, *143*, 110–124. (b) Avery, N. R.; Matheson, T. W.; Sexton, B. A. *Appl. Surf. Sci.* **1985**, *22/23*, 384–391.

Table III. Vibrational Frequencies (cm^{-1}) and Mode Assignments of Triply Bridging Formimidoyl, μ_3-η^2-HCNH, Bridging and Terminally Bound Hydrogen Isocyano, μ-CNH and η^1-(C)-CNH, and Triply Bridging Cyano, μ_3-η^2-CN[a]

| | formimidoyl, 335–370 K | | | hydrogen isocyano, 370–390 K[b] | | cyano, 400–450 K |
mode	HCNH	HCND	DCND	μ-CNH	η^1-CNH	μ^3-η^2-CN
ν(NH) or ν(ND)	3250	2450	2450			
ν(CH) or ν(CD)	2920	2920	2200			
ν(CN)	1450	1450	1450	1660	2280	1670
π(NH) or π(ND)	1450	1220	1220	1450		
δ(NH) or δ(ND)	1240	1000	1000	1280	1060	
π(CH) or π(CD)	950	950	720			
δ(CH) or δ(CD)	770	770	550			
ν_a(Ru–CN)						465
ν_s(Ru–CN)						355
ν(Ru–C)				600	350	

[a] Indicated temperatures in the column headings correspond to the ranges in which each intermediate populates the surface and influences the high-resolution EEL spectra; refer to text and figures. [b] The first overtone of the strong symmetric stretch, ν(Ru–C), combines with the bending deformation, δ(NH), of the bridge-bonded μ-CNH adsorbate to yield a loss feature at 2450 cm^{-1} in Figure 6b–d.

bound imine-like configuration with a characteristic CN double bond stretching frequency that increased with coverage over the range of 1690–1770 cm^{-1}. Very strong Pt–C frustrated translation and skeletal deformation modes were observed at 265 and 530 cm^{-1} for this second bridge-bonded imine-like configuration.

With this information the hydrogen isocyanide intermediate present on the Ru(001) surface at 380–390 K is observed to exist as a mixture of terminally bound, η^1-(C)-CNH, and bridge-bound, μ-CNH. The mode assignments for the two configurations are given in Table III with the CN stretching frequencies at 2275–2295 and 1660–1670 cm^{-1}, respectively, for the terminally bound and bridge bound HNC intermediates. The NH bending deformations are at 1090 cm^{-1} for η^1-(C)-CNH and at 1260–1280 cm^{-1} for μ-CNH. For comparison the NH bending deformation is at 1344 cm^{-1} for gas-phase methylenimine.[37] The very strong loss feature at 595–605 cm^{-1} is assigned to the frustrated translation of the bridge bound hydrogen isocyanide, ν(Ru–C). The appearance of CO on the surface is evidenced by ν(CO) at 2000 cm^{-1}. The amount of CO is quite small, however. The loss feature at 2400–2450 cm^{-1} in Figure 6c,d is puzzling. Its assignment as a combination band of ν(Ru–C) and ν(CO) for the background-adsorbed carbon monoxide is not reasonable since the feature at 2450 cm^{-1} is comparable in intensity to the ν(CO) loss feature itself. The strongest feature is the 595–605 cm^{-1} frustrated translation of the bridging HNC intermediate, and the second strongest loss feature at 1260 cm^{-1} is the bending deformation, δ(NH), of this same intermediate. With both these modes having strong perpendicular dynamic dipole moments for the bridging imine-like configuration, the loss feature at 2400–2450 cm^{-1} is tentatively assigned as the combination of the first overtone of ν(Ru–C) with δ(NH).

Annealing the crystal to 400 K causes dehydrogenation of this remaining NH bond and the conversion to side-on bonded cyano, CN. Parts e–g of Figure 6 correspond to saturation exposures of CH$_3$NH$_2$, CH$_3$ND$_2$, and CD$_3$ND$_2$ adsorbed at 80 K and annealed to 400–425 K. All three isotopes yield identical spectra showing Ru–CN symmetric and asymmetric stretching modes at 340–350 and 585–595 cm^{-1} and ν(CN) stretching modes at 1655–1665 cm^{-1}. The presence of CO present on the surface is noted by the loss features at 450 and 2000 cm^{-1}. Annealing above 425 K desorbs the small amount of CO present on the surface, removing the ν(CO) feature at 2000 cm^{-1} and attenuating that at 450 cm^{-1}. By 450 K thermal decomposition of side-on bonded cyano begins accompanied by an increase in the intensity of the loss feature at 585–595 cm^{-1}. At 600 K no cyano adspecies remains on the surface, as evidenced by the loss of ν(CN), and annealing above 800–900 K initiates recombinative desorption of dinitrogen, decreasing the intensity of the 585–595 cm^{-1} feature but never entirely eliminating it. Thus, the loss feature at 585–595 cm^{-1} present in HREEL spectra above 450 K is due to ν(Ru–C) and ν(Ru–N) of surface carbon and nitrogen adatoms overlapping with the asymmetric ν(Ru–CN) mode of surface cyano present between 400 and 600 K.

Other surface HREELS studies have isolated chemisorbed CN on Pd(111) and Pd(100)[50] and on Cu(111) and O-predosed Cu-(111).[51] On both Pd(111) and Pd(100) surfaces, ν(CN) is observed at 220–240 meV (1774–1935 cm^{-1}). On clean Cu(111) ν(CN) is at 2045 cm^{-1}, and on O-predosed Cu(111) it is blue shifted to 2140 cm^{-1}. On Pd(111) and Pd(100) the cyano adspecies is proposed to be side-on bonded with the CN bond vector parallel to the surface. A NEXAFS study[52] of CN/Pd(111) revealed the CN bond axis to be tilted 14° above the plane of the surface, but the authors believe the cyano to be exactly parallel with the 14° tilt resulting from the experimental uncertainty inherent in the measurement. On the Cu(111) surfaces, CN is believed to exist in a side-on bonded configuration on the clean surface, but, when adsorbed onto an O-precovered surface, it reorients to a vertical, terminally bound configuration. This argument is used to explain the observed blue shift and intensification of the loss feature at 2140 cm^{-1} for CN/O–Cu(111) relative to the feature at 2045 cm^{-1} for CN/Cu(111). In our view, this increase in frequency for ν(CN) can more reasonably be explained as resulting from preadsorbed oxygen-withdrawing electron density from the surface and thereby decreasing the extent of back donation to the terminally coordinated CN. On the clean Cu(111) surface the ν(CN) loss feature at 2045 cm^{-1} is too high to be consistent with a side-on bonded configuration but rather reflects a terminally coordinated cyano adspecies bound to the surface predominantly by back donated electron density from the electron-rich, late-transition metallic Cu surface.

As expressed in an earlier publication,[53] the bonding configuration of CN on Ru(001) is best described as μ_3-η^2-CN. Both the carbon and nitrogen atoms interact with the surface: The carbon atom is σ-bonded to a single surface Ru atom while the CN bond vector is inclined across the center of a surface 3-fold site, thereby allowing either the bonding 1π orbitals to donate electron density to the surface or the antibonding 2π orbitals to receive back donated density from the surface. The 4σ lone pair orbital on the nitrogen atom remains collinear with the CN bond vector and thus stays orthogonal to the bonding orbitals between the surface and the cyano adspecies. This μ_3-η^2-CN configuration affords the greatest degree of overlap of surface and adsorbate orbitals and hence is preferred over alternative configurations.

(50) (a) Kordesch, M. E.; Stenzel, W.; Conrad, H. *J. Electron Spectrosc. Relat. Phenom.* **1986**, *39*, 89–96. (b) Kordesch, M. E.; Stenzel, W.; Conrad, H. *Surf. Sci.* **1986**, *175*, L687–L692.

(51) (a) Kordesch, M. E.; Stenzel, W.; Conrad, H.; Weaver, M. *J. Am. Chem. Soc.* **1987**, *109*, 1878–1879. (b) Kordesch, M. E.; Feng, W.; Stenzel, W.; Weaver, M.; Conrad, H. *J. Electron Spectrosc. Relat. Phenom.* **1987**, *44*, 149–162. (c) Feng, W.; Stenzel, W.; Conrad, H.; Kordesch, M. E. *Surf. Sci.* **1989**, *211/212*, 1044–1052.

(52) Somers, J.; Kordesch, M. E.; Linder, Th.; Conrad, H.; Bradshaw, A. M.; Williams, G. P. *Surf. Sci.* **1987**, *188*, L693–L700.

(53) Weinberg, W. H.; Johnson, D. F.; Wang, Y.; Parmeter, J. E.; Hills, M. M. *Surf. Sci. Lett.* **1990**, *235*, L299–L302.

IV. Discussion

The data presented in the previous section allow several important statements to be made regarding the decomposition of methylamine on Ru(001). The demonstrated preference for cleavage of C–H bonds over N–H and C–N bonds is evident from both the thermal desorption and high-resolution EEL spectra, and a comparison of this behavior to that observed for other surface reactions is now possible. Through careful accounting of the ammonia produced from the decomposition of CH_3ND_2, quantification of the branching ratio can be made for the competing dehydrogenation and C–N bond cleavage reaction pathways. Finally, the relevance of this study to commercial disproportionation reactions of aliphatic amines can be discussed.

A. Comparison of CH_3NH_2/Ru(001) to Related Surface Science Studies. The interactions of methylamine on Pt(111), Rh(111), Ni(111), W(100), W(100)–(1×5)–C and W(100)–(1×2)–O, Mo(100), Ni(100), Cr(100), Cr(111), and Pt(100) surfaces have been reported. On Pt(111)[10,11] temperature programmed desorption, TPD, and Auger electron spectroscopy, AES, indicate that no C–N bond cleavage occurs, and dehydrogenation is the only decomposition pathway available to CH_3NH_2. For room temperature exposures only H_2, HCN, and C_2N_2 are observed as decomposition products, and for exposure at 100 K in addition to the above products molecular methylamine also is observed. On Rh(111)[11,12] the decomposition of CH_3NH_2 yields H_2, HCN, and C_2N_2 as it did on Pt(111) except that at ~850 K cyanogen desorption ceases and N_2 desorption is observed. Thus, on Rh(111) there is evidence of C–N bond cleavage seemingly well after methylamine has been completely dehydrogenated to leave surface cyano, CN. High-resolution EELS experiments following the progress of the reaction would certainly help identify the occurrence of any low temperature cleavage of the C–N bond. In contrast, TPD and AES studies of methylamine adsorbed at 87 K on Ni(111)[16] indicate that molecular methylamine, H_2, and N_2 desorb as gas-phase products with surface carbon deposited as all irreversibly adsorbed methylamine experiences complete dissociation of the C–N bond. By approximately 430 K all the H_2 has desorbed, and an Auger line shape analysis indicates that near 410 K carbidic and nitridic species are being formed from C–N bond cleavage of the surface cyano. By study of the H_2 and D_2 thermal desorption spectra from the deuterated isotopes, CD_3NH_2 and CH_3ND_2, it was determined unequivocally that when adsorbed at 412 K, some, if not both, N–H bonds are retained while all the C–H bonds have been cleaved. On W(100) and the carbon and oxygen precovered W(100) surfaces,[14] CH_3NH_2 adsorbed at 120 K undergoes competing molecular desorption and complete decomposition to H_2, N_2, and surface carbon. The carbon precovered surface affected the reaction only by stabilizing the molecular methylamine to higher temperatures, and the oxygen precovered surface oxidized the surface carbon to yield gaseous CO as a product. On Mo(100),[13] thermal decomposition of monomethylamine following room temperature adsorption yields H_2, N_2, HCN, and a small amount of CH_4. No intact molecular CH_3NH_2 is observed, and the HCN product desorbs between 400 and 500 K. High-resolution electron energy loss spectroscopy studies of CH_3NH_2 adsorbed at 300 K on the Ni(111), Ni(100), Cr(111), and Cr(100) surfaces[15] indicate that molecular CH_3NH_2 exists on all surfaces with bonding through the lone pair of electrons on the nitrogen atom. On the Cr surfaces a substantial amount of dissociation is purported to occur based upon the appearance of a very intense, sharp loss feature at 510 cm^{-1} on Cr(100) and an intense, but broad, feature also at 510 cm^{-1} on Cr(111). This loss feature correlates with the surface–adsorbate stretching modes observed here on Ru(001) for the intermediate H_2CNH_2. Temperature programmed reaction spectrometry results of methylamine's decomposition on Ni(100)[17] are remarkably similar to those observed in this study. Molecular methylamine, hydrogen, nitrogen, and ammonia are the observed gaseous products with surface carbon observed with postreaction Auger spectroscopy. The ammonia is seen to have a peak desorption temperature of 365 K, while hydrogen peaks at approximately 375 K. The decomposition of CH_3ND_2 was also examined and

showed the ammonia product made up of primarily ND_2H and ND_3, and the H_2 and D_2 desorption spectra had peaks at 370 and 385 K, respectively. On Pt(100)–(5×20) and Pt(100)–(1×1),[18] methylamine's interaction and decomposition were studied. The Pt(100)–(5×20) surface is a stable, pseudohexagonal surface similar to Pt(111), and thermal desorption and high-resolution EELS data indicate that only reversible desorption occurs for methylamine. On metastable Pt(100)–(1×1), however, decomposition is evident from the gas-phase TDS detection of H_2 (T_{pk} ~ 380 K), HCN (550 K), C_2N_2 (780 K), and N_2 (810 K). The appearance of a HREELS loss feature at 1140 cm^{-1} upon annealing to 410 K is assigned to the C–C stretching mode of chemisorbed cyanogen implying completely dehydrogenated cyano, CN, adspecies have dimerized on the surface. Such an assignment must be considered tentative since the HREEL spectrum at 550 K contains evidence of a C–H stretching mode at 2980 cm^{-1}, implying that the 1140-cm^{-1} feature might also arise from a hydrogenic deformation mode of an incompletely dehydrogenated surface intermediate such as HCN.

In addition to the single crystalline studies, the reaction of CH_3NH_2 with H_2 has been examined on other kinds of transition-metal surfaces. Kemball and Moss[54] have studied this reaction over polycrystalline Ni, Fe, Pd, Pt, and W films, while Anderson and Clark[55] examined it over evaporated Pt, Pd, Ni, W, Co, V, and Cu films. The cracking of CH_3NH_2 to CH_4 and NH_3 and disproportionation to di- and trimethylamines were the dominant reaction processes observed. Meitzner et al.[56] studied the reaction over silica-supported Ru, Rh, Re, Pd, Os, Ir, Pt, and Au catalysts and found that cracking to CH_4 and NH_3 occurred on all metals as did a significant amount of disproportionation to dimethylamine, except on Rh. Minor products were found to be produced from the various metals, and most notably Ru and Os converted one-third of the methylamine to acetonitrile. Orita et al.[57] studied the decomposition of CH_3NH_2 at 393 K over Ru black in both the presence and absence of H_2. Of particular relevance is the fact that no higher amines were observed and small amounts of C_2–C_4 hydrocarbons were formed along with the CH_4 and NH_3 cracking products.

A comparison of the interactions of ammonia and methylamine with the Ru(001) surface is of pedagogic interest. The thermal desorption of reversibly adsorbed methylamine, as seen in Figure 1a, contains the same qualitative features as ammonia desorption from clean Ru(001). The desorption temperatures for methylamine are approximately 15 K greater than those of ammonia, and this observation is readily understandable based on the greater Lewis base character of methylamine and noting that both adsorbates bond to the Ru(001) surface via nitrogen lone pair donation. The formation of a second layer of ammonia on Ru(001) gives rise to a resolvable desorption feature at 140 K[22] and a strong librational loss feature at 360 cm^{-1} in HREEL spectra.[23] Methylamine thermal desorption spectra do not reveal a second-layer feature resolved from that of a multilayer of CH_3NH_2. However, the strong librational mode associated with the second layer is readily observed after annealing off the multilayer (cf. Figure 3a–c). Thus, the bonding interactions of ammonia and molecular methylamine are predictably similar with the presence of the methyl group slightly modifying the strengths of the bond to the surface.

B. Branching Ratio: Competing Decomposition Pathways of CH_3NH_2. The majority decomposition pathway available to irreversibly adsorbed methylamine is complete dehydrogenation to chemisorbed cyano, CN. A smaller fraction of methylamine will follow the minority path of carbon–nitrogen bond cleavage, forming the ultimate products of carbon and nitrogen adatoms and ammonia. The production of ammonia occurs subsequent

(54) Kemball, C.; Moss, R. C. *Proc. R. Soc. London, A* **1957**, *238*, 107–116.
(55) Anderson, J. R.; Clark, N. J. *J. Catal.* **1966**, *5*, 250–263.
(56) Meitzner, G.; Myktka, W. J.; Sinfelt, J. H. *J. Catal.* **1986**, *98*, 513–521.
(57) Orita, H.; Naito, S.; Onishi, T.; Tamaru, K. *Bull. Chem. Soc. Jpn.* **1983**, *56*, 3390–3392.

to this C–N bond cleavage step and provides the means for quantifying the branching ratio of the competing decomposition reactions.

The surface reaction that forms ammonia results from amido, NH_2, combining with surface hydrogen. This statement is made based on the observation that for the low coverages of surface hydrogen encountered in this reaction, it is not at all likely that nitrogen adatoms or even imidogen, NH, could be reduced to form ammonia.[24] Thus, the production of ammonia follows the cleavage of the carbon–nitrogen bond in a surface intermediate that has retained the integrity of the amine functional group.

The intermediate which precedes C–N bond cleavage is bridging methyleniminium, μ-η^2-H_2CNH_2, present and stable on the surface at 300 K. The CN bond lengths in two separate triosmium cluster compounds[32] were found to be 1.53 and 1.50 Å, which are elongated relative to the CN single bond length of 1.47 Å.[36a] Heating one of these compounds, $Os_3(CO)_{10}(\mu$-η^2-$H_2CNMe_2)(\mu$-H), to 370 K induces cleavage of a C–H bond to yield a triply-bridging, secondary aminocarbene, μ_3-η^2-$HCNMe_2$, with a C–N bond length of 1.40 Å. The triple-bridging coordination of secondary (dimethylamino)carbene is less favored than its terminally coordinated isomer, η^1-(C)-$HCNMe_2$, which is encountered in numerous other organometallic compounds.[35]

In the decomposition of methylamine on Ru(001), a definitive isolation and identification of μ_3-η^2-$HCNH_2$ has not been made. Mode assignments for such an intermediate would have to include the stretching modes of the Ru–CN framework, which presumably would lie between 500 and 600 cm^{-1}, together with a C–N single bond stretching mode near 1000 cm^{-1} and a C–H deformation mode near 750 cm^{-1}. Such assignments may be possible for the spectra between 310 and 320 K, but the preference of $HCNH_2$ to be sp^2 hybridized and terminally coordinated has been demonstrated, and it is for this reason that triple-bridging secondary aminocarbene is not unambiguously isolated.

The competition between C–H and C–N bond cleavage in methyleniminium begins upon annealing above 300 K and appears to be completed by 320–330 K. The majority pathway continues, after C–H bond cleavage yields $HCNH_2$, and it follows the sequence presented earlier in the interpretation of the HREEL spectra. The minority pathway is initiated by C–N bond cleavage in μ-η^2-H_2CNH_2, leading to the formation of surface methylene, CH_2, and amido, NH_2. As noted previously, both of these intermediates are unstable under these conditions and will quickly convert to further products.

Quantification of the branching ratio is made dependent upon the extent to which the surface amido, NH_2, *itself branches to form imidogen and surface hydrogen or is hydrogenated to form ammonia.* The key input in addressing this issue lies in the ammonia *thermal desorption data and especially that of the mixed deuterated isotopes* of ammonia formed from the decomposition of CH_3ND_2 (cf. Figure 2b). The hydrogenation reaction of surface amido involves the transfer of a hydrogen (or deuterium) atom from some surface state (not necessarily a ground state) to the short-lived amido intermediate before the amido itself decomposes. From the thermal desorption spectra of the deuterated ammonia product in Figure 2b, and assuming equal mass spectrometric sensitivities for the parent ND_3 and ND_2H molecules, the amount of ND_2H formed is 40% of that of ND_3, or 28% of the total ammonia, ND_3 + ND_2H. Together these two ammonia products account for the observed cracking fragments at masses 17 and 18. The production of ND_3 *must* occur from the deuteration of ND_2, where the deuterium adatom has been formed from the decomposition of a second deuterated amido. This surface deuterium is most likely in a highly mobile surface state where it possesses most of the energy from the decomposition reaction of the unstable ND_2. Upon locating an intact, unstable, but newly formed ND_2, it deuterates this amido and yields the more stable ND_3 product.

The production of ND_2H obviously results from the reaction of ND_2 with the available surface hydrogen adatoms. It is interesting to note that despite the fact that there is significantly higher coverage of surface H than surface D, the fact remains

that 72% of the ammonia product is ND_3 while only 28% is ND_2H. This experimental result is simply a manifestation of the difference in relative reaction rates of the deuterated amido, ND_2, with highly mobile D atoms versus thermally equilibrated, less mobile H atoms. The higher reactivity of similarly "hot" hydrogen adatoms has been observed recently in the decomposition of formates on the Ru(001) surface.[58]

The fate of the mobile surface deuterium is not exclusively to react with surface ND_2, but it might also combine with surface hydrogen adatoms and desorb as HD. As seen in Figure 2a, the beginning of HD desorption occurs near 320 K, while that of D_2 is not seen until near 365 K. The preponderance of both the HD and D_2 thermal desorption results from later decomposition of majority path intermediates: η^1-(C)-$HCND_2$, μ-η^2-$HCND$, μ-CND, and η^1-(C)-CND. The low-temperature tail of the mass 3 amu signal, however, contains H recombination with D released from ND_2 decomposition from the minority path. Thus, a definitive determination of the branching ratio must include the ultimate products of all the surface amido formed when the C–N bonds are cleaved.

For each ND_3 molecule formed, two amido intermediates have to participate, since one of these must decompose in order to release the deuterium atom required to make ND_3. The total ammonia produced from a saturation exposure of CH_3NH_2 was given earlier as 0.02 ± 0.01 monolayer while that of irreversibly adsorbed methylamine was 0.15 ± 0.01 monolayer. With 72% of ammonia formed from CH_3ND_2 being ND_3 and 28% being ND_2H, the most efficient production of ammonia following C–N bond cleavage leads to an estimate of 0.034 monolayer for the fractional coverage of methylamine that follows the minority reaction. In terms of the branching ratio, this result implies that 23%, or one in every four or five, of the irreversibly adsorbed methylamine molecules undergoes C–N bond scission.

As noted above, however, the low temperature tail, 320 K < T < 350 K, of the HD desorption spectrum arises from deuterium and hydrogen recombination, where the deuterium source is the decomposing amido, ND_2. The amount of HD present in the leading edge is estimated to be less than 25% of the total HD produced, and the total fractional coverages of HD and this atomic D in Figure 2a are 0.25 and 0.06 monolayer, respectively, both relative to saturation coverages of atomic deuterium, Θ_D = 1.00. The estimate of the maximum amount of amido decomposition that appears as HD is 0.031 monolayer. Combining this with the amount of hydrogenated amido that forms ND_3 yields an estimate of 0.065 for the maximum fractional coverage of methylamine experiencing C–N bond cleavage. In this case the distinction between minority and majority paths is virtually meaningless since 44%, or nearly one of each two molecules, completely dehydrogenates, while the other cleaves its CN bond.

It must be noted, however, that when the C–N bond of methyleniminium is broken, a methylidyne, CH, and hydrogen adatom will be formed upon the decomposition of surface methylene. Methylidyne is stable on Ru(001) to above 500 K and its bending deformation mode, δ(CH), at 800 cm^{-1} is a strong loss feature.[43] The fact that no such HREEL assignment can be made for methylidyne in the spectra from methylamine's decomposition implies that the fractional coverage of methylidyne must be below its detection limit by the HREEL spectrometer. With this in mind, the extent of C–N bond cleavage along the minority pathway is most likely near the lower limits of the above estimates, i.e., between 0.04 and 0.05 monolayer, yielding a branching ratio between one of every three to four irreversibly adsorbed molecules. Scheme I incorporates the principal products of the sequence of elementary reaction steps along the majority and minority paths.

C. η^1-(C)-$HCNH_2$ and the Disproportionation of Amines. Some of the intermediates identified in the decomposition of methylamine on Ru(001) are of general interest because they may play relevant roles in related catalytic processes. For example, the catalytic amination of aliphatic alcohols by copper oxide produces aliphatic amines that are commercially used as corrosion inhibitors and as

(58) Sun, Y.-K.; Weinberg, W. H. *J. Chem. Phys.* **1991**, *94*, 4587–4599.
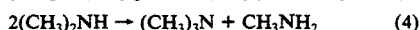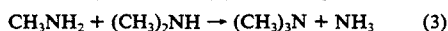
Scheme I

Scheme II

Scheme III
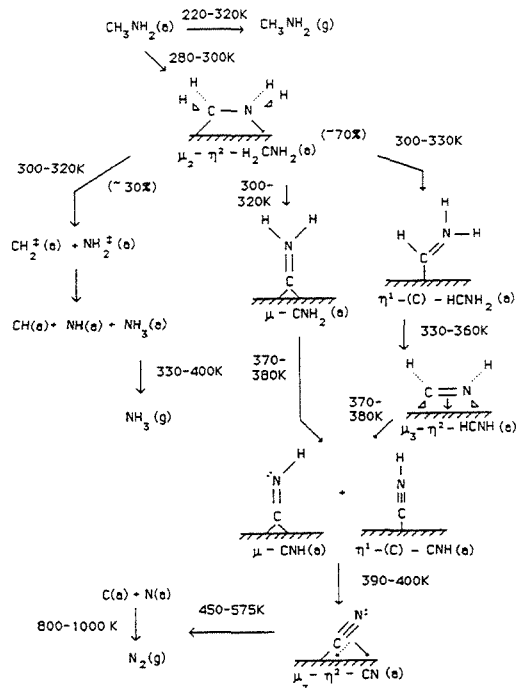
additives to textile products.[3] The process uses either dimethylamine or monomethylamine reacting with long chain primary alcohols to yield the desired amine product and water as in reaction 1. The mechanism has been studied by Baiker et
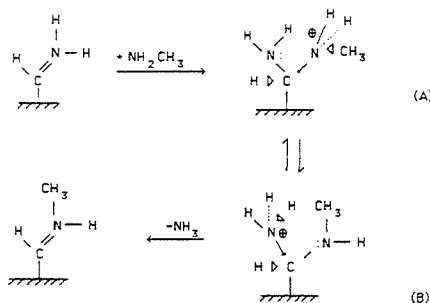
$$RCH_2OH + (CH_3)_2NH \rightarrow RCH_2N(CH_3)_2 + H_2O \quad (1)$$
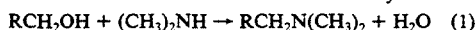
al.[2] and it is believed to involve the aldehyde of the reagent alcohol. The selectivity of the reaction is hampered however by disproportionation (reactions 2–4) of the reagent dimethyl- or monomethylamine.[55] At the temperature range of the amination

$$2CH_3NH_2 \rightarrow (CH_3)_2NH + NH_3 \quad (2)$$

$$CH_3NH_2 + (CH_3)_2NH \rightarrow (CH_3)_3N + NH_3 \quad (3)$$

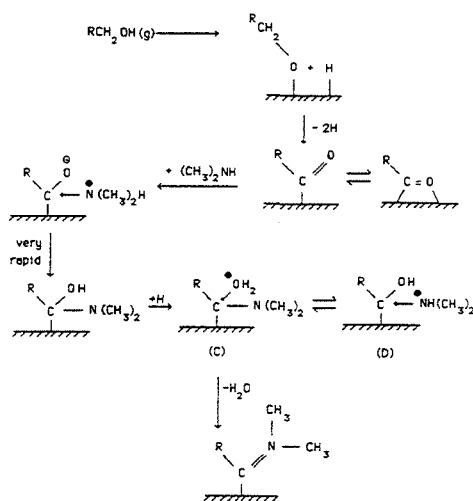$$2(CH_3)_2NH \rightarrow (CH_3)_3N + CH_3NH_2 \quad (4)$$

process, 400–600 K, the equilibrium mixture consists predominantly of ammonia and trimethylamine. To improve the selectivity of the process, it was discovered that a hydrogen partial pressure of 15–80 kPa in the reaction stream inhibited disproportionation of the feed amine.

In the decomposition of methylamine on Ru(001), the identification of terminally bound, secondary aminocarbene has been made. This planar intermediate has a partial double bond between the carbon and nitrogen, in part due to the incomplete delocalization of the nitrogen lone pair to the empty p_π orbital of the carbon atom. As a result, the carbenoid carbon of η^1-(C)-HCNH$_2$ is electron deficient and susceptible to nucleophilic attack, a chemical property common to metal-coordinated amino carbene ligands.[59] A mechanism for the transalkylation of tertiary amines has been proposed for the (dimethylamino)carbene ligand in Os$_3$(CO)$_8$ (η^1-HCNMe$_2$)(μ-H)$_2$(μ_3-S) by Adams et al. which involves equilibration between two zwitterionic intermediates.[9] This mechanistic step is illustrated in Scheme II to demonstrate the disproportionation of monomethylamine. The sequence begins with η^1-(C)-HCNH$_2$ experiencing nucleophilic attack at its

(59) (a) Connor, J. A.; Fischer, E. O. *J. Chem. Soc. A* **1969**, 578–584. (b) McCormick, F. B.; Angelici, R. J. *Inorg. Chem.* **1981**, *20*, 1118–1123.

carbenoid carbon by a second monomethylamine molecule. The cationic pair (A and B) are formed by the intramolecular transfer of a proton between the two amine moieties. The new secondary methylaminocarbene then can be reduced by surface hydrogen to form dimethylamine, (CH$_3$)$_2$NH.

Related to this reaction mechanism is the amination step of long chain aliphatic alcohols. When α-deuterium labeled alcohols, RCD$_2$OH, were aminated by dimethylamine, the product mixture contained 33% RCDHN(CH$_3$)$_2$ and 67% RCH$_2$N(CH$_3$)$_2$, but no RCD$_2$N(CH$_3$)$_2$.[22] These results indicate that at least one α-CD bond is cleaved during the amination reaction. A mechanism involving an intermediate analogous to η^1-(C)-HCNH$_2$ is proposed in Scheme III to account for the majority product. The aliphatic alcohol will undergo initial O–H bond cleavage on the surface followed by the cleavage of both of the α-CH bonds to yield an intermediate with an electron-deficient carbonyl carbon. This carbon atom is then attacked by the nucleophilic amine, followed by a very rapid intramolecular proton transfer. Protonation from the surface produces the cationic pair (C and D) with water ultimately released as a leaving group upon C–O bond cleavage. The resulting surface intermediate is the secondary (dimethylamino)carbene, which, when reduced by surface hydrogen, yields the desired aliphatic long-chain amine.

V. Summary

A high-resolution electron energy loss spectroscopy and thermal desorption mass spectrometry study of monomethylamine on the clean surface of Ru(001) has been performed, and the important findings are the following:

1. Molecular methylamine coordinates to this surface through lone pair donation of the nitrogen atom, and its interaction is of

the same nature as that of ammonia with only a slightly stronger bond formed as a result of the substituent methyl group.

2. Preferential dehydrogenation is observed relative to C–N bond cleavage. Approximately ~70% of the irreversibly adsorbed methylamine dehydrogenates completely to surface cyano, μ_3-η^2-CN, with ν(CN) = 1660 cm^{-1}.

3. Activation of C–H bonds is more facile than that of N–H bonds, as judged by the isolation of η^1-(C)-HCNH$_2$ and μ-CNH$_2$ intermediates.

4. No desorption products other than reversibly adsorbed methylamine are observed to retain the CN bond, and the surface cyano is stable to 450 K at which point it begins to decompose to carbon and nitrogen adatoms.

5. A mechanism for amine disproportionation and amination of aliphatic alcohols is proposed that involves the secondary aminocarbene, η^1-(C)-HCNH$_2$, stable on this surface under these ultrahigh vacuum conditions between 300 and 330 K.

Hydrogenation of CO at 100 K on the Ru(001) Surface: Spectroscopic Identification of Formyl Intermediates

William J. Mitchell, Youqi Wang, Jun Xie, and W. Henry Weinberg*

Department of Chemical and Nuclear Engineering University of California, Santa Barbara, California 93106

An improved understanding of Fischer–Tropsch synthesis and the methanation reaction involving the catalytic reaction of CO and H_2 on transition metals to form hydrocarbons (CO bond scission) and alcohols (CO bond preserved) is of obvious industrial importance. As a result, this reaction has been studied intensely over numerous transition metals and over a wide range of temperatures and pressures. Under ultrahigh-vacuum (UHV) conditions (base pressure below 10^{-10} Torr and working pressure below 10^{-7} Torr), no reaction between CO and H_2 has been observed on single-crystalline metal surfaces. Consequently, UHV studies have been restricted to analyzing coadsorption phenomena where it is found that the CO–H interaction is repulsive, with this repulsion decreasing as one proceeds from the close-packed [fcc(111), hcp(001)] to the more open [fcc(110), bcc(100)] crystallographic orientations.[1] High-pressure studies (order of 10–100 Torr), however, have revealed a steady-state reaction between coadsorbed CO and hydrogen to produce methane (and some higher alkanes) on Ru, Ni, Pt, Pd, Ir, and Fe.[2-4] These studies show the reaction rate to be structure insensitive (i.e., independent of crystallographic orientation), and of the metals investigated, Ru was found to exhibit the highest activity. Using *ex situ* characterization of the surface, a mechanism was proposed that is based on the initial dissociation of CO, followed by hydrogenation of the surface carbon to CH_4.[2,5] However, CO chemisorbs *molecularly* on Ru, Pt, Pd, and Ir, and it is difficult to activate on these as well as on all other late transition metals. Thus, it is feasible that insertion of hydrogen into the Ru–CO bond, or vice versa, to form a H_xCO intermediate may occur,[4] a possibility supported in the organometallic literature (ref 6 and references therein). This intermediate can then dehydrate under reaction conditions to give hydrocarbons, or it can hydrogenate further to give alcohols. The initial steps involved in the hydrogenation reaction have not yet been identified, and *in situ* spectroscopy on this *reaction* system must be carried out.

We have hydrogenated CO on a single-crystalline surface, under UHV conditions, which has allowed us to perform high-resolution electron energy loss spectroscopy (HREELS) to determine unambiguously the initial surface reaction intermediates. The
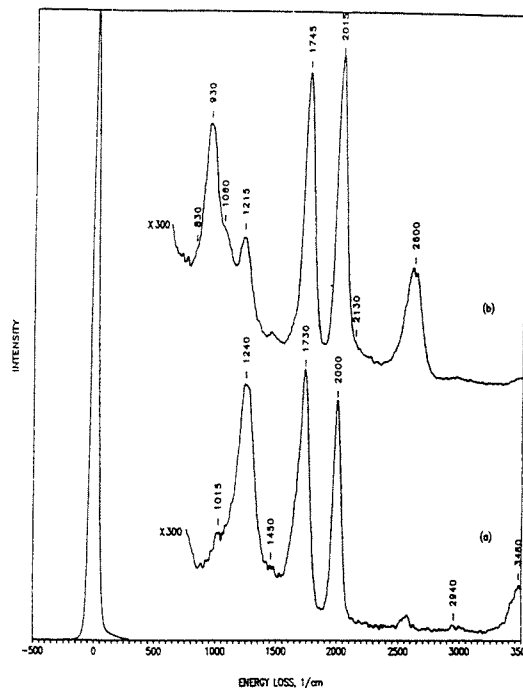
(1) (a) Channing, N. D. S; Chesters, M. A. *Surf. Sci.* **1986**, *175*, L811. (b) Benziger, J.; Madix, R. *Surf. Sci.* **1978**, *77*, L379. (c) Rangelov, G.; Bischler, U.; Memmel, N.; Bartel, E.; Dose, V.; Pabst, M.; Rosch, N. *Surf. Sci.* **1992**, *273*, 61. (d) Conrad, H.; Ertl, G.; Latta, E. E. *J. Catal.* **1974**, *35*, 363. (e) Fisher, J. B.; Madey, T. E.; Yates, J. T. *J. Vac. Sci. Technol.* **1978**, *15*, 543. (f) Ibbotson, D. E.; Wittrig, T. S.; Weinberg, W. H. *Surf. Sci.* **1981**, *111*, 149. (g) Goodman, D. W.; Yates, J. T.; Madey, T. E. *Surf. Sci.* **1980**, *93*, L135. (h) Richter, L. J.; Germer, T. A.; Ho, W. *J. Chem. Phys.* **1987**, *86*, 477. (i) Nyberg, C.; Westerlund, L. *Surf. Sci.* **1991**, *256*, 9. (j) Yates, J. T.; Madey, T. E. *J. Chem. Phys.* **1971**, *54*, 4969.

(2) (a) Krebs, H. J.; Bonzel, H. P.; Gafner, G. *Surf. Sci.* **1979**, *88*, 269. (b) Bonzel, H. P.; Krebs, H. J. *Surf. Sci.* **1980**, *91*, 499. (c) Goodman, D. W.; Kelley, R. D.; Madey, T. E.; Yates, J. T. *J. Catal.* **1980**, *63*, 226. (d) Kelley, R. D.; Goodman, D. W. *Surf. Sci.* **1982**, *123*, L743. (e) Krebs, H. J.; Bonzel, H. P. *Surf. Sci.* **1980**, *99*, 570. (f) Krebs, H. J.; Bonzel, H. P.; Schwarting, W.; Gafner, G. *J. Catal.* **1981**, *72*, 199.

(3) (a) Poutsma, M. L.; Elek, L. F.; Ibarbia, P.; Risch, H.; Rabo, J. A. *J. Catal.* **1978**, *52*, 157. (b) Vannice, M. A. *J. Catal.* **1975**, *37*, 449. (c) Hoffmann, F. M.; Robbins, J. L. *J. Electron Spectrosc. Relat. Phenom.* **1987**, *45*, 421.

(4) Vannice, M. A. *Catal. Rev. Sci. Eng.* **1976**, *14*, 153.

(5) Bell, A. T. *Catal. Rev. Sci. Eng.* **1981**, *23*, 203.

(6) Masters, C. *Adv. Organomet. Chem.* **1979**, *17*, 61.

Figure 1. High-resolution electron energy loss spectra recorded after exposure of a saturated overlayer of CO on Ru(001) to "110 L" of atomic hydrogen (a), or deuterium (b), at 100 K and after annealing to 150 K. The peaks near 1200, 1700 and 2000 cm^{-1} identify η^2-HCO, η'-HCO, and chemisorbed CO respectively.

•

preliminary spectroscopic study presented here clearly identifies $\eta^1(C)$-HCO (**1**) and $\eta^2(C,O)$-HCO (**2**) as these intermediates on the Ru(001) surface. We were able to effect reaction, under

UHV conditions, by exposing gas-phase atomic hydrogen,[7] rather than molecular hydrogen, to a Ru(001) surface that is saturated with CO. By virtue of the bond dissociation energy, atomic hydrogen corresponds to a state of *much* higher chemical potential and, consequently, to a state of higher reactivity.[8] The UHV chamber in which the HREELS experiments were performed has been described previously,[11] as have the properties and method of preparation of the saturated CO overlayer, the fractional coverage of which is 0.65.[12]

Shown in Figure 1 are HREEL spectra recorded after exposure of the saturated CO overlayer on the Ru(001) surface to "110 langmuirs" of atomic hydrogen (Figure 1a) and atomic deuterium (Figure 1b)[13] at 100 K, followed by annealing to 150 K (to desorb

(7) The atomic hydrogen is generated by a hot (~1800 K) tungsten filament.

(8) This reactivity is verified by the observation that the saturation fractional coverage of hydrogen on Ru(001), θ_H, is 1.5 by dosing atomic hydrogen;[9] the saturation coverage of dissociatively chemisorbed molecular hydrogen is unity.[10]

(9) Lu, I. C.; Jachimowski, T. A.; Weinberg, W. H. In preparation.

(10) Sun, Y. K.; Weinberg, W. H. *Surf. Sci.* **1989**, *214*, L246.

(11) Thomas, G. E.; Weinberg, W. H. *Rev. Sci. Instrum.* **1979**, *50*, 497.

(12) Williams, E. D.; Weinberg, W. H. *Surf. Sci.* **1979**, *82*, 93.

(13) The atomic hydrogen exposure is calculated in terms of the background molecular hydrogen pressure, since the dissociation efficiency of the hot filament is unknown. Note that 1 langmuir = 10^{-6} Torr·s.

Table I. Mode Assignments for η^1-HCO Produced by CO Hydrogenation on Ru(001), with Corresponding Assignments for the Model Compounds $CH_3O(HCO)^a$ and RhOEP(HCO) [OEP = octaethylporphyrin][b,c]

mode	η^1-HCO	CH₃O-(HCO)	RhOEP-(HCO)	η^1-DCO	CH₃O-(DCO)
ν(CO)	1730	1754	1700	1745	1739
ν(CH)	2940	2943	–	2130	2216
δ(CH)	1450	1371	–	1060	1048
π(CH)	1015	1032	–	830	870

a Reference 14. *b* Reference 15. *c* All frequencies are in cm⁻¹.

Table II. Mode Assignments for η^2-HCO Produced by CO Hydrogenation on Ru(001), with Corresponding Assignments for η^2-HCO Produced by Formaldehyde Decomposition on Ru(001)[a,b]

mode	η^2-HCO		η^2-DCO	
	this study	ref 16	this study	ref 16
ν(CO)	1240	1180	1215	1160
ν(CH)	2940	2900	2130	–
δ(CH)	1450	1400	1060	980
π(CH)	1240	1065	930	825

a Reference 16. *b* All frequencies are in cm⁻¹.

multilayer water that adsorbs from the background). Comparison of these spectra allows immediate identification of the peaks at 1240 and 1215 cm⁻¹, 1730 and 1745 cm⁻¹, and 2000 and 2015 cm⁻¹ as being due to carbon–oxygen stretching vibrations, since there is no significant isotopic shift. We assign the 2000-cm⁻¹ modes to unreacted CO; the 1700-cm⁻¹ modes to a double bond between carbon and oxygen (i.e., the carbon atom has rehybridized from sp in CO to sp²), which suggests η^1-HCO; and the 1200-cm⁻¹ modes to a carbon–oxygen bond with a bond order that has nearly decreased to 1, suggesting η^2 coordination and, hence, η^2-HCO. The remaining vibrational modes of the surface formyls, which confirm their presence, are assigned as follows: δ(CH) [δ(CD)], the in-plane bend at 1450 (1060) cm⁻¹; and ν(CH) [ν(CD)], the carbon–hydrogen stretch at 2940 (2130) cm⁻¹ (resolved clearly in off-specular spectra). The peaks at 1015 (830) and 1240 (930) cm⁻¹ are assigned to π(CH) [π(CD)], the out-of-plane bend, of η^1-formyl and η^2-formyl, respectively. Justification for these mode assignments can be obtained by comparison with vibrational data for the model compounds CH₃O(HCO) and CH₃O(DCO),[14] as well as organometallic analogues,[15] for the η^1-formyl, and HREELS data describing formaldehyde decomposition on Ru(001)[16] for the η^2-formyl. The correspondence is shown in Tables I and II. The peak at 3480 (2600) cm⁻¹ is assigned to the stretching mode of a small amount of adsorbed H₂O (D₂O),[17] introduced as a result of the atomic dosing procedure.

Since the hydrogenation reaction occurs with high probability at an astonishingly low surface temperature (100 K), the reaction appears to obey pseudo-Eley–Rideal (ER) kinetics, as alluded to

by Harris and Kasemo,[18] where the incident hydrogen atom traps (i.e., loses the normal component of its gas-phase momentum) but does not accommodate (i.e., maintains its parallel momentum) to the surface temperature.[19] Subsequently, this atom, by virtue of the momentum retained in the parallel direction, collides and reacts with a chemisorbed CO molecule to form η^1-HCO. Herein lies the chemical advantage of the atomic hydrogen: at no point do we need to break the strong Ru–H bond, this being the major reason why the Langmuir–Hinshelwood (LH) reaction[20] is thermodynamically and kinetically unfavorable. Overlap of the nonbonding orbital of HCO with the empty metal d_σ-orbitals, along with backdonation from the filled metal d_π-orbitals into the π^*-orbital of the HCO, can then result in the more stable η^2-HCO bonding configuration. The concentration ratio of η^1- to η^2-formyls would be expected to be dictated by the electron density of the Ru surface at the Fermi level which is available for backdonation. On Ru(001), this density seems insufficient to form a uniform overlayer of the favored η^2-HCO.

In conclusion, we can confidently assert that we have observed the hydrogenation of CO (to formyl intermediates) on a well-characterized metal surface, under UHV conditions. A more complete discussion on this work will be presented elsewhere.[22]

(14) Shimanouchi, T. Tables of Vibrational Frequencies—Consolidated Vol. 1. *Natl. Stand. Ref. Data Ser. U.S., Natl. Bur. Stand. NSRDS-NBS 39* **1972.**

(15) Wayland, B. B.; Woods, B. A. *J. Chem. Soc., Chem. Commun.* **1981,** 700.

(16) Anton, A. B.; Parmeter, J. E.; Weinberg, W. H. *J. Am. Chem. Soc.* **1986,** *108,* 1823.

(17) Thiel, P. A.; Hoffmann, F. H.; Weinberg, W. H. *J. Chem. Phys.* **1981,** *75,* 5556.

(18) Harris, J; Kasemo, B. *Surf. Sci.* **1981,** *105,* L281.

(19) We do not expect the direct ER mechanism (where the incident H atom neither traps nor accommodates to the surface before reaction) to contribute to the production of HCO because the orientation of the adsorbed CO molecule, with the oxygen (or nonreactive) end protruding from the surface, will result in a vanishingly small direct reaction cross section.

(20) Most surface reactions exhibit LH kinetics, where both reactants have trapped and accommodated to the surface before reaction.[21]

(21) Weinberg, W. H. In *Dynamics of Gas–Surface Collisions*; Ashfold, M. N. R., Rettner, C. T., Eds.; Royal Society of Chemistry: Letchworth, 1991; pp 171–220.

(22) Mitchell, W. J.; Xie, J; Wang, Y.-Q.; Weinberg, W. H. In preparation.

Carbon monoxide hydrogenation on the Ru(001) surface at low temperature using gas-phase atomic hydrogen *

W.J. Mitchell, J. Xie, Y. Wang, and W.H. Weinberg

Department of Chemical Engineering, University of California,
Santa Barbara, California 93106, U.S.A.

Hydrogenation of carbon monoxide on the Ru(001) surface has been investigated using high-resolution electron energy loss spectroscopy. Exposing gas-phase atomic hydrogen to a saturated carbon monoxide overlayer on Ru(001) at 100 K results in reaction (via Eley-Rideal kinetics) under ultrahigh vacuum conditions. The mechanism of this reaction is believed to be a good representation of the actual Langmuir-Hinshelwood hydrogen migration reaction that would occur under industrial conditions. Both η^1- and η^2-formyl are clearly identified as initial reaction intermediates. Heating the surface to 180 K decomposes some of the η^1-formyl, leading to adsorbed CO and hydrogen desorption, with the remainder of the η^1-formyl converting to η^2-formyl. Further annealing to 250 K leads to complete decomposition of the η^2-formyl, resulting in hydrogen desorption and regeneration of the original CO overlayer. This work represents the first isolation and spectroscopic identification of any reaction intermediate for carbon monoxide hydrogenation on any well-characterized surface at low pressure and temperature.

1. INTRODUCTION

Over the past two decades, there has been intense research interest in the Fischer-Tropsch and related processes as synthetic routes to petroleum products. Developed initially in 1925, the Fischer-Tropsch synthesis reaction involves the conversion of CO and H_2 (derived from coal as synthesis gas) over a metallic catalyst to form hydrocarbon fuels and oxygenated chemicals [1].

Surface science studies performed on this reaction system have considered numerous single-crystalline transition metal surfaces and a wide range of temperature and pressure. Under ultrahigh vacuum (UHV) conditions, no chemical reaction between CO and H_2 has been observed [2-8]. However, at higher pressures (order of 10–100 Torr), steady-state reactions involving coadsorbed CO and hydrogen were observed, resulting in methane and some higher alkane products on Ru and Ni [9, 10], Pd, Pt, and Ir [11], and Fe[12, 13]. Using *ex situ* characterization of the Ru, Ni, and Fe

surfaces, a reaction mechanism was proposed in which the initial step was dissociative chemisorption of CO to give surface-bound carbide groups. It was suggested that the carbide intermediates then react with adsorbed hydrogen to give the final alkane products via methyne, methylene, and methyl surface intermediates. On the other hand, the probability of dissociative chemisorption of CO on Pt, Pd, and Ir surfaces is much smaller than on Fe, Ni, and Ru. Thus, it has been argued that the initial step in the hydrogenation reaction on these surfaces involves the insertion of hydrogen into coadsorbed CO to produce surface-bound formyls [14]. Dehydration and further hydrogenation reactions result in the observed alkane products. Moreover, homogeneous catalysis studies (based on organometallic complexes) also suggest metal formyl compounds as important intermediates in the CO hydrogenation reaction [16-20], where the proposed initial step is migration of a metal hydride to a CO ligand to form the metal formyl (also referred to as a CO insertion

428

reaction). This insertion mechanism has ample organometallic precedent, since several transition metal formyl (and formaldehyde) derivatives have been isolated experimentally [21-29], albeit via indirect methods that usually involve intermolecular hydrogen transfer from borohydrides, BL_3H^- (L = ligand), to cationic metal carbonyls, $M(CO)_n^+$.

In this report, we identify, via high-resolution energy loss spectroscopy (HREELS), the initial surface reaction intermediates that result when a saturated CO overlayer on the Ru(001) surface is exposed to gas-phase atomic hydrogen (rather than molecular hydrogen) under UHV conditions. This result demonstrates the viability of an additional CO hydrogenation mechanism operating on the Ru surface (especially in view of the fact that CO dissociation on Ru is both activated with respect to the gas phase and endothermic with respect to molecularly chemisorbed CO [30]). The use of atomic hydrogen has captured much attention recently [31-34] since it allows UHV surface analysis techniques to be applied to those surface reactions that usually occur only at ambient (or higher) pressures and/or high temperatures.

2. EXPERIMENTAL SYSTEM

Both the HREEL spectrometer and the UHV system in which it is contained have been described in detail elsewhere [35]. The resolution of the spectrometer varied between 30 and 55 cm-1 (full-width at half-maximum), while maintaining a count rate of at least 1×10^5 Hz in the elastically scattered beam in the specular direction. Incident beam energies of approximately 5.5 eV were used.

The Ru(001) crystal was mounted on a home-built radiation-shielded cryostat [36] which can reach 77 K with liquid nitrogen cooling and less than 20 K with liquid helium cooling (not used in the present study). The Ru sample was cleaned by using standard techniques of Ar^+ sputtering, and annealing in oxygen. Surface cleanliness was monitored with HREELS, a clean surface resulting in a featureless spectrum.

The CO (Matheson, 99.99%) was exposed to the surface by backfilling the UHV chamber through a leak valve. Both H and D atoms were generated *in situ* by dissociating H_2 (Matheson,

99.9995%) and D_2 (Matheson, 99.5%) with a hot tungsten filament (≈ 1800 K, as measured by a pyrometer) held 1-inch from the crystal. During exposure to the atomized hydrogen, the surface temperature would increase by approximately 20 K due to radiation from the hot filament. All exposures are given in Langmuirs (1 L = 10^{-6} Torr-s) in terms of *molecular* pressures as measured by an ion gauge. No correction for differing ionization sensitivities was made.

The saturated CO overlayer on the Ru(001) surface ($\theta_{CO} = 0.65$) was prepared by exposing 6 L CO to the surface at 77 K and then annealing to 270 K. Loss features at 445 and 2070 cm-1 in the HREEL spectrum are characteristic of the saturated overlayer with CO occupying on-top sites [37].

3. RESULTS

Before discussing our HREELS results, we first report a separate result from a temperature programmed desorption (TPD) spectroscopic study of this reaction system [38]. For the hydrogen exposures investigated here, it was found that two hydrogen desorption peaks were observed at 200 and 270 K, in contrast, for example, to hydrogen desorption from the clean Ru(001) surface where only one peak at approximately 320 K is observed. Moreover, only H_2 and CO were observed to desorb from the surface, and the desorption of CO is identical to that from the clean surface. Applying the method of Redhead [39] with a first-order pre-exponential factor of 10^{13} s-1 gives activation energies of 11.5 and 15.7 kcal/mol for the hydrogen desorption peaks at 200 and 270 K, respectively.

Shown in Figs. 1 and 2 are HREEL spectra measured after exposure of the saturated CO overlayer to "50 L" of atomic deuterium and hydrogen, respectively, at a surface temperature of 100 K, followed by annealing to the indicated temperatures. We have utilized the maximum entropy spectral estimation (MESE) method, developed recently within our group [40-42], to assign all features in the HREEL spectra presented here. This technique results in EEL spectra with ultimate resolution (intrinsic lineshapes), which consequently allows the assignment of modes that are not clearly visible in the measured spectrum.
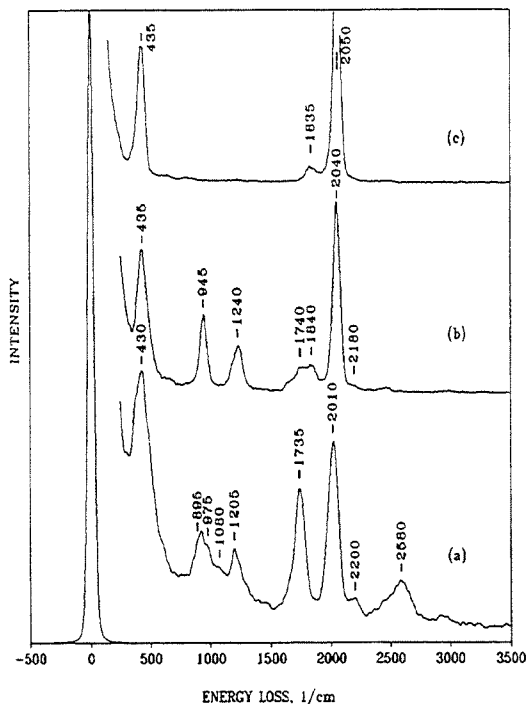
Figure 1. High-resolution electron energy loss spectra recorded after exposure of a saturated overlayer of CO on Ru(001) to "50 L" of atomic deuterium at 100 K, followed by annealing to (a) 150 K, (b) 180 K, and (c) 220 K for 60 s.
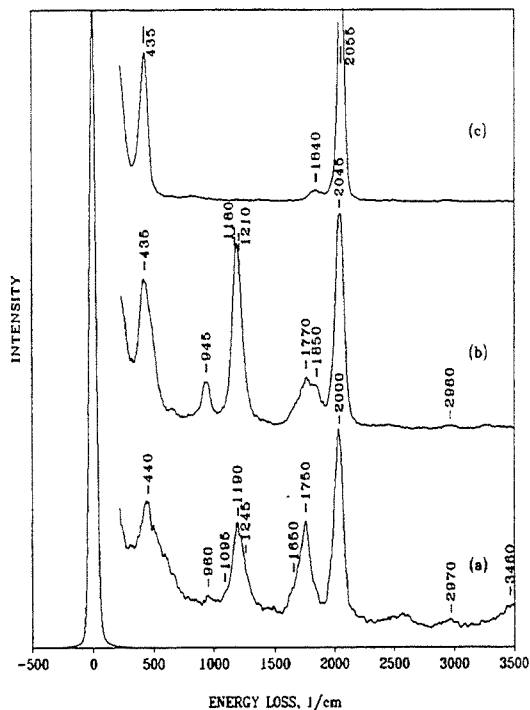

Figure 2. High-resolution electron energy loss spectra recorded after exposure of a saturated overlayer of CO on Ru(001) to "50 L" of atomic hydrogen at 100 K, followed by annealing to (a) 150 K, (b) 180 K, and (c) 220 K for 60 s.

The surface is first heated to 150 K for 60 s, cf., Figs. 1(a) and 2(a), to remove some of the water which had adsorbed from the background (generated by H and D atoms striking the chamber walls). Simple calculations, using the activation energies quoted above, indicate that no decomposition of the reaction intermediates would be expected if the hydrogen desorption is reaction limited. This was verified experimentally by comparing with HREEL spectra measured at 100 K. Comparison of the spectra at 150 K in Figs. 1 and 2 allows immediate identification of the modes at 1735–1750 cm^{-1}, as well as 2000–2010 cm^{-1}, to carbon-oxygen stretching vibrations since there is no significant isotopic shift. The strong features resolved at 895 and 975 cm^{-1} are assigned to CD bending modes in Fig 1(a). These features shift to

1095 and 1190 cm^{-1} in the hydrogenated surface species, cf., Fig. 2(a). The significant difference in intensity between these two bending modes in the hydrogenated species, as compared to the almost equal intensity in the deuterated species, implies that there is a peak at about 1200 cm^{-1} in both Figs. 1(a) and 2(a) that does not shift with the hydrogen isotope, hence, identifying an additional carbon-oxygen stretching vibration. In other words, in the hydrogen spectra of Fig. 2(a), the 1190 cm^{-1} peak is a result of overlapping peaks due to the CO stretch and the CH bend. These two modes are not resolved by the MESE method at 150 K, due to the nature of the surface disorder at this temperature: a very disordered surface leads to inhomogeneous, or Gaussian, broadening of the loss features. After annealing to 180 K, however, with improved

67

Table 1. Mode assignments for η^1- and η^2-HCO produced by CO hydrogenation on Ru(001), with corresponding assignments for the model compounds Rh(OEP)(HCO)[a], V(cp$_2$)CO(HCO)[b], CH$_3$(HCO)[c], and for η^2-HCO resulting from formaldehyde decomposition on Ru(001)[d,e].

mode	η^1-HCO				η^1-DCO		η^2-HCO		η^2-DCO	
	this study	ref 22	ref 23	ref 44	this study	ref 44	this study	ref 15	this study	ref 15
v(CO)	1750	1690	1700	1754	1735	1739	1190	1180	1205	1160
v(CH)	2970	-	-	2943	2200	2216	2970	2900	2200	-
CH bending	1095	-	-	1032	895	870	-	1065	-	825
	1245			1371	1080	1048	1190	1400	975	980

[a]Reference 22. [b]Reference 23. [c]Reference 44. [d]Reference 15. [e]All frequencies are in cm-1.

surface order, we can resolve these two modes, as discussed below. With reference to HREEL spectra obtained for water adsorption on Ru(001) [43], the modes at 2580 and 3460 cm-1 in Figs. 1(a) and 2(a) are assigned to v(OD) and v(OH) of residual surface water, respectively. The shoulder at 1650 cm-1 in Fig. 2(a) corresponds to the scissoring mode, δ(H$_2$O). The scissoring mode of D$_2$O at about 1200 cm-1 is not resolved. Features at 2200 and 2970 cm-1 (clearly resolved in off-specular spectra which are not shown) are assigned to the carbon-hydrogen stretching vibrations, v(CD) and v(CH), respectively. An additional CH bending mode at 1245 cm-1 in Fig. 2(a) is identified by the MESE technique. This mode shifts to 1080 cm-1 in the deuterated species, cf., Fig. 1(a). The peak at 960 cm-1 in Fig. 2(a) is discussed below.

With the above assignments in mind, and with particular reference to the three carbonyl bands that were observed, identification of the initial reaction intermediates can be made. The band near 2000 cm-1 identifies unreacted CO; the band near 1750 cm-1 identifies a double bond between carbon and oxygen (i.e., the carbon atom has rehybridized from sp in CO to sp^2) which suggests η^1(C)-HCO [22, 23, 44]; and the band near 1200 cm-1 identifies a carbon-oxygen bond with a bond order that has decreased nearly to one, suggesting η^2-coordination and, hence, η^2(C,O)-HCO [15]. Justification of these assignments can be obtained by comparison with vibrational data available in the literature, as summarized in Table 1.

After annealing to 180 K for 60 s, cf., Figs. 1(b) and 2(b), the η^1-formyl has largely decomposed or converted to some other species, as judged by the significant decrease of the band near 1750 cm-1 in both spectra. A feature at 1840-1850 cm-1 appears in both spectra, which identifies CO that is chemisorbed in a bridge site resulting from decomposition of the η^1-formyl. Furthermore, a slight increase in intensity of the mode at 2040 cm-1 in these spectra (upshifted from 1990-2010 cm-1) may be evidence for additional on-top CO. From Fig. 1(b), we see that there may be a slight increase in the intensity of the peak of v(CO) of η^2-DCO (upshifted to 1240 cm-1), and, we see a clear increase in the intensity of the peak at 945 cm-1, a part of which is due to a CD bending mode in η^2-DCO. The other bending mode of η^2-DCO is not resolved. Since the bending modes at 895 and 1080 cm-1 have attenuated appreciably, cf., Figs. 1(a) and 1(b), we assign these modes to η^1-DCO. These assignments are supported in Fig. 2(b) since the overlapping CH bending and CO stretching modes of η^2-HCO, which are now resolved by the MESE method at 1180 and 1210 cm-1, have increased, and the CH bending modes of η^1-HCO at 1095 and 1245 cm-1 have decreased.

The feature that appears at 945 cm-1 in Fig 2(b), downshifted from 960 cm-1 in Fig 2(a), is interesting. It cannot be assigned to an increase in the intensity of the other (previously unresolved) CH bending mode of η^2-HCO since this peak is not observed to shift upon deuteration, i.e., the corresponding bending mode in η^2-DCO is not resolved. This implies that the mode involves mainly CO motion, and recall that its increase in

intensity correlates with the decomposition of η^1-HCO. We tentatively assign this peak to a second form of η^2-HCO bound to the surface such that its C–O bond is weakened compared to the initially formed η^2-HCO. An analogy is the bridge-bonded CO that is also produced by the decomposition of η^1-HCO. We conclude that the η^1-formyl intermediate is removed by two channels: decomposition to adsorbed CO (bridge and on-top sites) and desorbing hydrogen (the 200 K peak in the hydrogen TPD spectra), as well as conversion to η^2-formyl (primarily one with an unusually low stretching frequency).

The HREEL spectra measured after annealing the surface to 250 K for 60 s, cf., Figs. 1(c) and 2(c), show an increase in intensity in the feature due to linearly adsorbed CO at 2050 cm-1, whereas those modes characteristic of the η^2-formyls are absent, indicating that they have both decomposed to CO and hydrogen which desorbs (identifying the source of the 270 K hydrogen TPD peak).

4. DISCUSSION

The results presented here show clearly that while coadsorbed hydrogen (from H_2) and CO do not react under UHV conditions, atomic hydrogen incident from the gas phase hydrogenates adsorbed CO on Ru(001) at surface temperatures as low as 100 K. Consequently, the reaction appears to follow an Eley-Rideal (ER) mechanism, alluded to by Harris and Kasemo [45], where the incident hydrogen atom traps (i.e., loses the normal component of its gas-phase momentum) but does not accommodate to the surface temperature and

chemisorb prior to reaction (i.e., maintains some parallel momentum). Direct ER kinetics (where the incident atom neither traps nor accommodates to the surface prior to reaction) might not be expected since the orientation of the adsorbed CO, with the oxygen end protruding from the surface, results in a very small direct reaction cross section for HCO formation [46].

The observed ER reaction is believed to proceed as follows. The 'hot' hydrogen atom collides with an adsorbed CO molecule, whereupon interaction of the H 1s-orbital with the CO π^*-orbital leads to hydrogen insertion (i.e., rehybridization of the acyl carbon) and, hence, formation of η^1-HCO, cf., Fig. 3(a). *Ab initio* studies of the formation of metalloformyl complexes (M-HCO) from organometallic hydridocarbonyls (H-M-CO) indicate that the Langmuir-Hinshelwood (LH) hydrogenation reaction, where the reactants are trapped and accommodated to the surface, can proceed through a 3-center transition state where the hydrogen 1s-orbital overlaps both a metal d_σ-orbital (bond breaking) and the CO π^*-orbital (bond formation) [16-19]. Consequently, the intermediates that result from the ER reaction should be essentially the same as those produced by the LH insertion reaction between coadsorbed H and CO (observable only at higher pressures and temperatures) [49] since the mechanisms closely resemble each other. The major difference is that no metal-hydrogen bond is broken in the ER reaction. This is why the LH reaction that results in the formyl intermediate is thermodynamically and kinetically unfavored ($\Delta H_{LH} \approx 45$ kcal/mol) and why we can observe the ER reaction under UHV conditions ($\Delta H_{ER} \approx -15$ kcal/mol) [50].

The η^2-coordination geometry results from overlap of the highest nonbonding orbital of the η^1-formyl (namely, the lone pair on the oxygen atom) with empty metal d_σ-orbitals, along with backdonation from filled metal d_π-orbitals into the lowest unoccupied orbital of the η^1-formyl (namely, the π^*_{CO} orbital localized on the carbon atom). This interaction has ample precedent in the organometallic literature [16, 20, 24] resulting in an η^2-formyl with substantial alkoxy-carbene character, where the carbon has undergone nearly complete rehybridization from sp^2 to sp^3 and the carbon-oxygen bond order has been lowered to
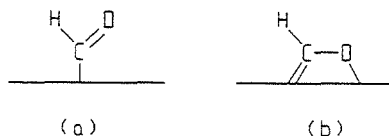

Figure 3. Proposed bonding configurations for the η^1- [(a)] and η^2- [(b)] formyls, as observed in homogeneous complexes.

nearly one, cf., Fig. 3(b). The production of the η^2-formyl intermediate depends critically on the ability of the metal to backdonate charge, since the dative lone-pair bond from oxygen is weak [20]. On Ru(001), it appears this ability is insufficient to form a uniform overlayer of the favored η^2-formyl at 100 K. However, annealing to 180 K does lead to further production from the conversion of the η^1-formyl indicating that the generation of η^2-formyl is a thermally activated reaction. The apparent synthesis of two different types of η^2-formyl on the surface, presumably with different local bonding geometries, is a particularly fascinating result.

5. CONCLUSIONS

In the surface science field, it is difficult to identify the exclusiveness of a particular reaction mechanism when compared to all others, especially in the case of catalytic CO hydrogenation, a reaction system not usually amenable to a detailed experimental mechanistic analysis. Hence, although it has been accepted that this hydrogenation reaction on Ru predominantly follows a CO dissociation channel, we might expect other channels to contribute to the overall rate (especially on Ru where the dissociative chemisorption of CO is endothermic). To this end, we have shown that the insertion of hydrogen into chemisorbed CO can occur on Ru (albeit via ER kinetics using gas-phase atomic hydrogen), which results in adsorbed formyls (bound in both an η^1- and an η^2-configuration). These intermediates have been isolated in numerous organometallic complexes, and in one case, on a transition metal surface via the decomposition of formaldehyde. Furthermore, extensive precedents exist for the hydrogen insertion step proposed here. We also find that the η^1-formyl has significantly decomposed to CO and hydrogen and converted to a second kind of η^2-formyl after annealing to 180 K for 60 s (identifying the 200 K peak in hydrogen TPD spectra). Both η^2-formyls decompose exclusively to CO and hydrogen after annealing to 250 K for 60 s (identifying the 270 K TPD peak).

REFERENCES

1. F. Fischer and H. Tropsch, Chem. Ber., 59 (1926) 830.
2. J. Benziger and R. Madix, Surf. Sci., 77 (1978) L379.
3. Nyberg and L. Westerlund, Surf. Sci., 256 (1991) 9.
4. D.E. Ibbotson, T.S. Wittrig, and W.H. Weinberg, Surf. Sci., 111 (1981) 149.
5. N.D.S. Chesters and M.A. Chesters, Surf. Sci., 175 (1986) L811.
6. H. Conrad, G. Ertl, and E.E. Latta, J. Catal., 35 (1974) 363.
7. D.W. Goodman, J.T. Yates, and T.E. Madey, Surf. Sci., 93 (1980) L315.
8. J.L. Gland, D.A. Fischer, D.H. Parker, and S. Shen, Langmuir, 7 (1991) 2574.
9. R.D. Kelley and D.W. Goodman, Surf. Sci., 123 (1982) L743.
10. F.M. Hoffmann and J.L. Robbins, J. Electron Spectrosc. Relat. Phenom., 45 (1987) 421.
11. M.A. Vannice, Catal. Rev. Sci. Eng., 14 (1976) 153.
12. H.J. Krebs, H.P. Bonzel, and G. Gafner, Surf. Sci., 88 (1979) 269.
13. H.J. Krebs and H.P. Bonzel, Surf. Sci., 99 (1980) 570.
14. Surface formyls, resulting from formaldehyde decomposition, have been isolated on the Ru(001) surface [15].
15. A.B. Anton, J.E. Parmeter, and W.H. Weinberg, J. Am. Chem. Soc., 108 (1986) 1823.
16. A.K. Rappe, J. Am. Chem. Soc., 109 (1976) 5605.
17. N. Koga and K. Morokuma, New. J. Chem., 15 (1991) 749.
18. G. Pacchioni, P. Fantucci, J. Koutecky and, V. Ponec, J. Catal., 112 (1988) 34.
19. N. Koga and K. Morokuma, J. Am. Chem. Soc., 108 (1986) 6136.
20. M.D. Curtis, K.-B. Shiu, and W.M. Butler, J. Am. Chem. Soc., 108 (1986) 1550.
21. C.P. Casey, M.W. Meszaros, S.M. Neumann, I.G. Cesa, and K.J. Haller, Organometallics, 4 (1985) 143.
22. B.B. Wayland and B.A. Woods, J. Chem. Soc., Chem. Commun., (1981) 700.
23. C. Floriani, Pure and Appl. Chem., 55 (1983) 1.

24. P.T. Wolczanski and J.E. Bercaw, Acc. Chem. Res., 13 (1980) 121.

25. C.P. Casey, S.M. Neumann, M.A. Andrews, and D.R. McAlister, Pure and Appl. Chem., 52 (1980) 625.

26. K.L. Brown, G.R. Clark, C.E.L. Headford, K. Marsden, and W.R. Roper, J. Am. Chem. Soc., 101 (1979) 503.

27. H. Berke, W. Bankhardt, G. Huttner, J. von Seyerl, and L. Zsolnai, Chem. Ber., 114 (1981) 2754.

28. S. Gambarotta, C. Floriani, A. Chiesi-Villa, and C. Guastini, J. Am. Chem. Soc., 104 (1982) 2019.

29. P.J. Fagan, K.G. Moloy, and T.J. Marks, J. Am. Chem. Soc., 103 (1981) 6959.

30. A.T. Bell, Catal. Rev. Sci. Eng., 23 (1981) 203.

31. W.J. Mitchell, Y. Wang, J. Xie, and W.H. Weinberg, J. Am. Chem. Soc., 115 (1993) 4381.

32. M. Xi and B.E. Bent, J. Phys. Chem., in press.

33. M. Xi and B.E. Bent, J. Vac. Sci. Technol. B, 10 (1992) 2440.

34. J. Xie, W.J. Mitchell, Y. Wang, and W.H. Weinberg, in preparation.

35. G.E. Thomas and W.H. Weinberg, Rev. Sci. Instrum., 50 (1979) 497.

36. W.J. Mitchell, Y. Wang, J. Xie, and W.H. Weinberg, in preparation.

37. G.E. Thomas and W.H. Weinberg, J. Chem. Phys., 70 (1979) 1437.

38. T.A. Jachimowski and W.H. Weinberg, in preparation.

39. P.A. Redhead, Vacuum, 12 (1962) 203.

40. Y. Wang and W.H. Weinberg, Phys. Rev. Lett., 69 (1992) 3326.

41. Y. Wang and W.H. Weinberg, 287/288 (1993) 1102.

42. Y. Wang and W.H. Weinberg, J. Electron. Spectrosc. Rel. Phenom., submitted.

43. P.A. Thiel, F.H. Hoffmann, and W.H. Weinberg, J. Chem. Phys., 75 (1981) 5556.

44. T. Shimanouchi, Tables of Vibrational Frequencies- Consolidated Vol. 1, NSRDS-NBS 39, 1972.

45. J. Harris and B. Kasemo, Surf. Sci., 105 (1981) L281.

46. The possibility also exists for a direct ER reaction with the oxygen end of the adsorbed CO molecule to form a COH intermediate. Detailed ab initio calculations on the gas phase H + CO system indicate that a metastable minimum exists for COH at 1.04 eV above H + CO, with a barrier to dissociation of 0.68 eV [47]. Experimental evidence for a short lived COH intermediate exists [48]. Atomic hydrogen incident on the Ru(001) surface, accelerated by the $\approx$ 3 eV chemisorption well, would have sufficient energy upon a direct collision with adsorbed CO to form a COH intermediate.

47. T.H. Dunning, J.Chem. Phys., 73 (1980) 2304.

48. L.C. Geiger and G.C. Schatz, J. Phys. Chem., 88 (1984) 214.

49. It is expected that CO hydrogenation under industrial conditions (e.g., 20 bar and 500 K at the SASOL complex in South Africa) obeys a LH mechanism (irregardless of the reaction channel).

50. Assuming D(M–H) $\approx$ 60 kcal/mol, D(M–CO) $\approx$ 30 kcal/mol, D(M–HCO) $\approx$ 25 kcal/mol [24], and D(H–H) = 104 kcal/mol.

Observation of the reaction of gas-phase atomic hydrogen with Ru(001)-p(1×2)-O at 100 K

Jun Xie, William J. Mitchell, Kevin J. Lyons, Youqi Wang, and W. Henry Weinberg
Department of Chemical Engineering, University of California, Santa Barbara, Santa Barbara, California 93106

The interaction of gas-phase atomic hydrogen with chemisorbed oxygen on Ru(001) has been investigated with high-resolution electron energy loss spectroscopy. As gas-phase hydrogen atoms impinge on the $p(1\times2)$ oxygen overlayer at surface temperatures below 100 K, water is formed, a reaction which has not been observed in previous studies of coadsorbed hydrogen and oxygen on Ru(001). The water molecules which are produced exist as adsorbed monomers initially but form clusters at greater extents of reaction. Since this reaction occurs at low surface temperatures, an Eley–Rideal-like mechanism is suggested in which hydrogen atoms from the gas phase react with adsorbed oxygen before being thermally accommodated to the surface. More than 50% of the saturation coverage of oxygen can be removed by means of gas-phase atomic hydrogen. Complete removal of the oxygen overlayer is inhibited by the water that is produced in the reaction.

I. INTRODUCTION

The existence of the notorious "pressure gap" that separates UHV (ultrahigh vacuum) single-crystalline model studies from industrial catalytic investigations with much less well-defined surfaces has posed a formidable, but rewarding, challenge to surface scientists for decades.[1,2] This pressure gap is attributable to the high coverages of reactants observed at reaction temperatures under high-pressure conditions, coverages that are not attainable using conventional UHV techniques. The recent emergence of atomic sources in surface science studies, in addition to the existing powerful array of UHV experimental methods, has opened a new door to bridging this gap.[3–5] The atomic sources produce more "reactive" reagents leading to synthesis reactions that frequently can otherwise be achieved only under high-pressure conditions.

The hydrogen oxidation reaction has been studied extensively (as a prototypical oxidation reaction) on a variety of single-crystalline transition metal surfaces such as Pt, Pd, Rh, and Ni.[6–10] However, only a handful of coadsorption studies have been carried out on Ru surfaces,[11–13] due to the absence of water formation under UHV conditions. For example, Hrbek[11,12] found that water was *never* observed among the desorption products from coadsorbed hydrogen and oxygen on Ru(001). He also reported that the adsorption of hydrogen was blocked by preadsorbed oxygen from the sites typical for adsorption on a clean surface and was completely inhibited on a surface saturated with a $p(1\times2)$ oxygen overlayer. Furthermore, the oxygen coverage did not decrease, as determined via x-ray photoelectron spectroscopy (XPS) and Auger electron spectroscopy (AES), following desorption of hydrogen at lower temperatures. On the other hand, the behavior of water adsorbed on Ru(001) has been well documented.[14–19] Water adsorbs molecularly on Ru(001) at 100 K, and the thermal desorption spectra of water show three desorption features, around 165, 180, and 210 K, corresponding to desorption of a multilayer (ice), a bilayer, and a monolayer, respectively. Dissociation is negli-

gible throughout this temperature range. The sole study that exists concerning the reaction of preadsorbed oxygen with low-pressure hydrogen on Ru(001) was conducted at elevated temperatures. At a pressure of H_2 of 1.3×10^{-7} Torr, Shi *et al.*[13] were able to titrate near-saturation coverage overlayers of oxygen on Ru(001) at surface temperatures between 490 and 890 K. By monitoring the decay of the oxygen signal with time using AES and XPS, it was found that the reaction rate exhibited three distinct regimes: first, a long induction period, then a rapid reaction, and, finally, a slow reaction. The first regime was attributed to the impeded dissociative adsorption of hydrogen on a nearly saturated oxygen overlayer, the second regime to the reaction of adsorbed hydrogen atoms with "active" oxygen in $p(1\times2)$ islands, and the third regime to a slow reaction of hydrogen with an inactive form of chemisorbed oxygen in $p(2\times2)$ domains.

In this paper, we report an UHV study of the formation of water on oxygen presaturated Ru(001) at low temperatures (≤100 K), employing an atomic hydrogen source. We have used high-resolution electron energy loss spectroscopy (HREELS) to identify the reaction intermediates and products. This study elucidates the hydrogen oxidation reaction on Ru(001) and provides valuable information for future studies on more complex reaction systems in which hydrogen oxidation and water formation is a common elementary step.

II. EXPERIMENTAL DETAILS

The HREELS experiments were performed in an UHV chamber with a base pressure below 5×10^{-11} Torr. The HREEL spectrometer and other instruments contained in this chamber have been described in detail elsewhere.[20] The resolution of the HREEL spectrometer varied between 30 and 55 cm^{-1} (full width at half-maximum), while a count rate of at least 1×10^5 counts per second was maintained in the elastically scattered beam with an incident electron beam energy

72

of approximately 5.5 eV. All HREEL spectra presented and discussed here were measured in the specular direction, which was 60° from the surface normal.

The Ru(001) crystal was mounted on a home-built radiation-shielded cryostat which can reach 80 K with liquid nitrogen as a coolant or below 30 K with liquid helium (not used in the present study). The Ru sample was cleaned using standard techniques of Ar^+ sputtering and annealing in oxygen.[21] Surface cleanliness was monitored via HREELS, and the clean surface was evidenced by a featureless HREEL spectrum.

The O_2 and $H_2(D_2)$ used in this study were obtained from Matheson with reported purities of 99.998% and 99.9995% (99.5%), respectively. These gases were used without further purification and their mass spectra gave no indication of any impurities. Oxygen was adsorbed by backfilling the UHV chamber through a leak valve. The H and D atoms were generated *in situ* by dissociating H_2 and D_2 with a movable hot filament doser, consisting of a leak valve and a 1/4-in.-diam stainless-steel tube terminated with a coolable copper radiation shield which houses a 10-mm-diam flat spiral tungsten filament. The hot filament, resistively heated to about 1800 K, as measured by a pyrometer, was positioned approximately 3 cm from the crystal face during dosing. The temperature of the Ru crystal rose approximately 15 K due to thermal radiation from the hot filament. Oxygen exposures are reported in units of Langmuirs (1 L=10^{-6} Torr s). Atomic hydrogen and deuterium exposures are cited in terms of the corresponding exposures of the molecular reagents, using uncorrected ion gauge readings. We estimate that the atomic flux is on the order of 2% of the reported molecular flux.

The $p(1\times2)$ oxygen overlayer was prepared by exposing 6 L of oxygen to the sample at 80 K and then annealing to 400 K. The resulting order of the overlayer was deduced from the HREEL spectra [*vide infra*, Fig. 1(a)] and earlier reported results.[22]

III. RESULTS

Conclusive evidence for water formation via the reaction of gas-phase atomic hydrogen with the $p(1\times2)$ oxygen overlayer on Ru(001) was obtained by HREELS. Shown in Fig. 1 are HREEL spectra measured before and after exposure of the Ru(001)-$p(1\times2)$-O surface to gas-phase atomic hydrogen. The spectrum shown in Fig. 1(a) is that of Ru(001)-$p(1\times2)$-O surface, which exhibits a strong feature at 585 cm^{-1} that corresponds to the frustrated translational mode of oxygen perpendicular to the surface, $\nu_\perp(RuO)$, in the threefold site. The features at 430 and 240 cm^{-1} are due to the frustrated translation parallel to the surface, $\nu_\parallel(RuO)$, and a surface phonon band, respectively.[22] After exposure of this surface to only "1 L" of atomic hydrogen [Fig. 1(b)], the loss features clearly indicate the appearance of reaction products from hydrogen oxidation. (The quotation marks here and hereafter serve to remind the reader that these are exposures of molecular hydrogen which are approximately two orders of magnitude greater than the actual exposure of atomic hydrogen.) By comparison to the results of H_2O adsorption on Ru(001),[14–19] peak assignments can be easily made cf. Table
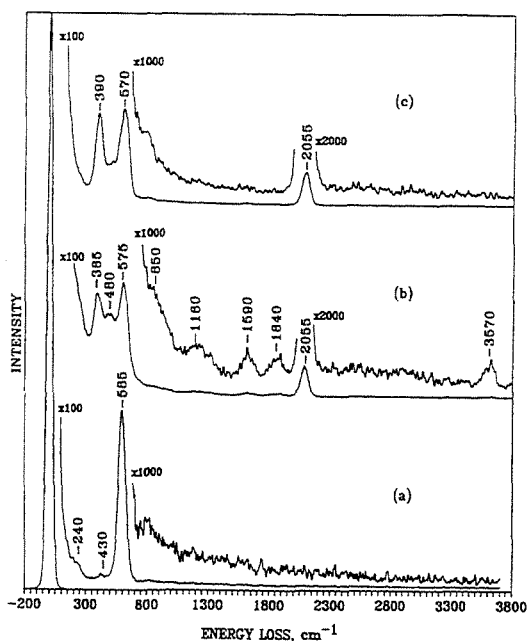

FIG. 1. HREEL spectra measured (a) before and (b) after exposure of a Ru(001)-$p(1\times2)$-O surface to 1 L of atomic hydrogen at 100 K, and (c) after annealing to 240 K.

I. The 480-cm^{-1} peak is assigned to the frustrated translational mode of H_2O perpendicular to the surface, and the broad shoulder around 850 cm^{-1} is due to the frustrated rotational modes. The 1590-cm^{-1} peak corresponds to the H_2O scissoring mode, $\delta(HOH)$. The OH stretching mode, $\nu(OH)$, is observed at 3570 cm^{-1} with a full width at half-maximum (FWHM) of about 150 cm^{-1}. The weak feature around 1160 cm^{-1} is assigned to a frustrated translational mode of hydrogen perpendicular to the surface while the other frustrated translational mode of hydrogen parallel to the surface, near 820 cm^{-1}, contributes to the shoulder at 850 cm^{-1}.[23] Due to background CO contamination, the Ru–CO frustrated translational mode as well as the CO stretching modes of CO in bridge and on-top sites are observed at 380, 1840, and 2055 cm^{-1}, respectively. The CO fractional coverage is estimated to be about 0.05. Note that $\nu(CO)$ is higher than that on a clean surface while $\nu_\perp(Ru–CO)$ is lower due to the strong effect of surface oxygen.[24]

With increasing exposure of atomic hydrogen, the sharp $\nu(OH)$ peak at 3570 cm^{-1} becomes a broad feature centered around 3390 cm^{-1} (FWHM>300 cm^{-1}), while the $\delta(HOH)$ mode shifts up to 1655 cm^{-1} cf. Fig. 2(a). These mode assignments were confirmed by substituting hydrogen with deuterium to check the *isotopic shift* of the corresponding vibrational modes. The frustrated rotational modes are shifted from 710 cm^{-1} to around 555 cm^{-1}, the same frequency range as $\nu_\perp(RuO)$, as may be seen by comparing Figs. 2(a) and 2(b). The $\delta(DOD)$ scissoring mode appears at 1200 cm^{-1}, while, as a result of some hydrogen in the back-

TABLE I. Vibrational mode assignments for adsorbed water and hydroxyls. All frequencies are in cm^{-1}.

Species	Mode	Frequency range Ref. 19	Pt(111) Ref. 8	Rh(100) Ref. 10	Ru(001)		
					Ref. 18	This study[a]	This study[b]
H$_2$O	frustrated translations	~200–500	250	···	230–430	480	···
	frustrated rotations	~500–1000	700	965	700–950	850	710 (555)
	scissoring mode	~1500–1650	1625	1655	1520–1650	1590	1655 (1200)
	OH stretch	~2500–4000	3400	3230	2950–3600	3570	3390 (2500)
OH	frustrated translation ($\perp$)	···	430	435	···	···	···
	frustrated translations ($\parallel$)	···	···	660	···	···	···
	frustrated rotation	···	1015	920	···	···	···
	OH stretch	···	3480	3180	···	···	···

[a]At low H$_2$O coverages coadsorbed with oxygen.
[b]At high H$_2$O coverages coadsorbed with oxygen. Values for D$_2$O are given in parentheses.

ground, a feature due to δ(HOD) is also observed at 1440 cm^{-1} cf. Fig. 2(b). The very weak ν(OH) feature suggests that the intensity of the peak at 1650 cm^{-1} is not due only to the δ(HOH) mode, but is also partly due to the ν(CO) mode of η^1-DCO which results from CO hydrogenation.[4] The broad peak centered at 2500 cm^{-1} is assigned to ν(OD), shifted by a factor of 1.36 with respect to ν(OH).

After annealing to 240 K, as seen in Fig. 1(c), all the modes attributable to adsorbed water are completely attenuated, leaving only the loss features due to CO and a reduced concentration of oxygen adatoms. A diminished $\nu_\perp$(RuO) feature always appears in the spectra measured after the post-annealing with a frequency lower than that for the original oxygen-saturated surface. This downshift in $\nu_\perp$(RuO) proves

conclusively that water is being synthesized on the surface at 100 K, and it desorbs completely below 240 K, i.e., we can exclude the possibility of molecular water adsorption from the background onto the Ru(001)-p(1×2)-O surface.

Shown in Fig. 3 is the $\nu_\perp$(RuO) frequency of unreacted oxygen as a function of exposure of atomic hydrogen, measured after annealing the postexposed surface to 240 K to desorb the water which is produced. Although a comprehensive correlation between $\nu_\perp$(RuO) and the fractional oxygen coverage is not available, it is well known that $\nu_\perp$(RuO) shifts down monotonically with decreasing oxygen coverage on Ru(001).[24] This important relation between the correlated decrease in $\nu_\perp$(RuO) and oxygen coverage allows us to make semiquantitative conclusions regarding the extent of the hydrogen oxidation reaction. Figure 3 clearly indicates that the residual oxygen coverage decreases upon increasing exposure to atomic hydrogen up to about 30 L. The value of $\nu_\perp$(RuO) saturates at approximately 535 cm^{-1} without any further discernible shift for hydrogen exposures from 30 to 90 L. Even though a value of $\nu_\perp$(RuO) of 535 cm^{-1} corresponds to a p(2×2) oxygen superstructure (θ_O=0.25),[22] it could also arise from scattered p(2×2) domains with the actual oxygen coverage less than one-quarter monolayer. In fact, the value of $\nu_\perp$(RuO) is observed to shift from 535 to
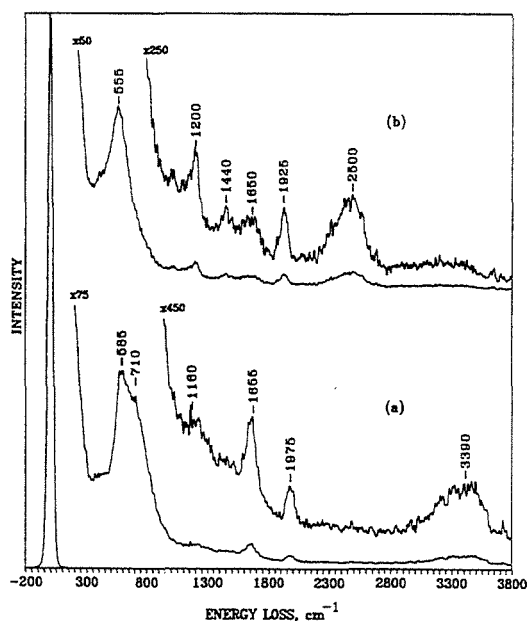

FIG. 2. HREEL spectra measured after exposure of a Ru(001)-p(1×2)-O surface (a) to 10 L of atomic hydrogen, and (b) to 10 L of atomic deuterium.
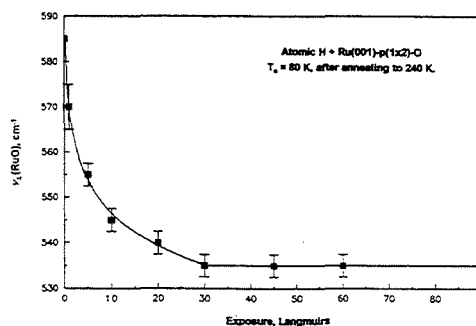

FIG. 3. Variation of the $\nu_\perp$(RuO) frequency as a function of atomic hydrogen exposure. The $\nu_\perp$(Ru–O) frequency, measured by HREELS at 80 K, is obtained after exposure of a Ru(001)-p(1×2)-O surface to atomic hydrogen at ~90–100 K followed by annealing to 240 K.

520 cm^{-1} when the residual oxygen overlayer is allowed to reorder and to relax following annealing to between 400 and 560 K. To investigate the origin of the unreacted oxygen and the influence of water which is produced, preliminary experiments have been carried out at 200 K, a temperature at which the reaction product water desorbs, during the atomic hydrogen exposure. The HREEL spectra, measured after an exposure of approximately 60 L at 200 K, show only features of adsorbed hydrogen, $v_\perp$(RuH) [$\sim$820 cm^{-1}] and $v_\parallel$(RuH) [$\sim$1120 cm^{-1}], as well as those of CO, $v_\perp$(Ru–CO) [$\sim$440 cm^{-1}] and v(CO) [$\sim$2000 cm^{-1}]. Annealing the postexposed surface to 560 K results in featureless HREEL spectra, which indicates the *complete* removal of oxygen by gas-phase atomic hydrogen under these conditions.

IV. DISCUSSION

The use of an atomic hydrogen source, in conjunction with HREELS, allows us to understand better the hydrogen oxidation reaction on Ru(001) by inducing reaction under UHV conditions. Incident gas-phase hydrogen atoms react with a $p(1\times2)$ oxygen overlayer on Ru(001) at surface temperatures as low as 90 K, showing *much* greater reactivity than their molecular counterpart after dissociative chemisorption. As noted above, dissociative adsorption of molecular hydrogen is inhibited by a $p(1\times2)$ oxygen overlayer on Ru(001), and, thus, the hydrogen oxidation reaction is not observed on this surface under UHV conditions.[11,12] For oxygen coverages below one-half monolayer, molecular hydrogen can adsorb dissociatively, but desorption of the hydrogen is favored with respect to the oxidation reaction. Even at high surface temperatures ($\sim$490–890 K), a long induction period prior to appreciable reaction, is needed on nearly saturated oxygen overlayers. Presumably, the H$_2$ adsorbs dissociatively at the $p(1\times2)$ domain edges, and the reaction occurs only in these regions, opening up the surface slowly.[13] For impinging hydrogen atoms, such an obstacle for dissociative adsorption no longer exists. Here, the hydrogen oxidation obviously proceeds via a mechanism different from the Langmuir–Hinshelwood mechanism which occurs at elevated surface temperatures. With previous studies demonstrating that coadsorbed hydrogen and oxygen produce no water on Ru(001) at low temperatures,[11,12] our results showing a reaction with high probability on Ru(001) at surface temperatures between 90 and 100 K strongly suggest that the reaction follows an Eley–Rideal-like mechanism where hydrogen atoms from the gas phase are oxidized prior to thermal accommodation with the surface.[25]

The high frequency (3570 cm^{-1}) and narrow linewidth ($\sim$150 cm^{-1}) observed for the v(OH) mode in Fig. 1(b), together with the δ(HOH) mode observed at 1590 cm^{-1}, indicate non-hydrogen-bonded water monomers after a rather low extent of reaction. Hydrogen-bonded clusters form at higher extents of reaction, as evidenced by the frequency upshift of the δ(HOH) mode as well as the broadening and frequency downshift of the v(OH) mode.[18,19]

The coexistence of hydroxyl intermediates is not clear. The high frequency and narrow linewidth of v(OH) in Fig. 1(b) is similar to that of adsorbed hydroxyls,[8] but the frustrated rotational mode of the hydroxyl, δ(OH) is absent cf.

Table I. Note also that δ(HOH) is always observed whenever v(OH) is present, even at the lowest exposure of atomic hydrogen cf. Fig. 1(b). Furthermore, in a previous thermal desorption spectroscopy (TDS) study of formic acid on Ru(001), Sun and Weinberg[26] observed that hydrogen and hydroxyls, fragments of formic acid decomposition at the defect sites, combine and desorb as water at 275 K. This suggests that the rate-determining step in water formation is the initial reaction forming hydroxyls, and, hence, we conclude that hydroxyls are not observed here.

Another interesting result is the maximum amount of oxygen that can be titrated with high probability by gas-phase atomic hydrogen from the half-monolayer $p(1\times2)$ overlayer. The removal of oxygen from Ru(001) by atomic hydrogen was demonstrated by the decrease in $v_\perp$(RuO)[24] after exposure to atomic hydrogen (and after annealing the surface to desorb water). The behavior of $v_\perp$(RuO), shown in Fig. 3 as a function of exposure to atomic hydrogen, indicates that the oxygen coverage decreases exponentially and approaches a final coverage of less than one-quarter monolayer with a $v_\perp$(RuO) of 535 cm^{-1}. This incomplete removal of surface oxygen by gas-phase atomic hydrogen at 100 K is related to the presence of water, as the preliminary experiments at 200 K show. The reaction product, water, impedes further reaction by forming a stable O$\cdots$H$_2$O complex, as was found in previous studies of water and oxygen coadsorption.[15–17] Once it is hydrogen bonded with H$_2$O, the chemisorbed oxygen becomes more anionic and, thus, less reactive with the atomic hydrogen.

V. CONCLUSIONS

The reaction of gas-phase atomic hydrogen with a $p(1\times2)$ oxygen overlayer on Ru(001) at 100 K has been studied by high-resolution electron energy loss spectroscopy. The hydrogen oxidation reaction occurs with high probability at surface temperatures between 90 and 100 K. The water that is produced is identified spectroscopically as isolated monomers at low conversions and hydrogen-bonded clusters at higher extents of reaction. All water which is formed desorbs at temperatures below 240 K. It appears that hydroxyl formation is the rate-determining step of the water formation reaction on Ru(001) since the hydroxyl intermediates cannot be trapped at these low temperatures. The reaction proceeds via an Eley–Rideal-like mechanism in which hydrogen atoms from the gas phase react, before being thermally accommodated to the surface, with chemisorbed oxygen to form hydroxyls, which react with a second hydrogen atom to produce water. More than 50% of the saturated $p(1\times2)$ oxygen overlayer on Ru(001) can be removed by gas-phase atomic hydrogen at 100 K. The unreacted oxygen remains in the form of stable hydrogen-bonded O$\cdots$H$_2$O complexes on the surface. All oxygen can be titrated at 200 K, a temperature at which the reaction product water desorbs.

ACKNOWLEDGMENT

[1]*Surface Science of Catalysis: In Situ Probes And Reaction Kinetics*, edited by D. J. Dwyer and F. M. Hoffmann, ACS Symp. Series 482 (American Chemical Society, Washington, DC, 1992).

[2]K. Christmann, *Introduction to Surface Physical Chemistry* (Springer, New York, 1992).

[3]C. T. Rettner, Phys. Rev. Lett. **69**, 383 (1992).

[4]W. J. Mitchell, Y.-Q. Wang, J. Xie, and W. H. Weinberg, J. Am. Chem. Soc. **115**, 4381 (1993).

[5]M. Xi and B. E. Bent, J. Vac. Sci. Technol. B **10**, 2440 (1992).

[6]P. R. Norton, in *The Chemical Physics of Solid Surfaces and Heterogeneous Catalysis*, edited by D. A. King and D. P. Woodruff (Elsevier, Amsterdam, 1982), p. 27.

[7]J. T. Yates, Jr., P. A. Thiel, and W. H. Weinberg, Surf. Sci. **82**, 45 (1979).

[8]G. B. Fisher and B. A. Sexton, Phys. Rev. Lett. **44**, 683 (1980); B. A. Sexton, Appl. Phys. A **26**, 1 (1981).

[9]C. Nyberg and C. G. Tengstal, Surf. Sci. **126**, 163 (1983).

[10]B. A. Gurney and W. Ho, J. Chem. Phys. **87**, 5562 (1987).

[11]J. Hrbek, J. Phys. Chem. **90**, 6217 (1986).

[12]J. Hrbek, J. Catal. **100**, 523 (1986).

[13]S.-K. Shi, J. A. Scherifels, and J. M. White, Surf. Sci. **105**, 1 (1981).

[14]P. A. Thiel, F. M. Hoffmann, and W. H. Weinberg, J. Chem. Phys. **75**, 5556 (1981).

[15]K. Kretzschmar, J. K. Sass, A. M. Bradshaw, and S. Holloway, Surf. Sci. **115**, 183 (1982).

[16]P. A. Thiel, F. M. Hoffmann, and W. H. Weinberg, Phys. Rev. Lett. **49**, 501 (1982).

[17]D. L. Doering and T. E. Madey, Surf. Sci. **123**, 305 (1982).

[18]P. A. Thiel, R. A. DePaola, and F. M. Hoffmann, J. Chem. Phys. **80**, 5326 (1984).

[19]P. A. Thiel and T. E. Madey, Surf. Sci. Rep. **7**, 211 (1987).

[20]G. E. Thomas and W. H. Weinberg, Rev. Sci. Instrum. **50**, 497 (1979).

[21]G. E. Thomas and W. H. Weinberg, J. Chem. Phys. **70**, 954 (1979).

[22]T. S. Rahman, A. B. Anton, N. R. Avery, and W. H. Weinberg, Phys. Rev. Lett. **51**, 1979 (1983).

[23]H. Conrad, R. Scala, W. Stenzel, and R. Unwin, J. Chem. Phys. **81**, 6371 (1984).

[24]G. E. Thomas and W. H. Weinberg, J. Chem. Phys. **69**, 3611 (1978).

[25]J. Harris and B. Kasemo, Surf. Sci. **105**, L281 (1981).

[26]Y.-K. Sun and W. H. Weinberg, J. Chem. Phys. **94**, 4587 (1991).

A molecular-beam study of the dissociative chemisorption of O_2 on Ir(110)-(1×2)

C. B. Mullins,[a] Y. Wang, and W. H. Weinberg

Division of Chemistry and Chemical Engineering, California Institute of Technology, Pasadena, California 91125

The zero-coverage probability of dissociative chemisorption of O_2 on Ir(110)-(1×2) has been measured using molecular-beam techniques for a wide range of incident kinetic energies, incident angles, and surface temperatures. The data indicate that a trapping-mediated mechanism is responsible for dissociative chemisorption at low energies, whereas at high energies a direct mechanism accounts for dissociative adsorption. Total energy scaling approximately describes the dissociative dynamics on the very corrugated Ir(110)-(1×2) surface.

Dissociative chemisorption on transition-metal surfaces is a key step in many industrially important heterogeneous catalytic reactions. The dynamics of dissociative chemisorption are currently poorly understood and an active area of research. In an effort to contribute further to an understanding of dissociative chemisorption, we have conducted a series of experiments to probe the interaction of molecular oxygen with the Ir(110)-(1×2) surface.

Two studies of oxygen chemisorption dynamics employing molecular beams have appeared recently. Rettner et al.[1] have studied the interaction of oxygen with a W(110) surface and concluded that the initial probability of adsorption depends strongly on the incident kinetic energy E_i scaling with the normal energy $E_n = E_i \cos^2\theta_i$, where θ_i is the angle of incidence. They also found some evidence for the existence of a weakly bound precursor to dissociative chemisorption at low incident kinetic energies. Williams et al.[2] have investigated the dynamics of dissociative adsorption of oxygen on Pt(111). They concluded that trapping-mediated chemisorption occurred for low incident energies and low surface temperatures, whereas at high incident kinetic energies a direct mechanism was likely the mechanism for chemisorption of oxygen. Taylor et al.[3] have investigated the interaction of oxygen with Ir(110)-(1×2) previously, and their work provided motivation for this study. They used thermal desorption mass spectrometry, low-energy electron diffraction, and work function measurements, and concluded that the initial probability of chemisorption was independent of surface temperature T_s. They also concluded for T_s between 300 and 700 K that the adsorption kinetics could be described by a second-order precursor model.

Zero-coverage dissociative chemisorption measurements have been made using the reflectivity method (of King and Wells[4]) employing an apparatus that will be described in detail elsewhere.[5] Briefly, the apparatus consists of a thrice differentially pumped supersonic molecular-beam source and ultrahigh vacuum scattering chamber. Low-energy electron diffraction optics, Auger electron spectroscopy, and an ion gun are mounted on the scattering chamber for obtaining and checking surface cleanliness and order. A quadrupole mass spectrometer is also mounted on the scattering chamber for thermal desorption mass spectrometry, reflectivity measurements, and beam time-of-flight measure-

ments. The source chambers contain the nozzle, a high-speed shutter, and a chopper for beam modulation as well as apertures for beam collimation. Both the scattering chamber and the third-beam chamber are pumped by turbomolecular pumps. The other two beam chambers are pumped by diffusion pumps. The Ir(110)-(1×2) sample is mounted on a manipulator in the scattering chamber which provides precise alignment of the sample in the beam. The manipulator is liquid nitrogen cooled, providing rapid cooling of the sample to 80 K. The sample temperature is determined from a 0.003-in. W/5% Re–W/26% Re thermocouple spotwelded to the back of the crystal. As mentioned above, the initial probability of adsorption data reported here have been determined by a beam reflectivity method similar to that of King and Wells.[4] The partial pressure of oxygen in the scattering chamber is used as a measure of the flux of O_2 molecules that do not chemisorb. Initial chemisorption probabilities S_0 (corresponding to chemisorption at zero coverage) are thus determined by a comparison of the initial oxygen partial pressure, following the opening of the high-speed shutter, to the oxygen partial pressure from the beam scattering from the saturated surface. Beam energies are varied by a combination of seeding and variation of nozzle temperature, and are measured by time-of-flight techniques.

Figure 1 shows S_0 as a function of incident kinetic energy for an angle of incidence of 15° with respect to the surface normal and surface temperatures of 150 and 300 K. As E_i is increased from its lowest values, S_0 decreases from a relatively high value to a minimum at ~ 4 kcal/mol. Note that this occurs for the measurements at 150 K as well as those at 300 K. The data displayed in Fig. 2 support the insensitivity of S_0 to T_s. This figure shows S_0 vs T_s for an incident angle of 45° and total incident energy of 980 cal/mol, and an incident angle of 15° and E_i of 9.1 kcal/mol. A decrease in S_0 with increasing kinetic energy in the low-energy range is associated with a trapping- or precursor-mediated chemisorption mechanism, cf. Fig. 1. A similar decrease in S_0 with E_i in the low E_i regime for O_2/W(110),[1] O_2/Pt(111),[2] N_2/W(100),[7] C_3H_8/Ir(110)-(1×2),[8] and C_4H_{10}/Ir(110)-(1×2)[8] has been observed before. However these systems displayed a strong sensitivity to surface temperature, with S_0 decreasing with increasing surface temperature. This type of behavior can be interpreted as follows: the trapping proba-
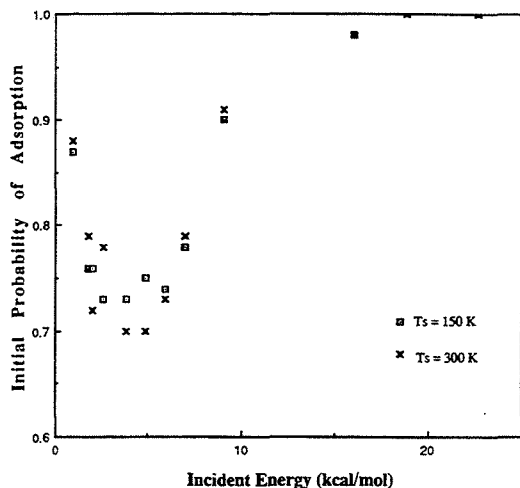
77

FIG. 1. The initial probability of dissociative chemisorption S_0 as a function of incident kinetic energy for $T_s = 150$ and 300 K, and incident angle of 15°.
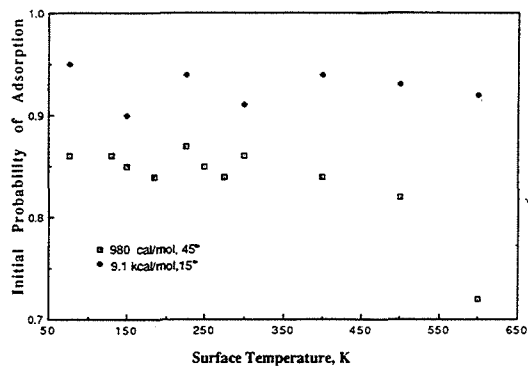

FIG. 2. The initial probability of dissociative chemisorption S_0 as a function of surface temperature for $E_i = 980$ cal/mol and $\theta_i = 45°$, and for $E_i = 9.1$ kcal/mol and $\theta_i = 15°$.

bility into the precursor state is a strong function of E_i decreasing with increasing E_i, but weakly influenced by T_s.[9] Once a particle is in the precursor state it either desorbs or chemisorbs dissociatively, the temperature dependence of which depends on the kinetic parameters for desorption and dissociation.[10] For the system under discussion, O_2/Ir(110)-(1×2), the relative insensitivity of S_0 to T_s at low E_i suggests that the activation energy for dissociation is nearly equal to the activation energy for desorption from the precursor or trapped state. The slight decrease in S_0 observed from 400 to 600 K is probably due to a decrease in the trapping probability.[9] The insensitivity of S_0 to T_s at high E_i supports the assignment of a direct mechanism to dissociative chemisorption in this regime. Behavior of this type has been observed previously,[1,7,8] but one should note that in the study by Williams et al.[2] S_0 was found to have a surface temperature dependence even at high E_i. The previous study of O_2/Ir(110)-(1×2) by Taylor et al.[3] supports these conclusions in that S_0 was determined to be insensitive to T_s from 300 to 700 K. The fact that S_0 for the O_2/Ir(110)-(1×2) system is nearly insensitive to incident angle suggests near total energy scaling for the chemisorption dynamics of this system. This is not too surprising considering that the surface reconstructs into a very corrugated geometrical structure, providing a corrugated potential energy surface. Total energy scaling in dissociative chemisorption of a diatomic has been reported previously for the N_2/W(110) system[6] and the N_2/W(100) system.[7] Chemisorption probabi-

lities S have also been determined as a function of coverage over a wide range of conditions. At low incident kinetic energies and low surface temperatures, S remains constant or decreases slowly for low coverages. This provides further supporting evidence for our assignment of a trapping-mediated chemisorption mechanism for the low E_i regime. A more complete description of the coverage dependence of the probability of dissociative chemisorption, as well as other details, will appear in a future publication.[5]

a) IBM Predoctoral Fellow.

[1] C. T. Rettner, L. A. DeLouise, and D. J. Auerbach, J. Chem. Phys. 85, 1131 (1986); J. Vac. Sci. Technol. A 4, 1491 (1986).

[2] M. D. Williams, D. S. Bethune, and A. C. Luntz, J. Chem. Phys. 88, 2843 (1988); J. Vac. Sci. Technol. A 6, 788 (1988).

[3] J. L. Taylor, D. E. Ibbotson, and W. H. Weinberg, Surf. Sci. 79, 349 (1979).

[4] D. A. King and M. G. Wells, Surf. Sci. 29, 454 (1971).

[5] C. B. Mullins, Y. Wang, and W. H. Weinberg (to be published).

[6] D. J. Auerbach, H. E. Pfnür, C. T. Rettner, J. E. Schlaegel, J. Lee, and R. J. Madix, J. Chem. Phys. 81, 2515 (1984).

[7] C. T. Rettner, H. Stein, and E. K. Schweizer, J. Chem. Phys. 89, 3337 (1988).

[8] A. V. Hamza, H. -P. Steinrück, and R. J. Madix, J. Chem. Phys. 85, 7494 (1986).

[9] C. T. Rettner, E. K. Schweizer, H. Stein, and D. J. Auerbach, Phys. Rev. Lett. 61, 986 (1988).

[10] W. H. Weinberg, in *Kinetics of Interface Reactions*, edited by M. Grunze and H. J. Kreuzer, Vol. 8 in Springer Series in Surface Science (Springer, Berlin, 1987), p. 94.

78

Electron energy loss spectroscopy of ammonia on Ru(001)

J. E. Parmeter,[a] Y. Wang, C. B. Mullins,[b] and W. H. Weinberg

Division of Chemistry and Chemical Engineering, California Institute of Technology, Pasadena, California 91125

The adsorption of ammonia on Ru(001) has been studied using high-resolution electron energy loss spectroscopy. Multilayer, second-layer, and monolayer ammonia have been characterized vibrationally. These three states desorb near 115, 130 and between approximately 150 and 350 K, respectively. The symmetric deformation mode of chemisorbed ammonia shifts down in frequency continuously with increasing coverage from approximately 1160 cm^{-1} in the low-coverage limit to approximately 1070 cm^{-1} at (monolayer) saturation. The frequency of this mode in coordination compounds of ammonia is sensitive to the charge on the metal atom (increasing with increasing positive charge), and the frequency shift of this mode on the Ru(001) surface can be correlated with the work function decrease that this surface undergoes as the ammonia coverage increases. Off-specular EEL spectra allow the weak NH_3 rocking mode and the frustrated translation of the ammonia perpendicular to the surface (i.e., the metal–nitrogen stretch) of chemisorbed ammonia to be resolved near 625 and 340 cm^{-1}, respectively. These modes have not been identified in previous EELS studies of chemisorbed ammonia on hexagonally close-packed metal surfaces. Second-layer and multilayer ammonia yield EEL spectra similar to those observed on other metal surfaces. In agreement with previous results, the adsorption of ammonia on Ru(001) at 80 K, followed by annealing, leads only to reversible desorption.

I. INTRODUCTION

The adsorption of ammonia on well-defined single-crystalline metal surfaces under ultrahigh vacuum (UHV) conditions has received considerable attention in recent years.[1-31] This subject is of interest both because it relates to industrial catalytic processes such as ammonia synthesis,[32] and because ammonia is a prototypical example of a weak donor ligand that bonds to metal atoms both in organometallic compounds[33-42] and on surfaces via the electron lone pair on the nitrogen atom. As part of a continuing study of the chemistry of nitrogen-containing molecules on the hexagonally close-packed Ru(001) surface,[43-48] we report here the results of a high-resolution electron energy loss spectroscopic (EELS) investigation of ammonia adsorption on this surface.

The interaction of ammonia with Ru(001) has been the focus of several previous studies.[18-23] Danielson et al.[18] employed thermal desorption mass spectrometry (TDMS), Auger electron spectroscopy, and low-energy electron diffraction (LEED) to study this system, and concluded that for adsorption temperatures below 300 K the chemisorbed ammonia desorbed completely reversibly, with negligible dissociation occurring upon annealing. Dissociation could be induced only be electron beam bombardment of the adsorbed ammonia, or by exposing the surface to large fluences of ammonia with the surface temperature maintained above 300 K. Benndorf and Madey[21] used LEED, TDMS, electron stimulated desorption ion angular distribution (ESDIAD)

measurements, and work function change ($\Delta\phi$) measurements to study ammonia adsorption on Ru(001), and also concluded that for low adsorption temperatures (approximately 80 K) ammonia adsorption is completely reversible. They showed that large ammonia exposures at 80 K lead to ammonia desorption over a broad temperature range, with monolayer desorption between approximately 150 and 350 K (and displaying weak maxima near 180 and 270 K), desorption of second-layer ammonia at 140 K, and multilayer desorption in a sharp peak at 115 K. Both ESDIAD and $\Delta\phi$ measurements supported the expected model of bonding for monolayer ammonia, namely via the lone pair of electrons on the nitrogen atom. The saturation monolayer coverage of chemisorbed ammonia was estimated to be approximately 0.25 monolayer (or 3.9×10^{14} molecule cm^{-2}) based primarily on LEED data and in analogy to previous studies of ammonia adsorption on Pt(111)[5] and Ni(110).[11] It was also suggested that ammonia adsorbs in threefold hollow sites on this surface.

Electron energy loss spectroscopy has been used previously to study ammonia adsorption on Pt(111),[3] Ni(111),[9] Ni(110),[9] Ag(110),[1] Ag(311),[2] and Fe(110).[28] In all cases, ammonia adsorbs molecularly at low temperatures (approximately 80–120 K) and only on Fe(110)[28] and Ni(110)[11] does significant dissociation occur as the surface is annealed. The EEL spectra of ammonia adsorbed in the monolayer are dominated in most cases by a strong loss feature occurring between approximately 1050 and 1170 cm^{-1}, which is due to the NH_3 symmetric deformation mode. Considerably weaker loss features occur in the frequency ranges of 1580–1650, 3200–3320, and 3340–3400 cm^{-1}, which are due, respectively, to the NH_3 asymmetric (degenerate) deformation, symmetric stretch, and asymmetric (degener-

ate) stretch. The characteristic frequency ranges for an NH_3 rocking mode and the frustrated translation of the ammonia perpendicular to the surface [i.e., the metal–nitrogen stretch, $\nu(M-NH_3) \equiv T_z$] are much less certain, however. The NH_3 rocking mode has not been identified previously for chemisorbed ammonia on any metal surface, although a frequency of 720 cm^{-1} has been reported for second-layer ammonia on Pt(111).[3] The $\nu(M-NH_3)$ mode has been identified on only three of the metal surfaces studied, and there is a large variation in the reported values: 340 cm^{-1} on Fe(110),[28] 470 cm^{-1} on Ag(311),[2] and 570 cm^{-1} on Ni(110).[9] It was partly in the hope of identifying these latter two modes clearly that we undertook this study of ammonia on Ru(001). As in several of the previous studies, we have measured EEL spectra of both NH_3 and ND_3 in order to confirm our mode assignments. Several of the earlier studies have also characterized second-layer and multilayer ammonia vibrationally. As might be expected, the formation of a second-layer, molecularly adsorbed state (desorbing between 120 and 160 K) and of a multilayer state (desorbing between 110 and 120 K) appears to be a general feature of ammonia adsorption on these metal surfaces, and both the second layers and the multilayers show some common EEL features on all surfaces on which they have been studied.

II. EXPERIMENTAL DETAILS

The EEL spectrometer used in this study, and the UHV chamber housing it, have been described in detail elsewhere.[49] The spectrometer employs 180° hemispheres as the energy dispersing elements in both the monochromator and the analyzer. The analyzer is rotatable within the scattering plane to allow off-specular EEL spectra to be measured. Typical parameters used in obtaining the EEL spectra presented here were the following: energy of the electron beam incident on the surface, 4 eV; resolution (full width at half-maximum of the elastically scattered beam), 50–85 cm^{-1}; count rate in the elastic peak, $1-3 \times 10^5$ counts per second; and (fixed) angle of incidence of the electron beam, approximately 60° with respect to the surface normal. All EEL spectra were collected in the specular direction, except as noted. All EEL spectra were recorded with the surface at a temperature of 80–100 K, after annealing to indicated temperatures.

The stainless steel UHV chamber was pumped by a 220 l s^{-1} Varian noble vacion pump and a titanium sublimation pump. Typical working pressures during experiments were in the range of $1-3 \times 10^{-10}$ Torr. The Ru(001) crystal could be cooled to 80 K using liquid nitrogen, and could be heated resistively to temperatures exceeding 1600 K. After each experiment, the surface was heated to 1000 K prior to the next exposure in order to desorb any trace amounts of atomic nitrogen[50] that might be formed as the result of ammonia decomposition at defects or the cracking of ammonia on hot filaments, as well as any residual hydrogen[51] and carbon monoxide[52] adsorbed from the chamber background. Periodic, extensive cleaning of the surface was accomplished both by argon ion sputtering and annealing the crystal in a background of oxygen. Surface cleanliness was verified by EELS, and by H$_2$[51] and CO[52] thermal desorption spectra

that are characteristic of the clean surface.

The UHV chamber also contains a quadrupole mass spectrometer for performing TDMS experiments, and for the analysis both of background gases and of the purity of the ammonia that was admitted into the chamber. The thermal desorption measurements performed in connection with this work were obtained with a heating rate of approximately 8 K s^{-1}. The NH_3 used in these studies was obtained from Matheson (99.99% reported purity) and was purified by several freeze–pump–thaw cycles. The NH_3 exposures were performed by backfilling the UHV chamber through a leak valve, and the purity of the NH_3 was verified in situ using mass spectrometry. The ND_3 was obtained from MSD isotopes (99 at. % D). Due to H/D exchange of the deuterated ammonia either on the walls of the UHV chamber or in the stainless steel leak lines, ND_3 could not be admitted into the chamber cleanly through a leak valve and was therefore admitted into the chamber via a directional beam doser consisting of a microcapillary array. The purity of the ND_3 adsorbed on the surface was best monitored by comparing the integrated intensities of the ND and NH stretching vibrations measured in subsequent EEL spectra. All exposures were effected at a surface temperature of 80 K, except as noted.

III. RESULTS

A. Thermal desorption mass spectrometry

Since a detailed study of the thermal desorption of ammonia from Ru(001) has already been carried out,[21] this subject was investigated only briefly, primarily to determine the appropriate ammonia exposures and annealing temperatures to obtain EEL spectra characteristic of multilayer, second-layer, and (various coverages of) monolayer ammonia. In reasonable agreement with the previous results, we detect the desorption of second-layer ammonia at 130 K for exposures in excess of approximately 1 L(1 L $\equiv$ 1 Langmuir $\equiv 10^{-6}$ Torr s), and the desorption of multilayer ammonia at 115 K for exposures exceeding approximately 2 L. While the two monolayer desorption maxima were not well resolved using our apparatus, our EELS results (cf. Sec. III B) indicated that monolayer ammonia desorbed between approximately 150 and 350 K. This is also in good agreement with the previous results.

The possibility that some of the ammonia dissociates rather than desorbs as the surface is annealed was investigated briefly using H$_2$ thermal desorption. The H$_2$ thermal desorption spectra that were measured following saturation ammonia exposures were compared to those obtained following saturation hydrogen exposures on Ru(001). This allowed the maximum possible amount of ammonia that dissociates to be estimated by using the known saturation coverage of hydrogen adatoms (approximately 0.85 monolayer) on Ru(001).[51] The amount of hydrogen adatoms that desorbed was never greater than 0.03 monolayer, which corresponds at most to 0.01 monolayer of NH_3. This could correspond to the decomposition of a small amount of ammonia at defect sites. However, such a small amount of hydrogen desorption could also result from the adsorption of hydrogen from the residual gas or from a small hydrogen impurity in
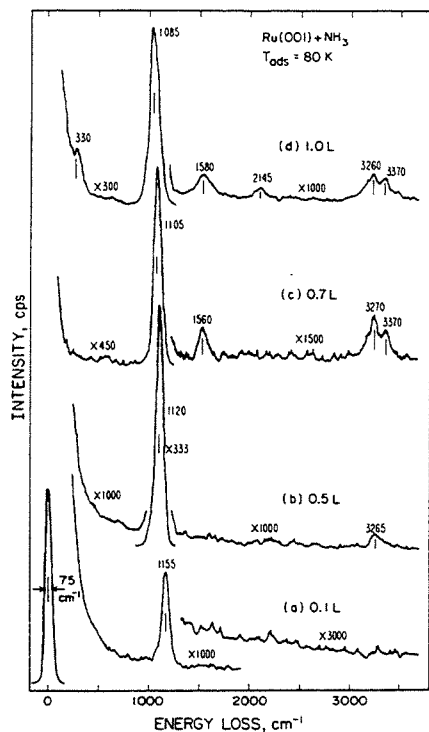
80

FIG. 1. The EEL spectra that result following several exposures of NH₃ to the Ru(001) surface at 80 K. (In the case of the 0.7 L exposure, the surface temperature was closer to 90 K, and the elastic peak count rate was only 2×10⁴.)

the ammonia sample. Thus, we are in complete agreement with the previous conclusion[18,21] that ammonia decomposition is negligible on Ru(001) following ammonia adsorption at 80–100 K.

B. Electron energy loss spectroscopy

Electron energy loss spectra for several coverages of ammonia on Ru(001) at 80–90 K are shown in Fig. 1. The exposures involved correspond to submonolayer coverages; no second-layer or multilayer ammonia is present in any of these spectra with the exception of spectrum (d), where a very small amount of second-layer ammonia is probably present. Following a 0.1 L ammonia exposure, only a single loss feature is resolved at 1155 cm⁻¹. For larger ammonia exposures, this loss feature shifts downward in frequency, reaching approximately 1085 cm⁻¹ following a 1 L exposure. It is by far the most intense loss feature for all submonolayer coverages, and is identified easily as being due to $\delta_s(NH_3)$, the symmetric deformation mode of molecularly adsorbed ammonia. At all coverages, it is strongly upshifted in frequency from its gas phase value of 950 cm⁻¹.[53] Following a 0.5 L exposure, a second loss feature is observed at 3265 cm⁻¹ due to the (unresolved) symmetric and asymmetric NH₃ stretching modes. Increasing the exposure to 0.7 L allows these two modes to be resolved at 3270 and 3370 cm⁻¹, respectively, and another loss feature becomes apparent at 1560 cm⁻¹ which is assigned as the asymmetric deformation mode of ammonia, $\delta_a(NH_3)$. Following a 1 L exposure all of these loss features are again resolved, and a very weak loss feature appears at 2145 cm⁻¹ which is assigned as the overtone of the NH₃ symmetric deformation. Another loss feature appears at 330 cm⁻¹. While this feature may derive some intensity from the very weak frustrated translational

TABLE I. Vibrational frequencies (in cm⁻¹) and mode assignments for gas phase ammonia, and for chemisorbed ammonia on several metal surfaces.

Mode	NH₃(g) (Ref. 53)	ND₃(g) (Ref. 53)	Ru(001) NH₃ (This work)	Ru(001) ND₃ (This work)	Pt(111) (Ref. 3)	Ni(111) (Ref. 9)	Ni(110) (Ref. 9)	Fe(110) (Ref. 28)	Ag(110) (Ref. 1)	Ag(311) (Ref. 2)
$\nu_a(NH_3)$	3414	2556	3370	2515	3340	3360	3350	3370	3390	
$\nu_s(NH_3)$	3337	2420	3260	2335	3240	3270	3200	3290		3410
$\delta_a(NH_3)$	1628	1191	1580	1165	1600	1580	1580	1640	3320	
$\delta_s(NH_3)$	950	747	1070–	835–	1140	1140	1120	1105–	1640	1648
			1160	910				1170	1050	1100
$\rho(NH_3)$	⋯	⋯	625ᵃ	480ᵃ	n.o.ᵇ	n.o.	n.o.	n.o.	n.o.	n.o.
$\nu(M-NH_3)$	⋯	⋯	340ᵃ	350ᵃ	n.o.	n.o.	570	340	n.o.	470

ᵃ Generally observed only in off-specular EEL spectra.
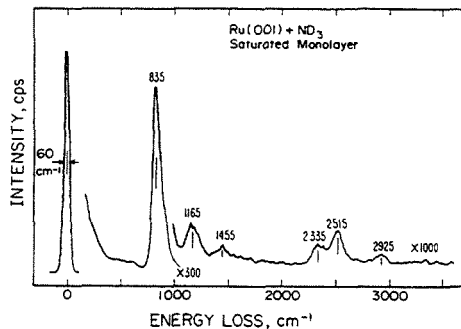ᵇ s = symmetric; a = asymmetric; n.o. = not observed.

FIG. 2. The EEL spectrum that results after a Ru(001) surface with condensed multilayers of ND_3 is annealed to 150 K. This spectrum is characteristic of monolayer ND_3.

mode (normal to the surface) of the chemisorbed ammonia (cf. Fig. 3), it is most likely due primarily to the presence of a very small amount of second-layer ammonia, which exhibits an intense loss feature due to a librational mode at 360 cm^{-1} (cf. Fig. 6 and Table II). The vibrational frequencies of chemisorbed ammonia on Ru(001) are summarized in Table I, and compared to those of gas phase ammonia,[53] and of ammonia chemisorbed on several other single crystalline metal surfaces. (Information is also included in this table that is derived from off-specular data, cf. Fig. 3.) It should be noted that while the weak loss features due to δ_a(NH$_3$), v_s(NH$_3$), and v_a(NH$_3$) occasionally were found to have frequencies differing by as much as $\pm$ 40 cm^{-1} from the average values listed in Table I, they showed no consistent frequency shifts as a function of coverage. Although such shifts would be difficult to detect due to the low intensities of these loss features, all of these features could usually be detected in off-specular spectra following exposures as low as 0.5 L.

A typical EEL spectrum of a saturated monolayer of ND_3 on Ru(001) is shown in Fig. 2. The surface was prepared by exposing the Ru(001) crystal at 100 K to approximately 30 L ND_3, followed by annealing to 150 K to remove multilayer and second-layer ND_3. The intense δ_s(ND$_3$) mode occurs at 835 cm^{-1}. As in the case of δ_s(NH$_3$), the frequency of this mode was found to shift up with decreasing coverage, and it occurred near 910 cm^{-1} in the low coverage limit. The δ_a(ND$_3$), v_s(ND$_3$), and v_a(ND$_3$) modes occur at frequencies of 1165, 2335, and 2515 cm^{-1}, respectively. The frequencies of these modes are also listed in Table I, and the observed frequency shifts upon deuteration clearly support the assignments. A very weak loss feature is observed at 1455 cm^{-1} in Fig. 2. A similar loss feature was observed in the EEL spectrum of second-layer ND_3 on Pt(111) and was attributed to δ_a(ND$_2$H) of a small ND_2H impurity.[3] The slight asymmetry on the high energy side of the δ_s(ND$_3$) loss feature could also be due to the presence of a small amount of ND_2H. The weak loss feature at 2930 cm^{-1} is most likely due to v(CH) of a small hydrocarbon impurity.[54]

Off-specular EEL spectra of both NH$_3$ and ND$_3$ al-

lowed two additional loss features to be resolved clearly in the low-frequency region. Figure 3 shows EEL spectra of nearly saturated monolayers of (a) NH$_3$ and (b) ND$_3$ obtained with the analyzer rotated approximately 5° off-specular (towards the surface normal). In addition to the loss features observed in specular EEL spectra, Fig. 3(a) shows features at 625 and 340 cm^{-1}, and Fig. 3(b) shows features at 480 and 350 cm^{-1}. Based on the observed frequency shifts and a comparison to vibrational data for metal–amine compounds (see Sec. IV A), the loss feature at 625(480) cm^{-1} is assigned to the NH$_3$(ND$_3$) rocking mode ρ(NH$_3$) and the loss feature at 340(350) cm^{-1} is assigned to the frustrated translation of the ammonia perpendicular to the surface v(Ru–NH$_3$). Both of these modes are absent in gas phase ammonia, where the "rock" corresponds to a free rotation and the "frustrated translation" to a free translation of the molecule. The low intensity of the v(Ru–NH$_3$) mode is consistent with previous results for ammonia adsorption on hexagonally close-packed metal surfaces, in which no metal–nitrogen stretching mode was resolved.[3,9] Due to the low intensities of the ρ(NH$_3$) and v(Ru–NH$_3$) loss features, it is impossible to say whether or not these modes undergo frequency shifts as a function of coverage. Note that in the off-specular EEL spectra presented here the δ_s(NH$_3$) [δ_s(ND$_3$)] loss feature has decreased greatly in intensity relative to the other loss features of chemisorbed ammonia. This indicates that this mode is strongly dipole enhanced in specular EEL spectra, while the remaining modes of chemisorbed ammonia are primarily impact excited.[55] It should be noted that the ρ(NH$_3$) mode was occasionally observed as a very weak shoulder in specular EEL spectra, near 650 cm^{-1} for NH$_3$ and near 500 cm^{-1} for ND$_3$. Indeed, such shoulders are barely visible in Figs. 1(d) and 2, but the frequency cannot be assigned accurately based on these spectra.
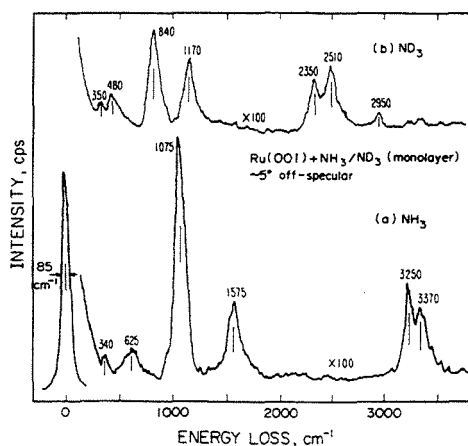

FIG. 3. Off-specular EEL spectra of monolayer (a) NH$_3$ and (b) ND$_3$ on Ru(001). Prior to spectral collection, the surface was annealed to 150 K to remove any second-layer ammonia.
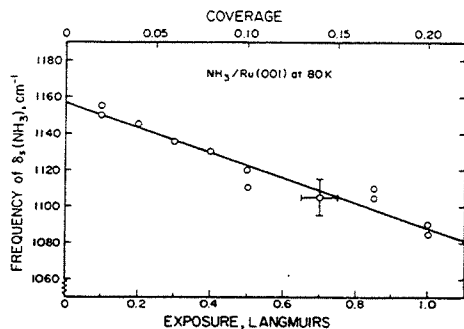
FIG. 4. The frequency of the $\delta_s(NH_3)$ mode of chemisorbed ammonia on Ru(001) as a function of ammonia coverage. The approximate coverages given are relative to the surface concentration of ruthenium atoms, which is 1.57×10^{15} cm^{-2}, and they are based on the assumption that the saturation (monolayer) ammonia coverage is 0.25.
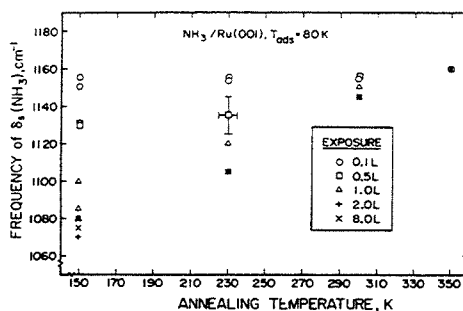

FIG. 5. The frequency of the $\delta_s(NH_3)$ mode of chemisorbed ammonia on Ru(001) as a function of annealing temperature for several initial exposures.

Figure 4 shows the variation in the frequency of the symmetric deformation mode of ammonia adsorbed on Ru(001) at 80 K as a function of the ammonia exposure. The exposure of 1 L corresponds to the coverage where the second-layer thermal desorption feature just begins to appear. However, this coverage does not correspond to monolayer saturation because the second layer begins to form before the monolayer is saturated[21]; it is estimated that this exposure corresponds to approximately 80% of monolayer saturation or an absolute coverage of approximately 0.2.[5,6] Note that the assumption of a constant probability of adsorption, in agreement with the results of Benndorf and Madey[21] and as expected for NH$_3$ at 80 K given that ammonia multilayers condense at this temperature, means that the coverages are directly proportional to the ammonia exposure. The frequency of the $\delta_s(NH_3)$ mode decreases monotonically with increasing coverage, from approximately 1155 cm^{-1} following a 0.1 L NH$_3$ exposure. The frequency decrease is very nearly linear with coverage, although there may be a slight decrease in the absolute value of the slope at high coverages. A linear least-squares fit to the data yields

$$\delta_s(NH_3) = -69.6\epsilon + 1157, \qquad (1)$$

where $\delta_s(NH_3)$ is the frequency of the NH$_3$ symmetric deformation mode in cm^{-1}, and ϵ is the exposure in Langmuirs.

Figure 5 shows the variation with annealing temperature of the frequency of the symmetric deformation mode of ammonia adsorbed on Ru(001) for a number of different ammonia exposures at 80 K. Following all exposures, the surface was annealed first to 150 K to be certain that only monolayer ammonia was present. It may be seen by comparison to Fig. 4 that annealing from 80 to 150 K generally did not change the frequency of $\delta_s(NH_3)$ by more than 10 cm^{-1} for exposures of 1 L or less. Following a 0.1 L ammonia exposure, the frequency of $\delta_s(NH_3)$ is nearly constant at 1150–1160 cm^{-1} regardless of annealing temperature. This is consistent with the fact that the coverage is not

changing for annealing temperatures between 80 and 300 K: for such a low exposure (i.e., coverage) the ammonia desorbs only in a single peak near 315 K.[21] On the other hand, the exposures of 2.0 and 8.0 L correspond to exposures well in excess of monolayer saturation, and annealing the surface to 150 K in each case produces a saturated monolayer of ammonia. Thus, the measured frequencies in these two cases should be the same for annealing temperatures of 150 K and greater, and this is found to be true within experimental error (± 10 cm^{-1}). The measured frequencies increase markedly as the surface is annealed from 150 to 230 and 300 K, because for a saturated monolayer of ammonia, significant molecular desorption occurs in these temperature ranges.[21] This results in a decrease in the coverage and thus an increase in the symmetric deformation frequency, as would be expected from an inspection of Fig. 4. For initial exposures of 0.5 and 1.0 L, the measured frequencies for any given annealing temperature fall between those obtained following 0.1 L or saturation exposures, and also increase (though less dramatically than for saturation exposures) with increasing annealing temperature. These results are all consistent with the $\delta_s(NH_3)$ frequency being a function of ammonia coverage only; the annealing temperature appears to have no effect other than to change the coverage. It should be noted that the two data points obtained following annealing to 350 K correspond to trivial amounts ($\lesssim 0.01$ monolayer) of ammonia readsorbed from the chamber background, since the thermal desorption of ammonia from Ru(001) is complete between 300 and 350 K. The $\delta_s(NH_3)$ frequency of 1160 cm^{-1} thus corresponds to the zero-coverage limit for ammonia on Ru(001), in agreement with the data of Fig. 4 and Eq. (1).

Electron energy loss spectra of second-layer NH$_3$ and ND$_3$ on Ru(001) are shown in Fig. 6, and the observed frequencies are compared to those of second-layer ammonia on other metal surfaces in Table II. The EEL spectra were obtained after the Ru(001) surface at 85 K was exposed to large fluences of NH$_3$ and ND$_3$, followed by annealing to 120 K to remove multilayer ammonia. The loss features due to $\delta_s(NH_3)$, $\delta_a(NH_3)$, $\nu_s(NH_3)$, and $\nu_a(NH_3)$ are assigned easily as for monolayer ammonia. The $\delta_s(NH_3)$ loss feature
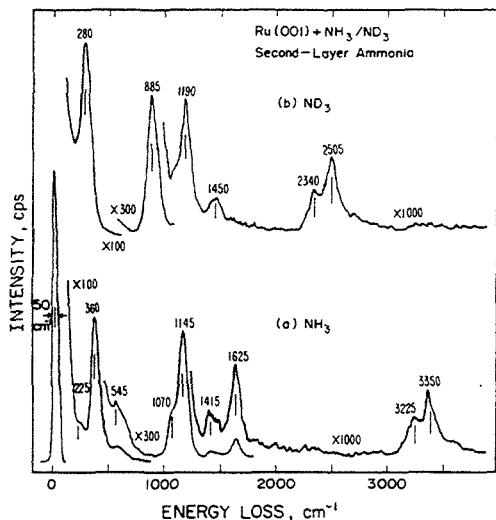
FIG. 6. The EEL spectra that result when a Ru(001) surface with condensed multilayers of (a) NH_3 and (b) ND_3 is annealed to 120 K. These spectra are characteristic of second-layer ammonia.

of second-layer NH_3 at 1145 cm^{-1} shows a pronounced shoulder at 1070 cm^{-1}, which is due to the partially screened $\delta_s(NH_3)$ loss feature of monolayer NH_3. The corresponding shoulder in the case of ND_3 is not so well resolved because the peak frequencies are closer together (i.e., approximately 50 rather than 75 cm^{-1} splitting). The spectrum of NH_3 (ND_3) contains an intense mode at 360 (280) cm^{-1} assigned to the NH_3 twisting mode $\tau(NH_3)$ (equivalent to the frustrated librational mode R_{xy}). Note that this mode is not

observed for monolayer ammonia because in that case it corresponds to a free rotation about the ruthenium–nitrogen bond. Evidence for this free rotation in the monolayer has been obtained from ESDIAD data.[21] This rotation is hindered in the second layer due to hydrogen bonding of the second-layer ammonia molecules to the monolayer ammonia. The EEL spectrum of Fig. 6(a) also shows loss features at 545 and 225 cm^{-1} which we tentatively assign, respectively, to an NH_3 rocking mode and the frustrated translation (perpendicular to the surface) T_z of the second-layer ammonia. The corresponding loss features are not well resolved in the case of ND_3 due to overlap with the $\tau(ND_3)$ loss feature at 280 cm^{-1}. Both spectra of Fig. 6 show a weak loss feature near 1400 cm^{-1}, the identity of which is uncertain. As stated previously, a similar loss feature has been attributed to $\delta_a(ND_2H)$ of an ND_2H impurity in the case of second-layer ND_3 on Pt(111).[3] In the case of NH_3, the 1415 cm^{-1} loss feature is probably a combination band (i.e., 360 + 1070 and/or 1145).[1,3,28] We can think of no likely impurity that would give rise to a loss feature in this frequency range; $\delta(H_2O)$ of water occurs at the considerably higher frequency of 1560 cm^{-1}.[57]

Figure 7 shows EEL spectra of (a) NH_3 and (b) ND_3 multilayers on Ru(001), and the vibrational frequencies and their assignments are listed in Table III along with data for solid ammonia and for NH_3 multilayers on other metal surfaces. Both of the EEL spectra in Fig. 7 were measured following ammonia exposures of approximately 30 L. The loss features due to the $\nu_s(NH_3)$, $\nu_a(NH_3)$, $\delta_s(NH_3)$, and $\delta_a(NH_3)$ modes are again assigned in a straightforward manner. Both spectra also show a weak loss feature due to the $\delta_s(NH_3)$ overtone/double loss. A strong loss feature at 200 cm^{-1} in both cases corresponds to an ammonia lattice mode (i.e., a frustrated translation of the ammonia molecules within the multilayers). Two strong librational modes are observed, one at 540 (420) cm^{-1} and the other a shoul-

TABLE II. Vibrational frequencies (in cm^{-1}) and mode assignments for second-layer NH_3 and ND_3 on Ru(001), and for second-layer NH_3 on several other metal surfaces.

	Ru(001)		Pt(111)	Ag(110)	Ni(110)	Ag(311)
Mode	NH_3 (This work)	ND_3	(Ref. 3)	(Ref. 1)	(Ref. 9)	(Ref. 2)
$\tau(NH_3)^a$	360	280	350	340	360	260
$\rho(NH_3)$	545	n.o.[b]	720	n.o.[c]	n.o.	n.o.
$\delta_s(NH_3)$	1145	885	1190	1100	1110	1100
$\delta_a(NH_3)$	1625	1190	1630	1630	1630	1650
$\nu_s(NH_3)$	3225	2340	3150	3320	3200	
						3410
$\nu_a(NH_3)$	3350	2505	3320	3390	3340	
T_z	225	n.o.	n.o.	n.o.	n.o.	n.o.

[a] This mode is also referred to in the literature as R_{xy} ($\equiv$ rotation about an axis normal to the surface), or simply as ν_t (a "frustrated libration"), although the latter designation alone is ambiguous.
[b] In some EEL spectra, a shoulder was present at approximately 450 cm^{-1} that might be assigned to $\rho(ND_3)$.
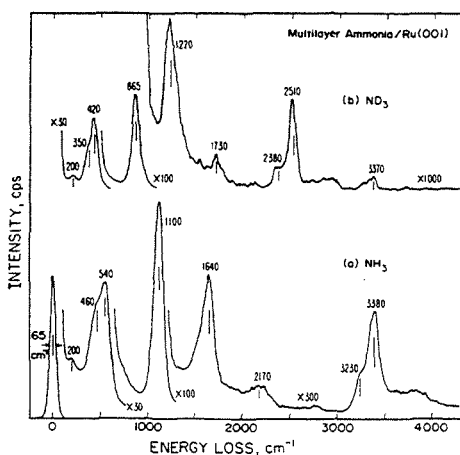[c] s = symmetric; a = asymmetric; n.o. = not observed.

FIG. 7. The EEL spectra of condensed multilayers of (a) NH_3 and (b) ND_3 on Ru(001). The exposures were approximately 30 L at a surface temperature of 85 K.

TABLE III. Vibrational frequencies (in cm^{-1}) and mode assignments for solid ammonia, and for ammonia multilayers on several metal surfaces.

Mode	Solid ammonia		Ru(001)		Pt(111)	Ag(110)	Ag(311)
	NH$_3$ (Ref. 58)[a]	ND$_3$ (Ref. 58)[a]	NH$_3$ (This work)	ND$_3$ (This work)	NH$_3$ (Ref. 3)	NH$_3$ (Ref. 1)	NH$_3$ (Ref. 2)
ν_t[b]	138–184	132–174	200	200	n.o.	140	n.o.
ν_l[c]	325–386	242–312	460	350			
					410	400	430
ν_l[c]	412–462	315–406	540	420			
δ_s(NH$_3$)	1057–1080	815–836	1100	865	1120	1070	1150
δ_a(NH$_3$)	1630–1679	1183–1217	1640	1220	1640	1630	1570
ν_s(NH$_3$)	3160–3330	2318–2336	3230	2380	n.o.[d]	3320	n.o.
ν_a(NH$_3$)	3370–3378	2505–2511	3380	2520	3320	3380	n.o.

[a] A range of values is given for each frequency of solid NH$_3$ and ND$_3$, based on several IR and Raman studies at temperatures ranging from 18 to 151 K. In some studies, more than one frequency was observed due to crystal splitting.
[b] $\nu_t \equiv$ frustrated translation or lattice mode.
[c] $\nu_l \equiv$ frustrated libration. Since there is some confusion over the assignments of these modes in the literature, we do not attempt to assign them to specific librations.
[d] s = symmetric; a = asymmetric; n.o. = not observed.

der at 460 (350) cm^{-1}. These frequencies are somewhat higher than those reported previously for both ammonia multilayers and solid ammonia,[58] although we note that the frequencies were lower if only a few layers of ammonia were present (e.g., approximately 370 and 450 cm^{-1} following an 8 L NH$_3$ exposure). Both spectra show low intensity tails on the high energy side of the ν_a(NH$_3$) loss features, the origins of which are not entirely clear, although they may be due to combination bands of ν_a(NH$_3$) [ν_a(ND$_3$)] and the librational and/or frustrated translational modes. The peak at 3370 cm^{-1} in the ND$_3$ multilayer spectrum is due primarily to the combination band δ_s(ND$_3$) + ν_a(ND$_3$), although ν(NH) modes due to contamination of the ND$_3$ sample may also contribute to its intensity. A loss feature of similar intensity was observed at 4480 cm^{-1} in NH$_3$ multilayer spectra that were scanned to higher loss energy, and this peak is assigned as δ_s(NH$_3$) + ν_a(NH$_3$).

IV. DISCUSSION

A. Comparison to ammonia on other metal surfaces and in coordination compounds

The EEL spectra that have been obtained for ammonia adsorbed on Ru(001) show strong similarities to those obtained when ammonia is adsorbed on other hexagonally close-packed metal surfaces [i.e., Pt(111)[3] and Ni(111)[9]], and on the pseudo-close-packed Fe(110) surface.[28] On the more highly corrugated surfaces, the EELS data currently available do not provide a consistent picture. On Ag(110),[1] the EEL spectra of adsorbed ammonia are very similar to the spectra obtained for ammonia on the more densely packed surfaces, with the δ_s(NH$_3$) loss feature at 1050 cm^{-1} being by far the most intense feature in the entire spectrum. The EEL spectra of ammonia adsorbed on Ag(311) are also similar, although in this case a mode of moderate intensity was

observed at 470 cm^{-1} that was assigned as ν(Ag–NH$_3$).[2] The EEL spectra of ammonia on Ni(110) are surprisingly different, with δ_s(NH$_3$), δ_a(NH$_3$), and ν_a(NH$_3$) loss features of comparable intensity and an additional strong mode at 570 cm^{-1} that was assigned as ν(Ni–NH$_3$).[9] However, this mode assignment does not appear to have been verified by obtaining EEL spectra of chemisorbed ND$_3$ on this surface. Despite the lack of a consistent pattern of mode intensities on the highly corrugated surfaces, the mode frequencies of δ_s(NH$_3$), δ_a(NH$_3$), ν_a(NH$_3$), and ν_a(NH$_3$) are quite similar on all of the metal surfaces where ammonia chemisorption has been studied by EELS. This fact, along with the consistent pattern of mode intensities on Ru(001), Pt(111), Ni(111), Fe(110), and Ag(110), suggests some useful comparisons to infrared data for metal compounds containing ammonia ligands.

Table IV provides a compilation of vibrational data for ammonia adsorbed on metal surfaces and in four different classes of metal–ammonia compounds. The data for the metal compounds show some interesting trends with regard to the charge (both formal and actual) on the metal atom. Note that the "electron richness" of the metal atoms in these compounds is expected to follow the order

$$M(NH_3)_6^{2+} > M(NH_3)_4^{2+} > M(NH_3)_6^{3+}.$$

The frequency of the δ_s(NH$_3$) mode is very charge sensitive and shifts upward with increasing charge on the metal atom, having average values of 1158 cm^{-1} in the M(NH$_3$)$_6^{2+}$ compounds, 1333 cm^{-1} in the M(NH$_3$)$_6^{3+}$ compounds, and intermediate average values in the case of the M(NH$_3$)$_4^{2+}$ compounds. The changes observed in the frequency of this mode when the metal atom is changed and the charge held constant are minor compared to those resulting from charge changes.[59] The ρ(NH$_3$) and ν(M–NH$_3$) modes are also charge sensitive and show marked upshifts in frequency in

TABLE IV. Vibrational frequencies (in cm^{-1}) for various modes of ammonia adsorbed on Ru(001) and other metal surfaces (Refs. 1–3, 9, and 28), and in various types of inorganic compounds (Ref. 64). The first number given in each case is the average frequency for the specific mode in a certain type of compound, and is followed in parentheses by the number of compounds that was used in calculating the average. Below this, the range (low and high extremes) is listed for the same mode.

Mode	Ru(001) (This work)	Other metal surfaces[a]	$M(NH_3)_6^{3+}$ (Ref. 64)[b]	$M(NH_3)_6^{2+}$ (Ref. 64)[c]	$M(NH_3)_4^{2+}$ tetrahedral (Ref. 64)[d]	$M(NH_3)_4^{2+}$ square planar (Ref. 64)[e]
$\nu_a(NH_3)$[g]	3370	3363(5) 3340– 3400	3269(3) 3240– 3310	3336(7) 3300– 3353	3316(3) 3233– 3354	3272(3) 3236– 3327
$\nu_s(NH_3)$	3260	3264(5) 3200– 3320	3183(3) 3130– 3250	3200(7) 3160– 3250	3226(3) 3150– 3267	3165(3) 3156– 3170
$\delta_a(NH_3)$	1580	1615(6) 1580– 1648	1616(6) 1587– 1630	1601(8) 1585– 1610	1608(3) 1596– 1617	1612(3) 1563– 1669
$\delta_s(NH_3)$	1115 1070– 1160	1119(6)[f] 1050– 1170	1333(6) 1290– 1368	1158(8) 1091– 1220	1227(3) 1176– 1253	1298(3) 1279– 1325
$\rho(NH_3)$	625	Not observed previously	806(6) 748– 857	656(8) 592– 769	683(3) 670– 693	807(3) 735– 849
$\nu(M-NH_3)$ (A_1)	340	Reported values of 340,470, 570	488(6) 462– 527	332(6) 298– 370	409(3) 370– 432	481(3) 420– 524

[a] Data are for Ag(110), Ag(311), Pt(111), Ni(111), Ni(110), and Fe(110).
[b] Data are for M = Cr, Ru, Os, Co, Rh, and Ir.
[c] Data are for M = Mg, Mn, Fe, Ru, Co, Ni, Zn, and Cd.
[d] Data are for M = Co, Zn, and Cd.
[e] Data are for M = Pd, Pt, and Cu.
[f] In the case of Fe(110), where $\delta_s(NH_3)$ was reported to shift in frequency as a function of coverage (Ref. 28), an average value was used as the characteristic frequency of chemisorbed ammonia.
[g] s = symmetric; a = asymmetric; n.o. = not observed.

going from the $M(NH_3)_6^{2+}$ to the $M(NH_3)_6^{3+}$ metal compounds, although in these cases there is somewhat larger overlap between the frequency ranges for these compounds and the $M(NH_3)_4^{2+}$ compounds. The $\nu_a(NH_3)$ mode is slightly charge sensitive, and shifts upward in frequency with decreasing charge on the metal atom. The $\nu_s(NH_3)$ and $\delta_a(NH_3)$ modes are not sensitive to the oxidation state of the metal atom and show no consistent frequency shifts.

Comparing the EELS data for ammonia on metal surfaces to the data for coordination compounds reveals immediately that the $\delta_s(NH_3)$ frequencies observed on surfaces are very similar to those observed in the $M(NH_3)_6^{2+}$ compounds, although the average frequency of 1119 cm^{-1} and the high and low extremes are all 40–50 cm^{-1} lower for the adsorbed ammonia. It is expected that the $\delta_s(NH_3)$ frequencies would be somewhat lower on metal surfaces, since the formal oxidation state of the surface metal atoms is zero. Thus, the observed frequencies of this mode for ammonia adsorbed on a number of metal surfaces appear to correlate well with the IR data for coordination compounds. The same is true in the case of the $\nu_a(NH_3)$ mode, the average frequency of which is higher on surfaces than in the coordination compounds. However, this is of only minor significance because this mode is only slightly charge sensitive, and due to its low intensity and overlap with the $\nu_s(NH_3)$ loss

feature, its frequency on any given surface cannot be determined as accurately as that of $\delta_s(NH_3)$.

The fact that the $\delta_s(NH_3)$ frequencies of chemisorbed ammonia are similar to those of $M(NH_3)_6^{2+}$ compounds suggest that the frequencies of the other two vibrational modes that are strongly charge sensitive, $\rho(NH_3)$ and $\nu(M–NH_3)$, might also be similar in these two cases. While very few data for these two vibrational modes of chemisorbed ammonia are available, our results provide strong support for this proposition. The measured $\rho(NH_3)$ frequency of 625 cm^{-1} is well within the range of 592–769 cm^{-1} reported for the $M(NH_3)_6^{2+}$ compounds, and is slightly lower than the average value of 656 cm^{-1}, just as our measured average $\delta_s(NH_3)$ frequency of 1115 cm^{-1} is slightly lower than the average value of 1158 cm^{-1} in these compounds. The $\rho(NH_3)$ frequencies of the $M(NH_3)_6^{3+}$ compounds are considerably higher, ranging from 748 to 857 cm^{-1}.

In the case of $\nu(M–NH_3)$, the available data for ammonia on metal surfaces present a more complex picture, but our measured frequency of 340 cm^{-1} is in good agreement with data for the $M(NH_3)_6^{2+}$ compounds and identical to the value reported for ammonia on the pseudo-close-packed Fe(110) surface.[28] The reported values of $\nu(M–NH_3)$ for Ag(311)[2] and Ni(110)[9] of 470 and 570 cm^{-1}, respectively, are considerably higher and similar to those observed in the

J. Chem. Phys. Vol. 88, No. 8, 15 April 1988

86

$M(NH_3)_6^{3+}$ compounds (462 to 527 cm^{-1}), even though the observed $\delta_s(NH_3)$ frequencies on both surfaces are very similar to those observed on close-packed and pseudo-close-packed surfaces and in the $M(NH_3)_6^{2+}$ compounds. While this difference is no doubt related in some way to the highly corrugated structures of the Ag(311) and Ni(110) surfaces, its exact explanation is unclear. In general, however, the comparison of the vibrational spectra of chemisorbed and coordinated ammonia appears promising, and also serves to point out the importance of obtaining off-specular spectra when EELS is used to study ammonia chemisorption.

B. Origins of the frequency shift of $\delta_s(NH_3)$: Correlation with work function data

The pronounced charge sensitivity of the $\delta_s(NH_3)$ frequency in coordination compounds also provides an explanation for the observed shift in the frequency of this mode as a function of coverage for ammonia chemisorbed on Ru(001). The work function change of Ru(001) as a function of ammonia coverage at 80 K has been studied by Benndorf and Madey,[21] and the work function was found to decrease monotonically by approximately 1.8 eV as the coverage is increased from 0 to 0.25 monolayer. The work function change is saturated only after a total ammonia coverage of approximately 0.6 monolayer, and the work function is then approximately 2.3 eV less than on the clean surface. The decrease in the work function is initially linear with coverage, but it increases slightly less rapidly with coverage above a coverage of approximately 0.15 to 0.20 monolayer, and much less rapidly above 0.25 monolayer. The work function decrease results from a net transfer of electrons from the ammonia to the ruthenium surface atoms, so that the electron richness of these surface atoms is increased as the coverage increases. The decreased "charge" on the metal atoms then leads to a lower $\delta_s(NH_3)$ frequency, just as in the coordination compounds of Table IV.

The magnitude of this charge, or the number of electrons donated to each surface metal atom by the ammonia adlayer for a given ammonia coverage, can be estimated approximately using the surface-ammonia dipole moment of 1.9 D calculated by Benndorf and Madey,[21] and assuming a surface–nitrogen bond distance of 2.15 Å.[60] This suggests that approximately 0.18 electron is transferred to the surface per adsorbed ammonia molecule. While the dipole moment of 1.9 D was based on the slope of the work function vs ammonia coverage curve in the limit of zero coverage, the curve is only slightly nonlinear below a coverage of 0.25, and a large part of this nonlinearity is probably due to the fact that some adsorption into the second layer occurs before the monolayer is completely saturated.[21] Our results showing that the frequency of $\delta_s(NH_3)$ decreases nearly linearly with coverage up to at least a coverage of approximately 80% of monolayer saturation supports this point of view, and it is therefore reasonable to assume this same dipole moment for each adsorbed ammonia molecule up to monolayer saturation. Thus, for a saturation monolayer ammonia coverage of 0.25, an average of approximately 0.045 electron is transferred to each surface ruthenium atom from the ammonia adlayer.

This interpretation of the frequency shift of $\delta_s(NH_3)$ has several important implications regarding ammonia chemisorption on Ru(001) and other metal surfaces. First, it suggests that this downshift should occur as the ammonia coverage is increased on all metal surfaces, and that the magnitude of the shift should scale approximately with the amount of charge transfer characteristic of ammonia adsorption. This hypothesis cannot yet be tested fully due to a lack of experimental data, but it is interesting to note that on Fe(110) a comparable work function decrease (approximately 2 eV)[26] and frequency shift (from 1170 to 1105 cm^{-1})[28] have been found. The Pt(111) surface exhibits a work function decrease of approximately 2.7 eV when a monolayer saturation coverage of ammonia is adsorbed.[5] While the published EEL spectra for monolayer ammonia on this surface show $\delta_s(NH_3)$ frequencies varying from at least 1170 to 1090 cm^{-1},[3] it is not clear whether there is a monotonic shift as a function of coverage. It must also be pointed out that a series of EEL spectra for various ammonia coverages on Ag(311) show no apparent shift in the frequency of this mode.[2] Work function data are not available for this surface. This interpretation suggests also that the $\delta_s(NH_3)$ frequency of ammonia chemisorbed on Ru(001) should be increased by the presence of electronegative adatoms such as oxygen, and decreased by the presence of electropositive adatoms such as alkali metals. In the case of oxygen, however, the effects of hydrogen bonding will complicate the analysis.[23]

Finally, we note that frequency shifts as a function of ammonia coverage might also be expected for the $\rho(NH_3)$ and $\nu(Ru–NH_3)$ modes of ammonia chemisorbed on Ru(001), since these modes are also charge sensitive for ammonia in coordination compounds. We cannot address this question unambiguously because the loss features due to these modes are below our limit of detectability for ammonia coverages less than approximately half of monolayer saturation. In addition, these low frequency modes are likely to be more affected than the $\delta_s(NH_3)$ mode by such effects as tilting of the ammonia at high coverages, a phenomenon which has been proposed to occur based on ESDIAD results.[21]

C. Adsorption site of NH_3 on Ru(001)

The adsorption site(s) of ammonia on metal surfaces has been the subject of some disagreement in the literature. Based on indirect evidence obtained using a variety of experimental techniques, it has been suggested that ammonia adsorbs with the nitrogen atom in threefold hollow sites on Ru(001),[21] Pt(111),[3] Ir(111),[17(a)] and Ni(111),[9] and with the nitrogen atom in the long bridging sites on the pseudo-close-packed Fe(110) surface.[26] On the other hand, the on-top site was favored for ammonia adsorption on Al(111),[31] and calculations for ammonia adsorption on Al(111)[61] and Cu(111)[62] support this model, showing the interaction between the nitrogen lone pair and the threefold hollow sites to be repulsive. The great similarities among the EEL spectra of ammonia chemisorbed on Ru(001), Pt(111),[3] Ni(111),[9] Fe(110),[28] and Ag(110)[1] suggest (but do not prove) that a common adsorption site is occupied on all of these surfaces.

For several reasons, we prefer the on-top site as the bonding site of chemisorbed ammonia on Ru(001). The primary reason is that the vibrational frequencies of adsorbed ammonia agree so well with those of ammonia ligands in hexamine compounds, which are "on-top" by definition. We would expect that the frequencies of $\rho(NH_3)$ and especially $\nu(Ru-NH_3)$ would be substantially different if bonding occurred in threefold hollow or twofold bridge sites. This hypothesis cannot be tested because *there is no example known to us in metal cluster chemistry of an ammonia ligand that occupies a threefold hollow or twofold bridging site, or any site other than an on-top site.*[63] The same is true of the closely related phosphine (PR$_3$) ligands. In fact, to our knowledge, NH$_3$, NH$_2$(NR$_2$), and NH(NR) ligands occupy only on-top, twofold bridging and threefold hollow sites, respectively, in metal cluster compounds.[63]

We note also that the Fe(110) surface contains no true threefold hollow sites, although it is possible that the pseudo-threefold sites on this surface might be sufficiently similar to true threefold sites to give rise to virtually identical EEL spectra for an adsorbed species. All of these arguments support the intuitive expectation that a strong σ-electron donor such as ammonia should adsorb on the most electron deficient site on these surfaces, namely, the on-top site.[62] While none of these points taken alone is compelling, we believe that together they provide considerable support for on-top bonding. Hopefully, additional data for ammonia adsorption on surfaces and (especially) in metal clusters will clarify this issue.

D. Second-layer and multilayer ammonia

As pointed out in Sec. III B, the EELS spectra of second-layer ammonia on Ru(001) show strong similarities to those obtained on other metal surfaces. Most notably, the strong $\tau(NH_3)$ loss feature at 350 cm^{-1} is very similar both in frequency and intensity to the corresponding loss features on Pt(111),[3] Ag(110),[1] and Ni(110).[9] Surprisingly, the corresponding loss feature on Ag(311)[2] was observed at the substantially lower frequency of 260 cm^{-1}. Nevertheless, it appears that a strong $\tau(NH_3)$ loss feature near 350 cm^{-1} is characteristic of second-layer ammonia on most surfaces and may be used as a vibrational fingerprint for the second layer. Note that the librational modes reported to date for multilayer ammonia (cf. Table III) occur at frequencies greater than 400 cm^{-1}. The intensity of the $\tau(NH_3)$ loss feature, and the fact that it is strongly attenuated in off-specular EEL spectra indicate that it is dipole enhanced and thus belongs to the totally symmetric representation of the surface/second-layer ammonia complex. This suggests that at least some of the second-layer ammonia is adsorbed with the molecular axis tilted significantly with respect to the surface normal. This is in agreement with the ESDIAD results of Benndorf and Madey,[21] who observed normal emission of H$^+$ for second-layer but not monolayer ammonia, and interpreted this in terms of tilting of the molecules within the second layer.

We note also that our $\rho(NH_3)$ frequency of second-layer ammonia of 545 cm^{-1} is substantially lower in frequency than that of 720 cm^{-1} reported for second-layer ammonia

on Pt(111).[3] The corresponding loss feature in the case of second-layer ND$_3$ on Pt(111) occurred at 570 cm^{-1}.[3] In our study, the corresponding mode in the case of ND$_3$ was not resolved unambiguously, although in some EEL spectra of second-layer ND$_3$ a shoulder was observed at approximately 450 cm^{-1}. For both of these reasons, and because this mode has not been identified in EEL spectra of second-layer ammonia on other metal surfaces, our assignment should be regarded as tentative.

The vibrational frequencies of multilayer NH$_3$ and ND$_3$ on Ru(001) are in reasonably good agreement with those of solid ammonia, although the frustrated translational and librational modes occur at slightly higher frequencies. We emphasize that even though all ammonia layers above the second are indistinguishable in thermal desorption spectra, quite large ammonia exposures were necessary in order to obtain an EEL spectrum of true ammonia multilayers, i.e., a spectrum that showed no changes in the frequencies at the various vibrational modes with increasing exposure of the surface to ammonia at 85 K. The main changes for lower exposures were in the frequencies of the librational modes, which shifted upward with increasing exposure until a total exposure of 15–20 L was reached. This would correspond, very approximately, to 15 "layers" of ammonia. It is possible that some of the previously reported librational frequencies of ammonia multilayers on metal surfaces would have been upshifted further if the exposures had been increased, and the fact that the observed librational frequencies of multilayer ammonia are in all cases higher than those of the strong librational mode of second-layer ammonia is consistent with our results.

V. CONCLUSIONS

High-resolution electron energy loss spectroscopy has been used to study the interaction of ammonia with the Ru(001) surface. The results are generally in agreement with those of previous studies of the ammonia/Ru(001) system utilizing other experimental techniques. In particular, we find no significant decomposition of ammonia following exposures to the Ru(001) surface at 80–100 K, and our EEL spectra support the desorption temperatures for multilayer, second-layer, and monolayer ammonia that have been reported previously. The principal new conclusions that may be drawn from the EELS results are the following:

(1) Monolayer ammonia on Ru(001) exhibits EEL spectra with $\delta_s(NH_3)$, $\delta_a(NH_3)$, $\nu_s(NH_3)$, and $\nu_a(NH_3)$ frequencies very similar to those of ammonia chemisorbed on other close-packed and pseudo-close-packed metal surfaces. In addition, the NH$_3$ rocking mode and the frustrated translational mode of the ammonia perpendicular to the surface are observed in off-specular EEL spectra and occur at frequencies of approximately 625 and 340 cm^{-1}, respectively. The $\rho(NH_3)$ mode has not been identified previously for chemisorbed ammonia, and the $\nu(metal-NH_3)$ mode has been identified only rarely. These results indicate the importance of obtaining off-specular spectra in EELS studies of chemisorbed ammonia.

(2) The vibrational spectra of ammonia chemisorbed on Ru(001) and other metal surfaces of similar geometry

are very similar to those of hexamine $2+$ compounds, $M(NH_3)_6^{2+}$, and agree much less well with those of $M(NH_3)_6^{3+}$ and $M(NH_3)_4^{2+}$ compounds, regardless of the type of metal atom and counter ions in the complexes. Thus, both on surfaces and in coordination compounds, the real (not formal) "oxidation state" of the metal is of paramount importance in determining the vibrational frequencies of coordinated ammonia.

(3) The intense $\delta_s(NH_3)$ mode of chemisorbed NH_3 on Ru(001) shifts down continuously and essentially linearly with increasing coverage, from 1160 cm^{-1} in the low coverage limit to 1070 cm^{-1} at monolayer saturation. This parallels the downshift of the frequency of this mode in coordination compounds as the charge on the metal atom decreases. This change can be correlated with the large decrease (~ 2 eV) in the work function of the Ru(001) surface that occurs as ammonia is adsorbed,[21] making the surface atoms, in effect, more "negatively charged."

(4) The EELS results, and the organometallic literature concerning NH_3 ligands, are more consistent with chemisorbed NH_3 bonding in on-top sites, rather than in threefold sites.

(5) The vibrational characteristics of second-layer and multilayer ammonia on Ru(001) are generally quite similar to those of second-layer and multilayer ammonia on other metal surfaces. The intense $\tau(NH_3)$ loss feature near 350 cm^{-1} appears to be a general feature of second-layer ammonia on most metal surfaces. The fact that this mode is dipolar in nature suggests a tilting of the molecular axis of the second-layer ammonia away from the surface normal, consistent with previous ESDIAD results.[21] While all layers above the second are indistinguishable in thermal desorption spectra, substantially larger coverages (i.e., approximately 15 layers) of condensed ammonia are necessary to obtain a multilayer EEL spectrum which shows no further changes in the vibrational frequencies of the various modes when additional exposures are made.

ACKNOWLEDGMENTS

[1] J. L. Gland, B. A. Sexton, and G. E. Mitchell, Surf. Sci. 115, 623 (1982).
[2] S. T. Ceyer and J. T. Yates, Jr., Surf. Sci. 155, 584 (1985).
[3] B. A. Sexton and G. E. Mitchell, Surf. Sci. 99, 523 (1980).
[4] B. A. Sexton and G. E. Mitchell, Surf. Sci. 99, 539 (1980).
[5] G. B. Fisher, Chem. Phys. Lett. 44, 683 (1981).
[6] J. L. Gland, Surf. Sci. 71, 327 (1978).
[7] J. L. Gland and V. N. Korchak, J. Catal. 53, 9 (1978).
[8] J. L. Gland and E. B. Kollin, Surf. Sci. 104, 478 (1981).
[9] G. B. Fisher and G. E. Mitchell, J. Electron Spectrosc. Relat. Phenom. 29, 253 (1983).
[10] C. W. Seabury, T. N. Rhodin, R. J. Purtell, and R. P. Merrill, Surf. Sci. 93, 117 (1980).
[11] M. Grunze, M. Golze, R. K. Driscoll, and P. A. Dowber, J. Vac. Sci. Technol. 18, 611 (1981).

[12] K. Jacobi, E. S. Jensen, T. N. Rhodin, and R. P. Merrill, Surf. Sci. 108, 397 (1981).
[13] T. E. Madey, J. E. Houston, C. W. Seabury, and T. N. Rhodin, J. Vac. Sci. Technol. 18, 476 (1981).
[14] F. P. Netzer and T. E. Madey, Phys. Rev. Lett. 47, 928 (1981).
[15] F. P. Netzer and T. E. Madey, Surf. Sci. 119, 422 (1982).
[16] M. Grunze, P. A. Dowber, and C. R. Brundle, Surf. Sci. 128, 311 (1983).
[17] (a) R. J. Purtell, R. P. Merrill, C. W. Seabury, and T. N. Rhodin, Phys. Rev. Lett. 44, 1279 (1980); (b) W. M. Kang, C. H. Li, S. Y. Tang, C. W. Seabury, K. Jacobi, T. N. Rhodin, R. J. Purtell, and R. P. Merrill, *ibid.* 47, 931 (1981).
[18] L. R. Danielson, M. J. Dresser, E. E. Donaldson, and J. T. Dickinson, Surf. Sci. 71, 599 (1978).
[19] L. R. Danielson, M. J. Dresser, E. E. Donaldson, and D. R. Sandstrom, Surf. Sci. 71, 615 (1978).
[20] T. E. Madey and J. T. Yates, Jr., in *Proceedings of the 7th International Vacuum Congr. and 3rd International Conference on Solid Surfaces*, edited by R. Dobrozemsky, F. Rüdenauer, F. P. Viehböck, and A. Breth (Vienna, 1977), p. 1183.
[21] C. Benndorf and T. E. Madey, Surf. Sci. 135, 164 (1983).
[22] C. Benndorf and T. E. Madey, Chem. Phys. Lett. 101, 59 (1983).
[23] T. E. Madey, C. Benndorf, D. L. Doering, and S. Semancik, Proc. 8th Int. Congr. Catal. 4, 51 (1984).
[24] M. Grunze, F. Bozso, G. Ertl, and M. Weiss, Appl. Surf. Sci. 1, 241 (1978).
[25] M. Drechsler, H. Hoinkes, H. Kaarmann, H. Wilsch, G. Ertl, and M. Weiss, Appl. Surf. Sci. 3, 217 (1979).
[26] M. Weiss, G. Ertl, and F. Nitschke, Appl. Surf. Sci. 3, 614 (1979).
[27] M. Grunze and G. Ertl, in Ref. 20, p. 1137.
[28] W. Erley and H. Ibach, Surf. Sci. 119, L357 (1982).
[29] K. Kishi and M. W. Roberts, Surf. Sci. 62, 252 (1977).
[30] I. D. Gay, M. Textor, R. Mason, and Y. Iwasawa, Proc. R. Soc. London Ser. A 356, 25 (1977).
[31] F. P. Netzer and T. E. Madey, Chem. Phys. Lett. 88, 315 (1982).
[32] See, for example, G. C. Bond, *Catalysis by Metals* (Academic, New York, 1962).
[33] J. R. Hall and G. A. Swile, J. Organomet. Chem. 42, 479 (1972).
[34] R. P. Shibaeva, L. P. Rozenberg, R. M. Lobkovskaya, A. E. Shilov, and G. B. Shulpin, J. Organomet. Chem. 220, 271 (1981).
[35] L. M. Vallarino and S. W. Sheargold, Inorg. Chim. Acta 36, 243 (1979).
[36] W. Rigby, J. A. McCleverty, and P. M. Maitlis, J. Chem. Soc. Dalton Trans. 1979, 382.
[37] B. P. Sullivan, J. A. Baumann, T. J. Meyer, D. J. Salmon, H. Lehmann, and A. Ludi, J. Am. Chem. Soc. 99, 7368 (1977).
[38] H. Lehmann, K. J. Schenk, G. Chapuis, and A. Ludi, J. Am. Chem. Soc. 101, 6197 (1979).
[39] D. Rehder, J. Organomet. Chem. 37, 303 (1972).
[40] J. E. Ellis and K. L. Fjare, Organomet. 1, 898 (1982).
[41] D. Sellmann, A. Brandl, and R. Endell, J. Organomet. Chem. 111, 303 (1976).
[42] M. Herberhold, F. Wehrmann, D. Neugebauer, and G. Huttner, J. Organomet. Chem. 152, 329 (1978).
[43] A. B. Anton, N. R. Avery, B. H. Toby, and W. H. Weinberg, J. Electron. Spectrosc. 29, 181 (1983).
[44] A. B. Anton, N. R. Avery, T. E. Madey, and W. H. Weinberg, J. Chem. Phys. 85, 507 (1986).
[45] U. Schwalke, J. E. Parmeter, and W. H. Weinberg, J. Chem. Phys. 84, 4036 (1985).
[46] U. Schwalke, J. E. Parmeter, and W. H. Weinberg, Surf. Sci. 178, 625 (1986).
[47] J. E. Parmeter, U. Schwalke, and W. H. Weinberg, J. Am. Chem. Soc. 109, 1876 (1987).
[48] J. E. Parmeter, U. Schwalke, and W. H. Weinberg, J. Am. Chem. Soc. 109, 5083 (1987).
[49] G. E. Thomas and W. H. Weinberg, Rev. Sci. Instrum. 50, 497 (1979).
[50] The recombinative desorption of nitrogen adatoms from Ru(001) occurs near 800–850 K (Ref. 21).
[51] The recombinative desorption of hydrogen adatoms from Ru(001) occurs below 450 K; H. Shimizu, K. Christmann, and G. Ertl, J. Catal. 61, 412 (1980).
[52] The desorption of molecularly chemisorbed CO from Ru(001) occurs below 500 K. (a) T. E. Madey and D. Menzel, J. Appl. Phys. Suppl. 2, Part 2, 229 (1974); (b) H. Pfnür, P. Feulner, H. A. Engelhardt, and D. Menzel, Chem. Phys. Lett. 59, 481 (1978); (c) H. Pfnür, P. Feulner, and D. Menzel, J. Chem. Phys. 79, 4613 (1983).

89

[53]H. Ibach and D. L. Mills, *Electron Energy Loss Spectroscopy and Surface Vibrations* (Academic, New York, 1982), p. 348.

[54]While it is unclear exactly what this impurity might be, this loss feature is quite clear in off-specular spectra, consistent with its assignment as a $v(CH)$ mode. It seems too low in frequency to be due to a $v(NH)$ mode.

[55]For a discussion of dipole and impact scattering, see Ref. 53, Chaps. 1 and 3.

[56]The estimate of 80% of monolayer saturation is arrived at from both the thermal desorption spectra of Ref. 21, and by noting in Fig. 5 that the minimum $\delta_s(NH_3)$ frequency for monolayer ammonia on Ru(001) is approximately 1070 cm^{-1}, and assuming the frequency decrease to be linear up to saturation.

[57]P. A. Thiel, F. M. Hoffmann, and W. H. Weinberg, J. Chem. Phys. **75**, 5556 (1981).

[58]O. S. Binbrek and A. Anderson, Chem. Phys. Lett. **15**, 421 (1972), and references therein.

[59]For example, consider the $\delta_s(NH_3)$ frequencies (in cm^{-1}) of the following series of $M(NH_3)_6^{2+}$ compounds: Mn, 1146; Fe, 1156; Co, 1163; Ni, 1176; Zn, 1145. On the other hand, there is a large frequency difference between $Co(NH_3)_6^{2+}$ (1163) and $Co(NH_3)_6^{3+}$ (1329).

[60]This distance appears to be typical of metal–nitrogen bond distances in organometallic compounds of ammonia. See, for example, Ref. 38.

[61]K. Hermann, P. S. Bagus, and C. W. Bauschlicher, Phys. Rev. B **31**, 6371 (1985).

[62]C. W. Bauschlicher, J. Chem. Phys. **83**, 2619 (1985).

[63]These statements are based on a thorough search of the *Dictionary of Organometallic Compounds* (Chapman and Hall, London, 1984). While data for ammonia are not very extensive, the data for PR$_3$ ligands are, and they indicate that only on-top sites are occupied.

[64]K. Nakamoto, *Infrared and Raman Spectra of Inorganic and Coordination Compounds*, 3rd ed. (Wiley, New York, 1978), pp. 197–202.